Novel Physics in Superconductor-Ferromagnet Hybrid Structures

Marchiori Pereira, Estefani

Award date:
2019

Awarding institution:
University of Bath

Novel Physics in Superconductor-Ferromagnet Hybrid Structures

submitted by

Estefani Marchiori Pereira

for the degree of Doctor of Philosophy

of the

University of Bath

Department of Physics

June 2019

To my father

"Door meten tot weten"

"Through measurement to knowledge"

H. Kamerlingh Onnes

Abstract

The interaction between superconductivity and non-collinear ferromagnetism has been investigated in hybrid structures. The nature of the interaction between the two can convert spin-singlet Cooper pairs from a conventional superconductor into spin-triplet pairs within the ferromagnet. These can survive over longer distances in the ferromagnetic material, which is a clear signature of a novel electronic state. This thesis primarily describes efforts to realise and study these fascinating long-range spin-triplet correlations in superconductor-ferromagnet hybrid structures composed of conventional superconducting Niobium (Nb) and ferromagnetic Permalloy (Py). A disk geometry has been used to promote a magnetisation vortex in the ferromagnet, whose naturally non-collinear magnetisation makes it ideal for spin-triplet pair generation. Firstly, two distinct superconductor-ferromagnet hybrid arrays have been fabricated in which the subsystems are either electronically or magnetically coupled, and the superconducting vortex behaviour investigated by scanning Hall probe microscopy. Distinct vortex nucleation patterns occur in different hybrid arrays and unconventional vortex behaviour near the Py disks has been observed, manifested as an apparent intervortex attraction. These interesting findings motivated the fabrication of planar superconductor-ferromagnet Josephson junctions with a disk-like geometry, which exhibited anomalous electrical magnetotransport phenomena, indicating the possible role of spin-triplet supercurrents. Secondly, a commercial second generation high-temperature superconducting (2G-HTS) tape has been investigated by scanning Hall probe microscopy in order to obtain a deeper understanding of the vortex pinning energy landscape, which is critical to underpin future developments. The magnetic flux front propagation in the tape has been mapped, showing very distinct behaviours at different temperatures. Our results have been compared to a classical critical state model, and find that this only describes the observed vortex behaviour well at temperatures closer to T_c. In addition, fishtail-like magnetisation peaks have been observed that have been linked to a 'vortex matching' effect for pinning sites near the edge of the tape.

Acknowledgements

Firstly, I would like to express my complete gratitude to Prof. Simon J. Bending, my supervisor, for his constant support, expert guidance and enlightening discussions throughout the course of this project. His enthusiasm at every new experiment has taught me how to stay motivated in the face of challenges.

I thank as well Dr. Gavin Burnell and his research group in Leeds for their great assistance with the thin film sputter deposition for sample fabrication, which was invaluable.

Also, I would like to thank two inspiring researchers, Dr. Peter J. Curran, who taught me so much about the scanning Hall probe microscope, and Dr. Sara Dale for her timely guidance in all aspects of the experimental work.

I'm extremely grateful for all the technical assistance and advices provided by: Dr. Stephen Wedge and Dr. Sivapathasundaram Sivaraya in the nanofabrication facility; Paul Reddish in the mechanical workshop; Wendy Lambson in the chemistry lab; and Martin Fullick in the electronics workshop. Their patience and guidance were crucial to the progress of my research.

I would like to thank the former and current members of the Nanoscience group: Dr. Hasti Shajari, Dr. Murali Hari, David Collomb, Liam Farrar, Will Campbell and Dr. Penglei Li. They all have been essential in each stage of my experimental activities. Also, I would like to extend my thanks to all the great friends I have made during my time in Bath, for they have helped me to see different aspects of life.

Lastly, yet most importantly, I would like to thank my mother Gilnéia and my sister Camila for their continuous encouragement and unconditional love, and my fiancé Flaviano for his support and patience that were essential throughout this journey. My father did not live to see me completing this project, but I carry with me his interest for science, which I'm everyday thankful for.

Contents

Chapter 1

Overview

1.1 Motivation

Intensive research has been conducted on the search for exotic states-of-matter for the development of innovative memory and logic devices. Fascinating physics has emerged when very different materials such as superconductors (S) and ferromagnets (F) are artificially brought together [1]. Superconductivity and ferromagnetism are considered to be mutually exclusive states-of-matter, since the parallel electron spin alignment in ferromagnets is not compatible with the opposite spin pairing of Cooper pairs in conventional superconductors. At the superconductor-ferromagnet interface, a proximity effect takes place, where the superconducting order parameter exhibits rapidly damped oscillations within the adjacent ferromagnet, decaying fast over just a few nanometers inside strong ferromagnets.

In the recent years, a long range proximity effect has been reported in superconductor -ferromagnet hybrid devices [2–4], where supercurrents can survive for much longer distances within the ferromagnet. These long-range supercurrents are believed to be signatures of a novel same-spin superconducting state. This is theoretically predicted to arise due to scattering of conventional singlet Cooper pairs by non-collinear magnetic moments at the S-F interface [5], resulting in a mixing of spin singlet and spin triplet Cooper pairs. The existence of these spin triplet correlations is a direct consequence of the broken time-reversal symmetry. These spin-polarised supercurrents have allowed two fields that once were considered incompatible such as superconductivity and spintronics to be combined and are considered the building blocks for the emerging field called superconducting

spintronics [6, 7].

Modern lithographic and deposition techniques have enabled impressive hybrid device engineering. However, the microscopic physical properties of the underlying superconductor-ferromagnet interface in these devices lacks a complete understanding. Here, we have proposed an experiment where the superconducting and ferromagnetic systems, which are either magnetically or electronically coupled, are investigated by scanning Hall probe microscopy. The search for unconventional superconducting vortex behaviour leads to important insights into the underlying superconducting order parameter as reflected in the pinning energy landscape. Based on this first experiment, superconductor-ferromagnet Josephson junctions with a distinct design have been proposed and their electrical magnetotransport properties investigated in the search for anomalous transport indicating the presence of these fascinating long-range spin-polarised supercurrents.

Independently, attention has been paid to second generation coated conductors. Since the discovery of the first high-temperature superconductors (LaBaCuO [8], YBaCuO [9]), they have been subject of extensive research due to their strong potential for technological applications. Coated conductors are also known as second generation high-temperature superconductors (2G-HTS) [10] which resulted from concentrated research efforts to make them commercially applicable. A major challenge for their full implementation is the rapid suppression of the superconducting critical current density in moderate magnetic fields, caused by superconducting vortex motion. Scientists and engineers have strived to understand, improve and optimise the pinning mechanisms to control and prevent the vortex motion. Scanning Hall probe microscopy is a powerful technique which can provide a deeper understanding of the pinning energy landscape and superconducting vortices in these tapes to aid in the development and optimisation of their vortex pinning landscapes.

The primary objective of this Thesis is to investigate proximity effects in superconductor-ferromagnet hybrids containing noncollinear magnetisation, which can potentially generate fascinating long-range spin-triplet supercurrents. Two main characterisation techniques have been used: scanning Hall probe microscopy (SHPM) to directly visualise the vortex behaviour with high spatial resolution and sensitivity, and electrical magnetotransport measurements to identify and

characterise anomalous transport phenomena.

The secondary objective aims to achieve an understanding of the pinning energy landscape and the superconducting vortex behaviour in a high-temperature superconducting thin film made of YBaCuO, present in a second-generation high-temperature superconducting (2G-HTS) tape. This has been achieved by mapping the magnetic flux front penetration using scanning Hall probe microscopy (SHPM).

1.2 Thesis Structure

This thesis describes the experimental research into superconductivity and magnetism conducted at the University of Bath under the supervision of Professor Simon J. Bending. The thesis is structured as follows: Chapter 2 introduces the basic theoretical framework by briefly introducing the main phenomena and theories of superconductivity and key concepts in the physics of vortex matter. It also provides the relevant background material to set the experimental results in Chapters 4 and 5 in suitable context, though does not represent a comprehensive review of the topics. Chapter 3 describes the working principles of the experimental techniques and sample fabrication methods used to realise the systems investigated. Chapter 4 contains the experimental results and analysis of superconducting vortex imaging by scanning Hall probe microscopy of superconductor-ferromagnet hybrid structures. It aims to achieve an understanding of the pinning potential landscape due to the proximity effects between the superconducting and ferromagnetic sub-systems. Chapter 5 describes the experimental results of electrical magnetotransport measurements of superconductor-ferromagnet Josephson junctions in the search for the signatures of spin-polarised supercurrents. Chapter 6 is a somewhat independent section where the structure of 2G-HTS tapes and their development challenges are introduced. This is followed by a description of the experimental methods used for magnetic flux front imaging by scanning Hall probe microscopy as well as the experimental results and analysis in the light of a comparison with a classical critical state model. Chapter 7 closes the thesis and presents a summary of the final conclusions of the experiments as well as future prospects for extending the research work. Lastly, a list of the published works and the cited bibliography can be found.

Chapter 2

Background Theory

The theories related to the topics discussed in this thesis are introduced, explained and discussed in this chapter. This includes the London, Ginzburg-Landau and BCS theories of superconductivity which are briefly introduced in chronological order, including an understanding of the energies involved in small ferromagnetic structures and at the end the effects observed in superconductor-ferromagnet hybrid structures is discussed.

2.1 Superconductivity

Zero resistivity and perfect diamagnetism are hallmarks of superconductivity. H. Kamerlingh Onnes was the first to liquefy Helium, reaching the lowest temperature available at that time. In 1911, Onnes used such cooling capabilities to measure the resistivity of pure Mercury, observing for the first time a superconducting transition to a zero resistivity state [11]. W. Meissner and R. Ochsenfeld discovered in 1933 [12], when measuring the magnetic field distribution in tin and lead samples, that when the material is cooled down below the superconducting critical temperature the magnetic field is expelled from its interior. Hence they exhibit a perfect diamagnetic state that is destroyed only when the external magnetic field exceeds a critical value. This phenomenon is called the Meissner effect. Such exquisite properties required a new theory as the electromagnetic laws were not able to fully explain it. In the following the main theories of superconductivity that describes its phenomenological and microscopic aspects are briefly introduced.

2.1.1 London Theory

The London brothers proposed the first significant phenomenological theory of superconductivity [13] where the two main electrodynamic properties are described, the perfect conductivity and perfect diamagnetism. They were motivated by the two-fluid model and considered a superconductor where a fraction of the conduction electrons becomes superconducting and move without dissipation. The first London equation describes the perfect conductivity,

$$\frac{d}{dt}\mathbf{j_s} = \frac{n_s e^2}{m_e}\mathbf{E}, \tag{2.1}$$

where j_s is the superconducting current density inside the superconductor, n_s is the number density of superconducting electrons, m_e and e the mass and charge of the superconducting electrons and $\mathbf{E}$ the electric field. This equation shows that a steady current can be sustained in the superconducting material without an electric field presence. This is very different from a normal conductor, where a constant electric field is required to sustain the current against the material's resistance.

The second London equation describes the perfect diamagnetism, *i.e.* the Meissner-Ochsenfeld effect,

$$\mathbf{B} = -\frac{m_e}{n_s e^2}\nabla \times \mathbf{j_s}, \tag{2.2}$$

where swirling superconducting currents generate a magnetic field ($\mathbf{B}$) opposing an applied magnetic field; such currents are called superconducting screening currents. When combined with the Maxwell equation in the form $\nabla \times \mathbf{B} = \mu_0 \mathbf{j_s}$, this leads to

$$\nabla^2 \mathbf{B} = \frac{1}{\lambda^2}\mathbf{B}, \tag{2.3}$$

with

$$\lambda = \sqrt{\frac{m_e}{\mu_0 n_s e^2}}. \tag{2.4}$$

This implies that the magnetic field is screened from the interior of a superconductor over a characteristic penetration depth of λ. In a uniform magnetic field (B_0) parallel to a superconductor surface, the one-dimensional form of equa-

tion 2.3 has the solution,

$$B(x) = B_0 e^{-\frac{x}{\lambda}}, \tag{2.5}$$

where the magnetic field exponentially decreases at the superconductor surface, as shown in Figure 2-1. The London equations do not explain the occurrence of superconductivity, but they introduce restrictions on the standard electromagnetic equations in order to agree with the behaviour observed experimentally. The derivation of the equations can be found in several textbooks [14–16].

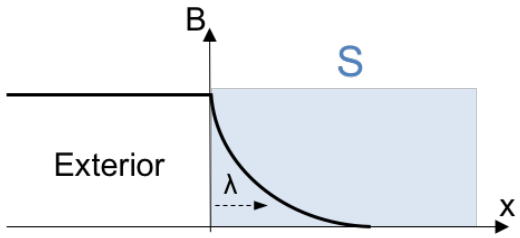

Figure 2-1: *Magnetic field near a superconductor surface. The screened magnetic field decays exponentially over a length given by the London penetration depth* λ.

2.1.2 Ginzburg-Landau Theory

Based on the previously established theory of second-order phase transitions by Landau, the theory of superconductivity proposed by Ginzburg and Landau in 1950 [17] describes the superconducting state and the normal metallic state as separate thermodynamic phases of matter. Second-order phase transitions involve some discontinuous change in symmetry of the system at the transition. In Landau's theory such transitions are characterised by an order parameter which is nonzero in the ordered state (low symmetry) below a critical temperature, T_c, and zero in the disordered state (high symmetry) above T_c.

Ginzburg and Landau postulated the existence of a complex spatially varying order parameter to characterise the superconducting state, $\psi(\mathbf{r}) = |\psi(\mathbf{r})| e^{i\theta(\mathbf{r})}$. The order parameter can be physically interpreted as a wave function for the centre of mass motion of BCS Cooper pairs of electrons, and the modulus, $|\psi(\mathbf{r})|^2 = n_s/2$, as the density of Cooper pairs in the ground state. In the general

case of an inhomogeneous superconductor in a uniform external magnetic field near T_c, where $\psi(\mathbf{r})$ is small, the superconducting state total free energy, F_s, is expressed as

$$F_s(T) = F_n(T) + \int \left(a(T)\,|\psi|^2 + \frac{b}{2}\,|\psi|^4 + \frac{1}{4m_e}\,|(-i\hbar\nabla - 2e\mathbf{A})\,\psi|^2 \right) d^3r + \int \frac{\mathbf{B}^2}{2\mu_0} d^3r, \tag{2.6}$$

where F_n is the normal state free energy, $a(T)$ and b are the characteristic Ginzburg-Landau phenomenological parameters of the material, $\mathbf{A}(\mathbf{r})$ is the magnetic vector potential and $\mathbf{B}(\mathbf{r})$ the magnetic induction at each point in the superconductor. The integration is carried out over the entire volume of the superconductor. The first two terms in the first integral are an expansion in terms of $|\psi|^2$ that describes a homogenous condensate. The third term in the same integral represents a gradient term, analogous to the kinetic energy term into the Schrödinger's equation, which represents the kinetic energy of the superconducting electrons in the presence of a vector potential. The last integral corresponds to the magnetic field energy.

In the simple case of a homogeneous superconductor with no external fields applied, the free energy density can be expressed by only the first two terms of the expansion,

$$f_s - f_n = a(T)|\psi|^2 + \frac{b}{2}|\psi|^4, \tag{2.7}$$

where $f_s(T)$ and $f_n(T)$ are the superconducting state and normal state free energy densities, $a(T)$ is a smooth function of temperature and b is positive and assumed temperature-independent. Looking at the variation of $(f_s - f_n)$ as a function of ψ, there are two possible curves depending on the sign of $a(T)$, shown in Figure 2-2. When $a(T) > 0 (T > T_c)$ the curve has a parabolic shape with a single minimum at $\psi = 0$, and when $a(T) < 0 (T < T_c)$ the curve shows minima at $\psi = \pm\psi_0$. By minimising the free energy density (eq. 2.7) with respect to $|\psi|^2$, we find that $|\psi_0|^2 = -a(T)/b$ and the free energy density difference can be written as

$$f_s - f_n = -\frac{a(T)^2}{2b} = -\mu_0 \frac{H_c^2}{2} \tag{2.8}$$

corresponding to the condensation energy of the superconductor and defining H_c,

the thermodynamic critical field.

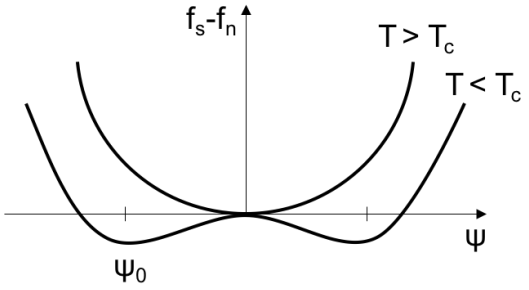

Figure 2-2: *Free energy difference between the superconducting and the normal state as a function of the order parameter. When above T_c the free energy has a single minimum at $\psi = 0$ and when below T_c the free energy has minima at $\pm\psi_0$. Adapted from Reference [15].*

The celebrated Ginzburg-Landau differential equations describe the macroscopic behaviour of superconductors when fields, currents, or gradients are imposed. By minimising the total free energy (eq. 2.6) with respect to the order parameter, $\psi(\mathbf{r})$, and the magnetic vector potential $\mathbf{A}$, we can find the two coupled Ginzburg-Landau equations,

$$(a(T) + b|\psi|^2)\psi + \frac{1}{4m_e}\left(-i\hbar\nabla - 2e\mathbf{A}\right)^2\psi = 0, \tag{2.9}$$

and

$$\mathbf{j_s} = -\frac{2e\hbar i}{4m_e}(\psi^*\nabla\psi - \psi\nabla\psi^*) - \frac{(2e)^2}{2m_e}|\psi|^2\mathbf{A}. \tag{2.10}$$

The first Ginzburg-Landau equation has the form of a Schrödinger equation for particles of mass $2m_e$, charge $2e$, wavefunction $\psi(\mathbf{r})$, and energy $-a$, apart from the nonlinear second term inside the first bracket. Similarly, the second Ginzburg-Landau equation has the same form as the usual quantum mechanical current expression for the same particles.

To understand the physical nature of the first Ginzburg-Landau equation, a simplified case must be considered in which no fields are present ($\mathbf{A} = 0$) and the order parameter $\psi(\mathbf{r})$ is real. For one-dimension the first Ginzburg-Landau

equation reduces to

$$a(T)\psi(x) + b\psi^3(x) - \frac{\hbar^2}{4m_e}\frac{d^2\psi(x)}{dx^2} = 0. \tag{2.11}$$

With the appropriate boundary condition, the solution is given by

$$\psi(x) = \psi_0 \tanh\left(\frac{x}{\sqrt{2}\xi(T)}\right), \tag{2.12}$$

with

$$\xi(T) = \sqrt{\frac{\hbar^2}{4m_e a(T)}}. \tag{2.13}$$

This characterises the spatial variation of ψ within the superconductor by a characteristic length scale $\xi(T)$, known as the Ginzburg-Landau coherence length. Depicted in Figure 2-3, $\xi(T)$ is a measure of the order parameter recovery distance from the superconductor surface.

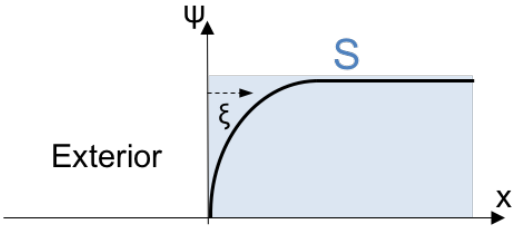

Figure 2-3: *The order parameter of a superconductor near the sample surface. The order parameter is reduced over a characteristic length given by the coherence length, ξ.*

Likewise, we can comprehend the second Ginzburg-Landau equation by considering the phase of the order parameter, $\psi(\mathbf{r}) \rightarrow |\psi(\mathbf{r})|e^{i\theta(\mathbf{r})}$, allowing it to be written as,

$$\mathbf{j_s} = \frac{2e\hbar}{2m_e}|\psi|^2\nabla\theta - \frac{(2e)^2}{2m_e}|\psi|^2\mathbf{A}. \tag{2.14}$$

In the ground state when the phase, θ, is constant the supercurrent can be rewritten as,

$$\mathbf{j_s} = -\frac{(2e)^2}{2m_e}|\psi|^2\mathbf{A}, \tag{2.15}$$

and applying the curl to both sides we obtain

$$\nabla \times \mathbf{j_s} = -\frac{(2e)^2}{2m_e}|\psi|^2\mathbf{B}, \tag{2.16}$$

which is the same as the London equation (eq. 2.2). This leads to a definition of the penetration depth, λ, as

$$\lambda(T) = \sqrt{\frac{m_e}{\mu_0 2|\psi|^2 e^2}}. \tag{2.17}$$

This explains the Meissner-Ochsenfeld effect and shows that when there is no spatial variation in the density of Cooper pairs, $|\psi|^2 = n_s/2$, the Ginzburg-Landau theory reduces to the London equation.

Boundary conditions must be used to ensure appropriate functional behaviour at the superconductor interface; a generalised boundary condition derived by De Gennes [18] from the microscopic theory is given by

$$\mathbf{n} \cdot (-i\hbar\nabla + 2e\mathbf{A})\psi = \frac{i\hbar}{b}\psi, \tag{2.18}$$

where $\mathbf{n}$ is the unit vector normal to the surface of the superconductor and b is a real constant. If $\mathbf{A} \cdot \mathbf{n} = 0$, the boundary condition is characterised by an extrapolation length b from the superconductor surface to a point inside the adjacent material at which $\psi = 0$. The value of b depends on the nature of the material at the superconductor interface, where for insulators, $b \to \infty$, for magnetic materials, $b \to 0$ and for normal metals, $b > 0$, in the intermediate range. This is a very simplified picture of the phenomenon called the proximity effect whereby superconductivity is induced into the material at the superconductor interface, as discussed in detail on section 2.3 of this chapter. For a didactic derivation of the Ginzburg-Landau theory the textbooks [15, 19] are recommended.

2.1.3 Type I and Type II Superconductors

A superconductor can be described by at least three characteristic parameters, the penetration depth $\lambda(T)$, the coherence length $\xi(T)$, and the carrier mean free path l. The last parameter indicates if the superconductor is in the clean limit $l > \xi$, or in the dirty limit $l < \xi$. The first two parameters describe the

spatial variation of an applied magnetic field and the superconducting order parameter at the superconductor surface, respectively. The superconductor surface energy per unit area is defined by $\gamma \approx (\xi - \lambda)\,(\mu_0 H_c^2/2)$. On the basis of this, Ginzburg-Landau defined a temperature-independent dimensionless parameter $\kappa = \lambda(T)/\xi(T)$, which divides superconductors into two groups:

- Type I superconductors, for $\kappa < 1/\sqrt{2}$ where $\xi > \lambda$, have a positive surface energy making it energetically unfavourable to create interfaces between the normal and superconducting state. When in a small external magnetic field H, the B field remains zero inside the superconductor, *i.e.* in the Meissner state, until suddenly superconductivity is destroyed at a critical field H_c, as shown in Figure 2-4(a).

- Type II superconductors, for $\kappa > 1/\sqrt{2}$ where $\xi < \lambda$, have a negative surface energy which favours the creation of normal-superconducting state interfaces to minimise the total energy. At external fields below a lower critical field H_{c1}, the superconductor is in the Meissner state. Once the field exceeds H_{c1}, magnetic flux starts to penetrate the superconductor up to an upper critical field H_{c2}, where superconductivity is completely destroyed, as shown in Figure 2-4(b).

The magnetic critical fields vary as a function of temperature, and close to the critical temperature T_c they all approach zero. Figure 2-4(c) and (d) show typical H-T phase diagrams for type I and type II superconductors, respectively.

2.1.4 Vortex Matter

The normal-superconducting interface in the bulk of a superconductor was analysed by Fritz London for a multiply connected superconductor in the presence of a magnetic field. He considered the situation of a hole (or normal region) passing through the superconductor, illustrated in Figure 2-5, and associated fluxoid, Φ'. By integrating the second London equation (eq. 2.2) in the form,

$$0 = \mu_0 \lambda^2 \nabla \times \mathbf{j_s} + \mathbf{B}, \tag{2.19}$$

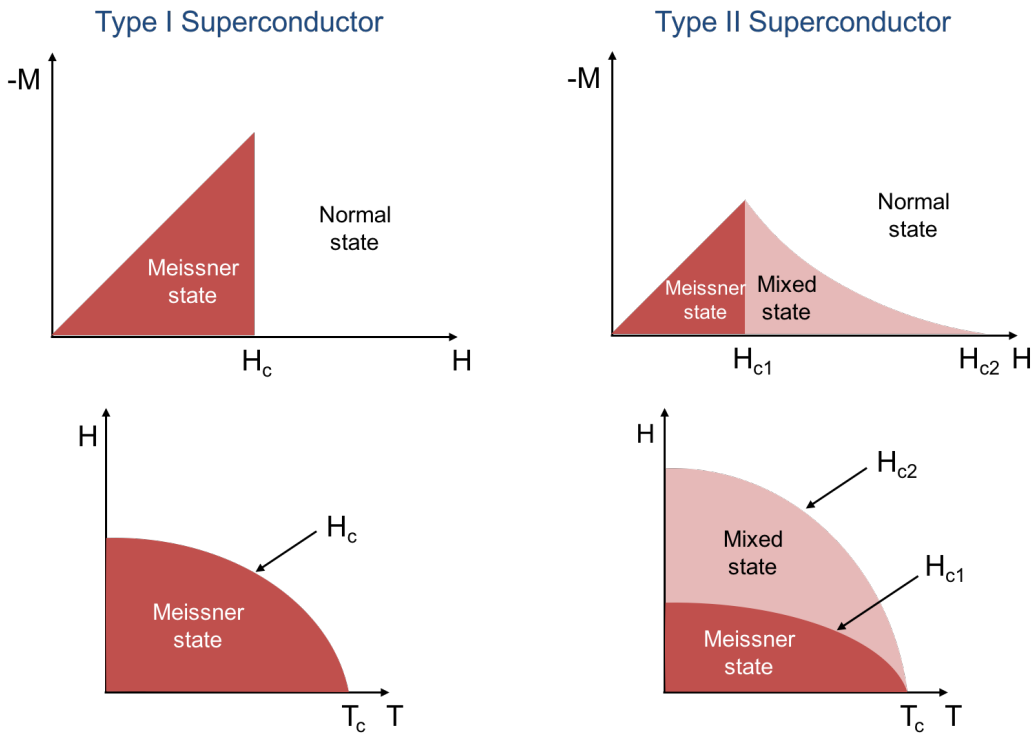

Figure 2-4: *Magnetic response for (a) type I and (b) type II superconductor when an external magnetic field is applied. Typical H-T phase diagram for (c) type I and (d) type II superconductors.*

over the surface S bounded by the path C enclosing the normal region, we find

$$\Phi^{'} = \int \mu_0 \lambda^2 \nabla \times \mathbf{j_s} \cdot d\mathbf{S} + \int \mathbf{B} \cdot d\mathbf{S}. \tag{2.20}$$

The second term is the total flux Φ passing through the normal hole and can be expressed in terms of the vector potential $\mathbf{A}$. Using the Stokes' theorem that relates the curl and the line integral of a function $\mathbf{X}$

$$\int_S \nabla \times \mathbf{X} \cdot d\mathbf{S} = \oint_C \mathbf{X} \cdot d\mathbf{s}, \tag{2.21}$$

where $d\mathbf{s}$ is an infinitesimal line of the path C enclosing the normal region, the fluxoid $\Phi^{'}$ can then be expressed as

$$\Phi^{'} = \oint \mu_0 \lambda^2 \mathbf{j_s} \cdot d\mathbf{s} + \oint \mathbf{A} \cdot d\mathbf{s} = \frac{1}{2e} \oint (2m_e \nu_\mathbf{s} + 2e\mathbf{A}) \cdot d\mathbf{s} \tag{2.22}$$

This expression relates the fluxoid $\Phi^{'}$ to the canonical momentum distribution $\mathbf{p}(\mathbf{r}) = 2m_e\nu_\mathbf{s}(\mathbf{r}) + 2e\mathbf{A}(\mathbf{r})$, where the first term represents the Cooper pairs kinetic momentum and the second term is the momentum associated with the magnetic field. From eq. 2.20, we can see that the fluxoid $\Phi^{'} = 0$ for any path around only superconducting material (no normal region) and also that the fluxoid $\Phi^{'}$ has the same value for any path around a given normal region. Similarly, in a time-varying applied field the supercurrent density $\mathbf{j_s}$ changes in order to hold $\Phi^{'}$ constant. The time variation of the fluxoid can be written as

$$\frac{d\Phi^{'}}{dt} = \int \mu_0 \lambda^2 \nabla \times \frac{d\mathbf{j_s}}{dt} \cdot d\mathbf{S} + \int \frac{d\mathbf{B}}{dt} \cdot d\mathbf{S}. \tag{2.23}$$

Substituting Maxwell's equation, $d\mathbf{B}/dt = -\nabla \times \mathbf{E}$, and the first London equation (eq. 2.1) in the form, $\mu_0 \lambda^2 d\mathbf{j_s}/dt = \mathbf{E}$, we find

$$\frac{d\Phi^{'}}{dt} = \int \nabla \times \mathbf{E} \cdot d\mathbf{S} - \int \nabla \times \mathbf{E} \cdot d\mathbf{S} = 0. \tag{2.24}$$

This implies that the fluxoid $\Phi^{'}$ is conserved and has a unique constant value for all paths enclosing any given hole. The fluxoid $\Phi^{'}$ value can be found by

applying the Bohr-Sommerfeld quantum condition to eq. 22,

$$\Phi^{'} = \frac{1}{2e}\oint (2m_e\nu_{\mathbf{s}} + 2e\mathbf{A}) \cdot d\mathbf{s} = \frac{1}{2e}\oint \mathbf{p} \cdot d\mathbf{s} = \frac{nh}{2e} = n\Phi_0 \tag{2.25}$$

where n is an integer. This shows the phenomenon of flux quantisation in superconductors where the fluxoid $\Phi^{'}$ is restricted to a discrete set of integral multiples of a flux quantum $\Phi_0 = \frac{h}{2e} = 2.07\,\mathrm{mT}.\mu m^2$.

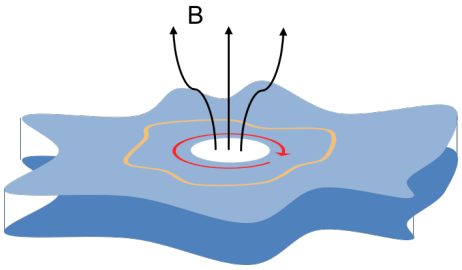

Figure 2-5: *Superconductor (blue) with a hole (normal region). The arbitrary path C (orange) encloses the normal region and a surface area S.*

A. A. Abrikosov [20] predicted the radically different behaviour of type II superconductors by solving the general Ginzburg-Landau eq. 2.6 in the regime where κ is large, i.e. $\xi > \lambda$, and near to H_{c2}. The order parameter $\psi(\mathbf{r})$ forms into a periodic lattice of vortices each carrying a quantum of flux Φ_0. This reveals how the magnetic flux penetrates superconductors in the mixed state between the lower critical field H_{c1} and the upper critical field H_{c2}.

A single vortex exhibits a core of diameter $\sim 2\xi(T)$, where the order parameter $\psi(\mathbf{r})$ is strongly suppressed and becomes zero at the centre. The whole vortex diameter is roughly $\sim 2\lambda(T)$. Vortical superconducting screening currents flowing around the core concentrate the magnetic flux towards the central normal region. The local magnetic field $\mathbf{B}(\mathbf{r})$ is maximum at the centre of the vortex and decays over the characteristic length $\lambda(T)$. A schematic diagram of two vortices and the characteristic length scales is shown in Figure 2-6.

Abrikosov's solution is exact near to H_{c2}, where the vortices are separated by distances of the order of the coherence length $\xi(T)$. The upper critical field H_{c2}, is then given by,

$$H_{c2}(T) = \frac{\Phi_0}{2\pi\mu_0\xi(T)^2}. \tag{2.26}$$

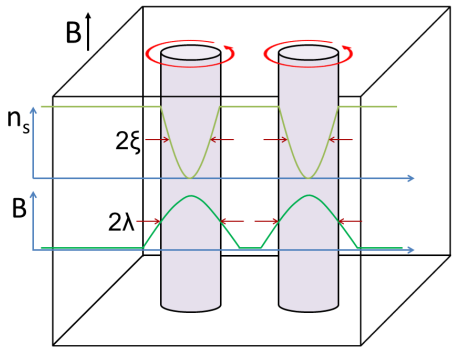

Figure 2-6: *Illustration of two vortices structure with the characteristic parameters indicated.*

Notice that at H_{c2} there is one quantum flux in each unit area $2\pi\xi(T)^2$. In contrast, at H_{c1} there are very few well separated vortices in the superconductor. A single vortex has the approximate free energy per unit length of

$$E_v = \frac{\Phi_0^2}{4\pi\mu_0\lambda(T)^2} ln\left(\frac{\lambda}{\xi}\right). \tag{2.27}$$

The energy balance between the total energy cost E due to the formation of the vortices and the magnetic work gained $\mu_0 HdM = HdB$ by their presence in the superconductor, favours the presence of the vortices when $E < H\Phi_0$. Therefore, it becomes energetically favourable to allow vortices to enter the superconductor when $H > H_{c1}$, where

$$H_{c1}(T) = \frac{\Phi_0}{4\pi\mu_0\lambda(T)^2} ln\left(\frac{\lambda}{\xi}\right). \tag{2.28}$$

Notice that the single vortex energy, eq. 2.27, has a quadratic dependence on Φ_0, thus a lattice of multi-quanta vortices has much higher energy than a lattice of single-quantum vortices $E_v(n\Phi_0) > nE_v(\Phi_0)$. However, the vortical supercurrents surrounding adjacent vortices of same polarity flow in opposite directions which results in a repulsive interaction between them. Hence, due to this energy penalty due to the interaction between adjacent vortices, under certain special conditions a superconductor can reach a lower energy configuration by creating a multi-quanta vortex lattice than a single-quantum vortex lattice.

This repulsive interaction between vortices stabilises a closed-packed equilibrium vortex structure with a triangular vortex arrangement, in which the distance between nearest neighbours is maximised. The distance between first vortices in a triangular vortex lattice satisfy $a_{\triangle}^2 = \sqrt{\frac{4}{3}}\frac{\Phi_0}{B}$ and this has a slightly lower energy than the square vortex lattice when $a_{\square}^2 = \frac{\Phi_0}{B}$.

Vortices are not completely free as the underlying superconductor crystal structure perturbs the ordered triangular lattice, sometimes creating square or even rectangular vortex arrays. Also, defects in the material, of either intrinsic or extrinsic origin, introduce disorder into the vortex lattice, creating a glassy vortex arrangement. The vortices minimise the free energy of the system by locating where these local variations suppress the order parameter, *i.e.* the vortices are pinned at these so called pinning centres.

Type II superconductors are of high technological interest as they can carry high current densities without energy loss. However, in the presence of an applied current the vortices experience a Lorentz force $\mathbf{F_L} = \mathbf{j} \times \mathbf{B}$ which makes them move perpendicular to the direction of current flow. Vortex motion induces a finite longitudinal electric field, $\mathbf{E} = \mathbf{B} \times \mathbf{v}$, where v is the vortex velocity. Consequently, this creates a finite resistance and power is dissipated. In order to keep the superconductor in its dissipation-free state the Lorentz force $\mathbf{F_L}$ must not exceed the pinning force $\mathbf{F_p}$ acting on a vortex. Hence, pinning is deliberately made strong, by the inclusion of nanoparticles, corrugations, vacancies, nanostructures, irradiation-induced defects and many others, in order to reach higher critical currents. The pinning force $\mathbf{F_p}$ acts primarily on the vortex core, and the most effective pinning centres have a diameter comparable to that of the vortex core $\sim 2\xi$.

Artificial periodic pinning structures can enhance the critical current at well-defined matching fields. This commensurability effect occurs when the period of the regular pinning structures, d, matches the vortex lattice spacing, a, *i.e.* when $d = na$. For a square vortex lattice, the matching fields are expected at integers or specific fractions of the matching field $B_\Phi = \frac{\Phi_0}{d^2}$ [21–23].

2.1.5 BCS Theory

The microscopic theory developed by J. Bardeen, L. Cooper and J. Schrieffer [24] brilliantly describes the origin of superconductivity. It shows that an effective attractive interaction can bind pairs of electrons into bound states which gives rise to superconductivity.

An effective attraction between electrons is possible via their interaction with phonons. A phonon $\mathbf{q}$ emitted by one electron with momentum $\hbar\mathbf{k}$, which exits with momentum $\hbar\mathbf{k}^{'}$, is absorbed by another electron with momentum $\hbar\mathbf{l}$ acquiring a momentum $\hbar\mathbf{l}^{'}$. This is illustrated as a Feynman diagram in Figure 2-7. From momentum conservation, the momentum of the exchanged phonon is $\hbar\mathbf{k} - \hbar\mathbf{k}^{'} = \hbar\mathbf{q}$ and phonon energy equals $\hbar\omega_{\mathbf{q}}$. This corresponds to an effective interaction between electrons. It can be physically pictured as a free electron traveling through the lattice that attracts the positive ions, this results in a positive polarisation of the medium which in turn attracts a second free electron. The effective interaction potential $V_{\mathbf{k}\mathbf{k}'}$ is given by

$$V_{\mathbf{k}\mathbf{k}'} = \frac{e^2}{\epsilon\mathbf{q}^2} + \frac{g^2\hbar\omega_{\mathbf{D}}}{(\hbar\omega_{\mathbf{q}})^2 - (\hbar\omega_{\mathbf{D}})^2}, \tag{2.29}$$

where ϵ is the dielectric function of the medium, g is the electron-phonon coupling constant, and $\hbar\omega_{\mathbf{D}}$ is the Debye energy for phonons in the lattice. The first term corresponds to the usual repulsive Coulomb interaction between electrons, and the second term corresponds to the phonon-mediated interaction which is negative (attractive) when $|\hbar\omega_{\mathbf{q}}| < \hbar\omega_{\mathbf{D}}$. Superconductivity arises if the net balance of the two interactions is negative resulting in an attractive interaction.

The electron-lattice interaction was first suggested by Fröhlich [25] and experimentally confirmed by the isotope effect [26], $T_c \propto M^{-1/2}$, where the superconducting critical temperature T_c was approximately proportional to the inverse square root of the mass of the crystal lattice ion M for isotopes of the same element.

Cooper showed that a very weak attractive interaction between two electrons near the Fermi surface is sufficient to form a bound state which causes an instability in the Fermi sea. In the case of two electrons near the Fermi level at T = 0, the lowest energy state has zero total momentum, so that the two electrons must have equal and opposite momenta. The total wavefunction $|\Psi\rangle = |\psi_r, \psi_\sigma\rangle$

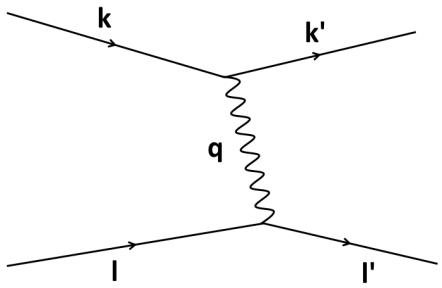

Figure 2-7: *Feynman diagram of the electron-electron interaction due to the emission and absorption of a phonon of momentum* $\mathbf{q}$.

must be asymmetric under an exchange of the two electrons. The spin wavefunction $|\psi_\sigma\rangle$ can be in the antisymmetric singlet spin state $|\uparrow\downarrow - \downarrow\uparrow\rangle$ or in one of the symmetric triplet spin states $|\uparrow\downarrow + \downarrow\uparrow\rangle$, $|\uparrow\uparrow\rangle$ and $|\downarrow\downarrow\rangle$. Therefore, for the spin-singlet state the spatial wavefunction $|\psi_r\rangle$ must be symmetric under electron interchange. Conversely, for a spin-triplet state the spatial wavefunction $|\psi_r\rangle$ would have to be an antisymmetric function. In practice the singlet coupling gives a larger probability amplitude of having the two electrons near each other.

To treat the problem for many electrons, Bardeen Cooper and Schrieffer used the variational method with the following pairing Hamiltonian:

$$\mathcal{H} = \sum_{\mathbf{k},\sigma} \epsilon_{\mathbf{k}} \mathrm{c}^{\dagger}_{\mathbf{k}\sigma} \mathrm{c}_{\mathbf{k}\sigma} + \sum_{\mathbf{k},\mathbf{k}'} \mathcal{V}_{\mathbf{k}\mathbf{k}'} \mathrm{c}^{\dagger}_{\mathbf{k}'\uparrow} \mathrm{c}^{\dagger}_{-\mathbf{k}'\downarrow} \mathrm{c}_{-\mathbf{k}\downarrow} \mathrm{c}_{\mathbf{k}\uparrow} \tag{2.30}$$

The first term corresponds to the kinetic energy, where $\epsilon_{\mathbf{k}}$ is the energy of an electron with momentum $\hbar\mathbf{k}$ and spin $\sigma = \uparrow, \downarrow$ within $\pm\hbar\omega_{\mathbf{D}}$ of the Fermi energy. The second term corresponds to the interaction of an electron pair scattered from $(-k, \downarrow)(k, \uparrow)$ to $(k', \uparrow)(-k', \downarrow)$, where $\mathrm{c}^{\dagger}$ and c are the creation and annihilation operators, respectively. Together with the Hamiltonian they used the following variational wavefunction to minimise the total energy:

$$|\Psi_{BCS}\rangle = \prod_{k} (u^{*}_{\mathbf{k}} + v_{\mathbf{k}} \mathrm{c}^{\dagger}_{\mathbf{k}\uparrow} \mathrm{c}^{\dagger}_{-\mathbf{k}\downarrow}) |0\rangle \tag{2.31}$$

where $u_{\mathbf{k}}$ and $v_{\mathbf{k}}$ are variational parameters and $|u_{\mathbf{k}}|^2 + |v_{\mathbf{k}}|^2 = 1$. This wavefunc-

tion describes a coherent state of Cooper pairs. It starts from the vacuum $|0\rangle$ and adds pairs of electrons with zero total momentum and opposite spins.

By minimising the total energy $E = \langle \Psi_{BCS} | \mathcal{H} | \Psi_{BCS} \rangle$ we can obtain the BCS excitation spectrum $\pm E_k = \pm\sqrt{(\epsilon_k - E_F)^2 + \Delta^2}$, where Δ is the BCS gap parameter. The spectrum of E_k as a function of k near k_F is shown in Figure 2-8. There are no superconducting states with energy less than $\pm\Delta$ around the Fermi energy.

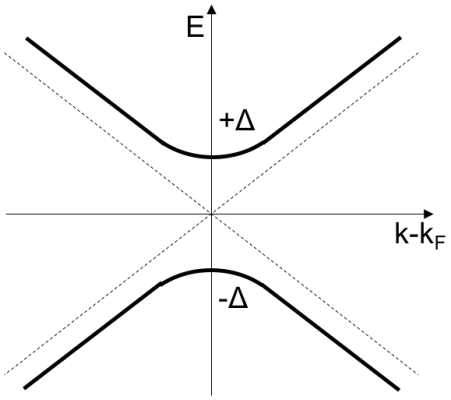

Figure 2-8: *Quasiparticle energy as a function of k near the Fermi wave vector. The electron and hole energies are illustrated by the dashed lines. There are no states available below an energy Δ in the superconducting state.*

The energy gap at zero temperature is given by,

$$\Delta = \frac{\hbar\omega_D}{\sinh\left[\frac{1}{N(0)V}\right]}, \tag{2.32}$$

where $N(0)$ is the density of states at the Fermi level. In the weak coupling limit $N(0)V \ll 1$ this equation can be approximated as

$$\Delta = 2\hbar\omega_D e^{-\frac{1}{N(0)V}}. \tag{2.33}$$

At the critical temperature T_c where $\Delta(0) \to 0$, we see that,

$$k_B T_c = 1.13\hbar\omega_D e^{-\frac{1}{N(0)V}}, \tag{2.34}$$

where at T = 0 we have $2\Delta(0) = 3.528 k_B T_c$ which is the excitation energy necessary to break a Cooper pair.

Two years after the publication of the BCS theory, Gor'kov considered the case when the superconducting gap is very small, *i.e.* near T_c. He derived the Ginzburg-Landau theory from the BCS theory finding that the spatially dependent superconducting gap $\Delta(\mathbf{r})$ is proportional to the Ginzburg-Landau order parameter $\psi(\mathbf{r})$.

2.2 Ferromagnetism in Microscopic Structures

2.2.1 Introduction to Ferromagnetism

Materials can be classified according to their magnetic susceptibility $\chi = M/H$, *i.e.* the ratio of their magnetisation with respect to an external magnetic field. The common forms of magnetism are paramagnetism $\chi > 0$, diamagnetism $\chi < 0$, and ferromagnetism $\chi \gg 0$.

Ferromagnetism is a manifestation of spontaneous alignment of the atomic magnetic moments in solids. This spontaneous magnetisation depends on temperature and becomes zero above the Curie temperature, where the material generally becomes paramagnetic.

The spontaneous alignment stems from the coupling between the magnetic moments of neighbouring atoms, which mainly arise from the spin of the electrons with an additional contribution from the orbital motion of electrons around the atom nucleus. This interaction is called exchange coupling and can be expressed by the Heisenberg spin exchange Hamiltonian,

$$\mathcal{H} = -\mathcal{J}\mathbf{S_1} \cdot \mathbf{S_2} \tag{2.35}$$

where $\mathcal{J}$ is the exchange constant, $\mathbf{S_1}$ and $\mathbf{S_2}$ are operators of electron spins on two adjacent atoms. When $\mathcal{J} < 0$ the spins tend to align antiparallel (antiferromagnetic), while for $\mathcal{J} > 0$ a parallel align of the spins is favoured (ferromagnetic).

A hysteresis loop can provide fundamental information on the material magnetic properties and a generalised loop can be seen in Figure 2-9. It shows the intrinsic saturation spontaneous magnetisation, M_s, and two extrinsic properties,

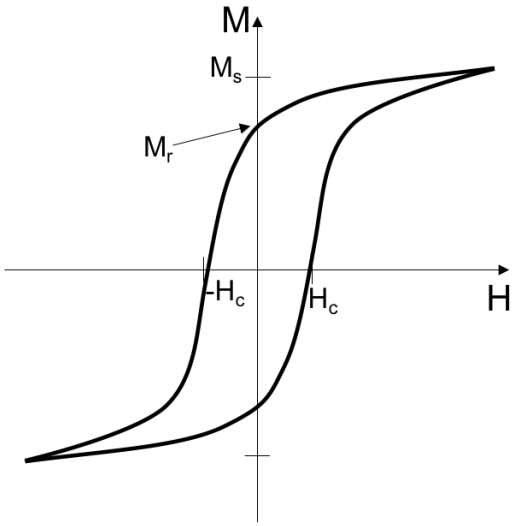

Figure 2-9: *Generalised hysteresis loop with saturation magnetisation M_s, remanence M_r and the coercivity H_c indicated. Adapted from Reference [27].*

the remanence, M_r and the coercivity, H_c, which depend on the shape, surface roughness, microscopic defects and thermal history of the material.

Ferromagnetic materials can be classified based on their coercivity as hard and soft materials. Hard magnetic materials have high coercivity and show broad square-like hysteresis loops, as observed in materials like NdFeB and SmCo magnets. In contrast, soft magnetic materials have low coercivity and show very narrow loops, as found in magnetic alloys such as Permalloy ($Ni_{80}Fe_{20}$).

These materials generally have natural directions of magnetisation due to magnetic anisotropy that lie along one or more easy axes, as illustrated in Figure 2-10. The uniaxial anisotropy energy E_a represents the energy cost to rotate the magnetisation direction away from the easy axis, which in the case of uniaxial anisotropy is given by

$$E_a = K_u \sin\theta^2, \tag{2.36}$$

where θ is the angle between the direction of magnetisation and the easy axis, and K_u is the anisotropy constant. Anisotropy limits the coercivity in hard magnets and adds to the coercivity in soft magnets. There are several sources of anisotropy in magnetic materials such as magnetocrystalline anisotropy due to spin-orbit coupling in the specific crystallographic structure of the material, shape

anisotropy from the demagnetising field that opposes the material magnetisation and depends on the sample shape, and induced anisotropy when a preferred direction of magnetisation is created by an applied stress, or by deposition or annealing an alloy in a magnetic field in order to create atomic-scale texture.

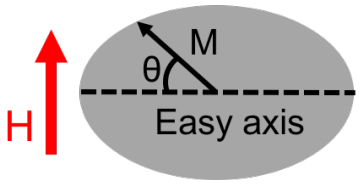

Figure 2-10: *An applied external magnetic field rotates the magnetisation away from the material easy axis.*

A magnetic moment can be viewed as a single dipole; from the Biot-Savart law the dipole magnetic field due to a magnetic moment, $\mathbf{B}$, is given by

$$\mathbf{B}(\mathbf{r}) = \frac{\mu_0}{4\pi}\left[3\frac{(\mathbf{m}\cdot\mathbf{r})\mathbf{r}}{r^5} - \frac{\mathbf{m}}{r^3}\right], \tag{2.37}$$

where $\mathbf{r}$ is the vector from the magnetic moment to a certain point in space. The dipole field decay with distance leads to a weak long range dipole-dipole interaction with a second moment at position r.

Electrostatic and magnetostatic effects are the main contributions to the energy of a ferromagnetic material. The electrostatic interactions include the exchange interaction and related effects. The magnetostatic interactions involve the self-energy of the interaction of the material with its own magnetic field, and the interaction of the material with varying external magnetic fields. The magnetostatic interactions are weaker compared to the electrostatic interactions but key to the domain formation and the magnetisation processes.

2.2.2 Ferromagnetic Disk Structure

Ferromagnetic materials generally form domain structures in order to reduce their magnetostatic energy, however in very small ferromagnetic systems the formation of domain walls is not energetically advantageous. In disk-like structures of micrometer or sub-micrometer size, a curling magnetic configuration, *i.e.* a

magnetisation vortex, is expected in place of conventional domains as shown in Figure 2-11(a). In this configuration the in-plane magnetisation direction gradually changes so as not to lose much exchange energy, but enough to cancel out the total dipole energy [28]. The angle between adjacent spins near the centre of the disk becomes increasingly large which drives the formation of a core to the vortex structure where the magnetisation turns out-of-plane and is oriented perpendicular to the plane of the disk [29].

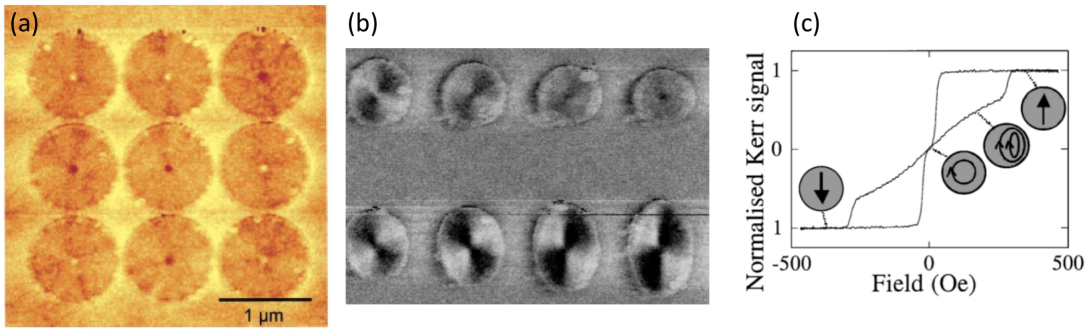

Figure 2-11: *(a) Magnetic Force Microscopy (MFM) image of ferromagnetic permalloy disks of 1 μm diameter, reproduced from Reference [28]. (b) Ferromagnetic permalloy ellipses with major axis along the vertical axis varying from 1 μm to 2 μm, adapted from Reference [29]. (c) Hysteresis loop measured by Kerr microscopy of supermalloy ($Ni_{80}Fe_{14}Mo_5$) disks of 300 nm diameter and 10 nm thickness. Reproduced from Reference [30].*

In thin films of soft ferromagnetic materials such as permalloy ($Ni_{80}Fe_{20}$) the easy axis generally has an in-plane orientation, a situation that is considered ideal for the formation of a magnetic vortex in small disk-like structures. The diameter and thickness ranges for the formation of such magnetic vortex states in permalloy have been extensively studied [28–32]. For a single magnetic vortex, the disks can range from 100 nm up to 1 μm in diameter, with thicknesses ranging from 15 nm to 50 nm. Below this range the disks exist in a dipole-like structure, while above this range the disks exhibit more than one magnetisation vortex.

Additional anisotropies in permalloy disks can destroy the in-plane curling configuration. In the case of shape anisotropy, elliptical disks show four quadrants of alternating up and down magnetisation, whereby a longer major-axis shows stronger contrast. Figure 2-11(b) shows two different pattern orientations which

correspond to two directions of circulation (clockwise or counterclockwise). When an external in-plane magnetic field is applied the magnetic moments align along the magnetic field, displacing the magnetic vortex core sideways. The magnetic vortex core is annihilated at a magnetic field, H_a, and nucleates again once the external field is reduced to a field, H_n, describing the typical hysteresis loop shown in Figure 2-11(c).

2.2.3 Object Oriented MicroMagnetic Framework (OOMMF) Simulations

The ferromagnetic disk structure has been simulated and studied using the object oriented micromagnetic framework (OOMMF) code [33]. Developed by M.J. Donahue and D.G. Porter, OOMMF uses a finite difference technique with 3D spins on a grid of rectangular elements where the magnetic moments interact according to the Landau-Lifshitz equation,

$$\frac{d\mathbf{M}}{dt} = -\gamma\left[\mathbf{M}\times\mathbf{H}_{eff}\right] - \gamma\frac{\alpha}{M_s}\mathbf{M}\times\left[\mathbf{M}\times\mathbf{H}_{eff}\right], \tag{2.38}$$

where $\mathbf{M}$ is the pointwise magnetization, $\mathbf{H}_{eff}$, is the pointwise effective field, γ is the Landau-Lifshitz gyromagnetic ratio for an atomic spin and α is the Landau damping coefficient. The first term describes the precession and the second term the damping of the magnetisation in a solid. The effective field, $\mathbf{H}_{eff}$, can be expressed as

$$\mathbf{H}_{eff} = -\frac{\delta E}{\delta M}. \tag{2.39}$$

It combines all energies including the exchange energy, the anisotropy energy, the self-magnetostatic (demagnetization) energy and the Zeeman energy. Figure 2-12 illustrates the simulation of a permalloy disk of 1 μm diameter and 50 nm thickness. The arrows represent magnetic moments, the red colour indicates upwards magnetisation, the blue colour indicates downwards magnetisation, and the absence of colour indicates in-plane magnetisation. The colour scale highlights the perpendicular magnetic configuration at the core of the disk. Figures Figure 2-12(b) and (c) show the magnetisation when an in-plane magnetic field is applied along the horizontal axis in opposite directions. Notice that the magnetic moments start to align with the applied magnetic field and the vortex core moves

sideways with respect to the applied field direction.

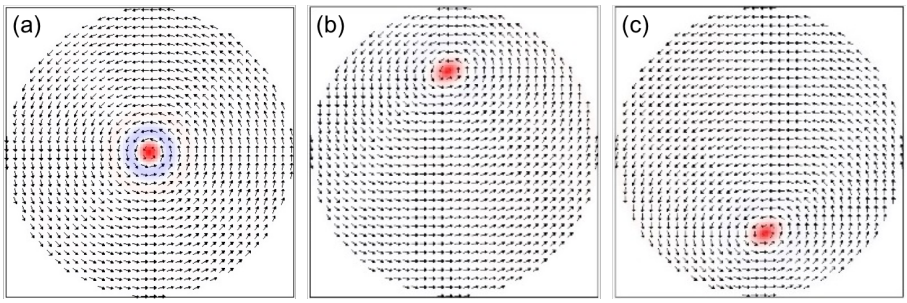

Figure 2-12: *(a) OOMMF simulation of a 1 μm diameter disk of permalloy of 50 nm thickness. An external magnetic field is applied along the horizontal axis in the (b) positive and (c) negative directions.*

2.3 Superconducting Heterostructures

2.3.1 Superconductor-Normal Metal Interface

When a superconductor and a normal metal are placed in intimate contact, the Cooper pairs near the interface can penetrate into the normal metal and induce superconductivity, such a phenomenon is called a *proximity effect*. The superconducting order parameter $\psi(x) = \psi_0 e^{-\xi_n x}$ decays exponentially inside the normal metal, as schematically represented in Figure 2-13(a). The Cooper pairs are formed by two electrons in a spin-singlet state with equal and opposite momenta and spins which results in a zero total momentum for the pair, this is shown in Figure 2-13(b). They penetrate over a characteristic length of $\xi_n \sim \sqrt{\frac{\hbar D_n}{2\pi k_B T_c}}$ into the normal metal in the diffusive regime, where D_n is the diffusion constant, and over a characteristic length of $\xi_n \sim \frac{\hbar v_F}{2\pi k_B T_c}$ in the clean limit, where v_F is the Fermi velocity. This characteristic length is typically of the order of a few microns. At the same time there is a weakening of the superconductivity near the interface with the normal metal. The Cooper pairs leak into the normal metal which decreases the superconducting transition temperature of the adjacent superconductor; this phenomenon is called the *inverse proximity effect* [1].

A characteristic of the proximity effect is Andreev reflection [34], in which an electron (hole) in the normal metal, with momentum k and kinetic energy less

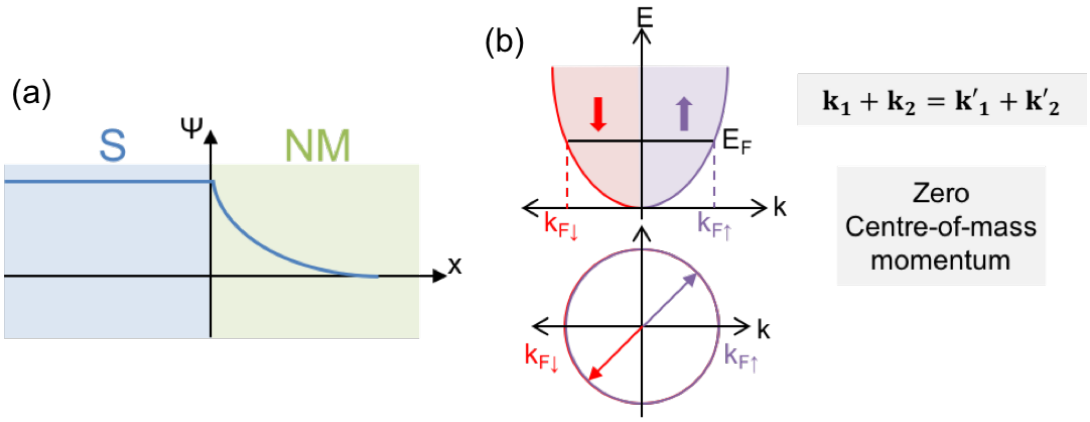

Figure 2-13: *(a) The proximity effect between a superconductor and a normal metal. The blue line illustrates the exponential decay of the superconducting order parameter within the normal metal. (b) The energy as a function of momentum k for electrons in a conventional superconductor. Adapted from Reference [4].*

than the superconducting energy gap, Δ, reflects as a hole (electron) of equal momentum at the interface with a superconductor. Hence, a net charge of $\pm 2e$ is transferred to the superconducting side of the interface as a Cooper pair, which corresponds to an increase of the electrical conductance by a factor of 2 with respect to the normal-state conductance [35].

2.3.2 Josephson Effect in Superconductor-Superconductor Junctions

First predicted by a doctoral student at the University of Cambridge called Brian Josephson, the Josephson effect describes the phenomenon of the supercurrent tunnelling through a barrier when the order parameters on either side of a junction overlap [36]. Two well-separated superconductors present distinct order parameter phases, however once in close proximity, typically $< 2\,\text{nm}$, Cooper pairs can tunnel from one superconductor to another and the phases become correlated. Two weakly coupled superconductors can be realised in different Josephson junction structures such as a Dayem bridge (constriction), a point contact, a proximity effect bridge and crossed wires, as illustrated in Figure 2-14.

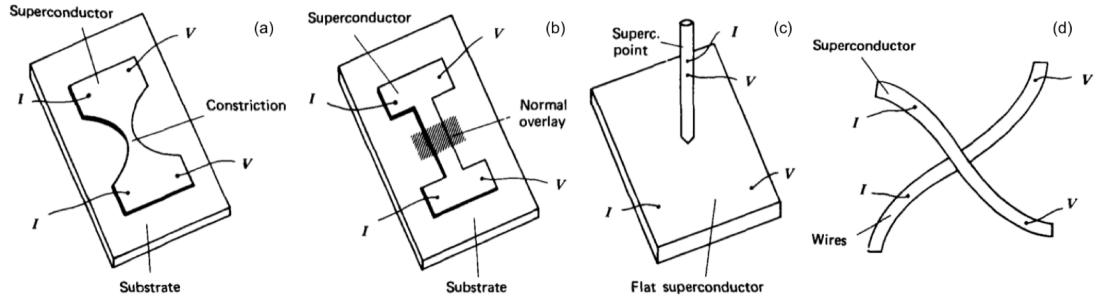

Figure 2-14: *Sketches of different Josephson junction structures. (a) A Dayem bridge junction, (b) a proximity effect junction, (c) a point contact junction and (d) a crossed wire junction. Adapted from Reference [37].*

Considering superconductors with a similar density of Cooper pairs, ρ, the tunnel current through a Josephson junction is given by

$$J_s = J_c \sin(\theta_1 - \theta_2) \tag{2.40}$$

where θ_1 and θ_2 are the order parameter phase on each side and $J_c = 2K/\rho$ with K the coupling amplitude between the two superconductors. In this case, the current depends non-linearly on the superconducting phase difference $\varphi = \theta_1 - \theta_2$. The voltage is related to the time-dependent phase by

$$\frac{\partial \varphi}{\partial t} = \frac{2eV}{\hbar}. \tag{2.41}$$

In the case where $V = 0$ the phase difference is constant though not necessarily zero. Hence, a critical current can flow through the junction without an applied voltage, known as the d.c. Josephson effect. If a constant voltage is applied, by integrating Eq. 2.41 in time, $\varphi = \varphi_0 + \frac{2eV}{\hbar}t$, we find that the tunnel current oscillates expressed as,

$$J_s = J_c \sin(\varphi_0 + \frac{2eV}{\hbar}t), \tag{2.42}$$

with a frequency $\omega = 2eV/\hbar$ which is known as the a.c. Josephson effect. The ratio between frequency and voltage is a constant given by $483.6\,\mathrm{MHz}/\mu\mathrm{V}$.

The maximum tunnelling supercurrent is modulated by a magnetic field ap-

plied perpendicular to the junction,

$$J = J_0 \left| \frac{\sin \pi \frac{\Phi}{\Phi_0}}{\pi \frac{\Phi}{\Phi_0}} \right|, \tag{2.43}$$

where $\Phi = HLd$ and $\Phi_0 = h/2e$ is the flux quantum. The junction geometry is illustrated in Figure 2-15(a) where L is the length of the junction, $d = (\lambda_L + \lambda_R + b)$ corresponds to the junction width which is the overall magnetic penetration, λ is the penetration depth, b is the barrier thickness or separation between superconductors, and H is the applied external magnetic field. The spatial modulation of the supercurrent is shown in Figure 2-15(b). The minima occur when the magnetic flux threading the junction is a multiple of the flux quantum.

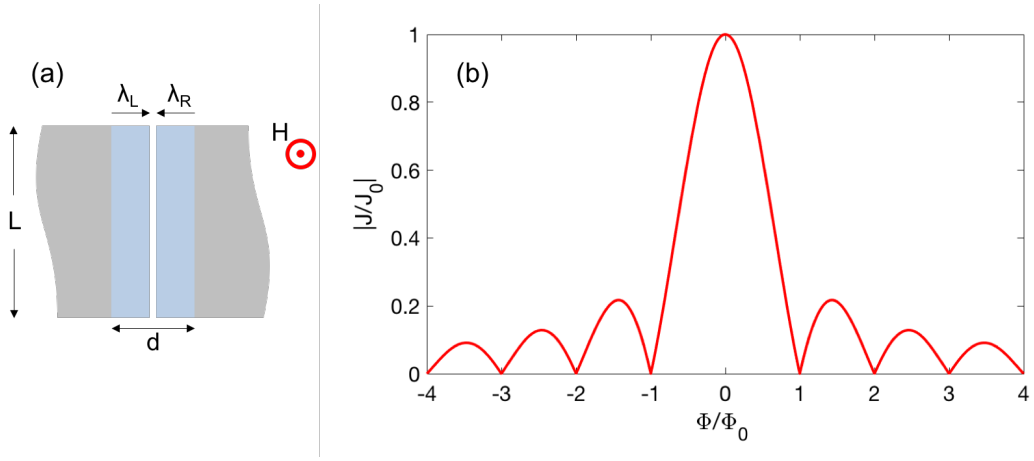

Figure 2-15: *(a) Josephson junction geometry with the relevant parameters indicated. (b) The spatial modulation of the tunnelling supercurrent by an applied magnetic field, formally similar to a Fraunhofer diffraction pattern.*

The critical current shows a Fraunhofer-like dependence on the magnetic field, analogous to a single slit diffraction pattern. When two weak-link Josephson junctions are connected in parallel in a loop, quantum interference can be observed, whereby the relative phases in the two junctions is modulated by the magnetic flux enclosed in the superconducting loop. In this case, the maximum tunnelling supercurrent is given by

$$J = 2J_0 \left| \cos \pi \frac{\Phi_f}{\Phi_0} \right|, \tag{2.44}$$

where Φ corresponds to the flux enclosed in the superconducting loop. In this case, the critical current as a function of the applied magnetic field is analogous to a double slit diffraction pattern shown in Figure 2-16.

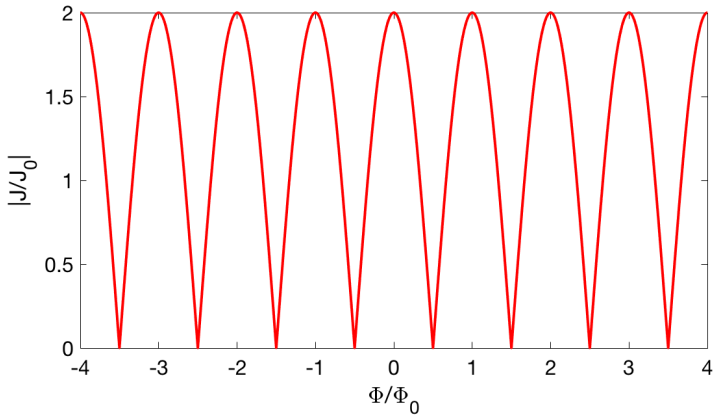

Figure 2-16: *Dependence of the critical current on the applied magnetic field for two coupled Josephson junctions forming a Superconducting Quantum Interference Device, SQUID.*

2.3.3 Superconductor-Ferromagnet Interface - FFLO state

The antagonistic nature of superconducting and ferromagnetic materials gives rise to many interesting phenomena when both are placed in intimate contact. Unlike ferromagnetic superconductors such as UGe2 [38], URhGe [39] and UCoGe [40], where superconductivity and ferromagnetism coexist, in artificial hybrid superconductor-ferromagnet structures the interaction is limited to short distances around the interfaces of the two systems [41].

A conventional superconductor adjacent to a ferromagnet experiences a Cooper pair-breaking effect due to the ferromagnet exchange field. The magnetic ordering tends to lead to parallel alignment of the electron spins which either prevents or breaks Cooper pairs, with anti-parallel spin alignment. On the other hand, superconductivity is induced in the ferromagnet as the Cooper pairs penetrate the material. Under the influence of the exchange field, the superconducting order parameter $\psi(x) = \cos(x/\xi_F)\psi_0 e^{-\xi_F x}$ exhibits damped oscillations within the ferromagnet over a characteristic length $\xi_F \sim \sqrt{\frac{\hbar D_F}{E_{ex}}}$, typically of a few nanometers.

This occurs because the up-spin electron of the pair parallel to the exchange field decreases its energy by an amount equal to the exchange energy, while the down-spin electron energy increases by the same amount, as schematically illustrated in Figure 2-17. Hence, the up-spin electron increases its kinetic energy, while the down-spin electron decreases its kinetic energy and the Cooper pair acquires a finite center-of-mass momentum, Q. Consequently, the two spin contribution to the pair amplitude varies as

$$\begin{aligned} |\psi\rangle &= \frac{1}{\sqrt{2}}(|\uparrow\downarrow\rangle e^{iQx} - |\downarrow\uparrow\rangle e^{-iQx}) \\ &= \frac{1}{\sqrt{2}}(|\uparrow\downarrow\rangle - |\downarrow\uparrow\rangle)\cos(Qx) + \frac{i}{\sqrt{2}}(|\uparrow\downarrow\rangle + |\downarrow\uparrow\rangle)\sin(Qx), \end{aligned} \tag{2.45}$$

resulting in a mixture of spin-singlet (blue) and spin-triplet (red) states with zero spin projection in the direction of magnetisation.

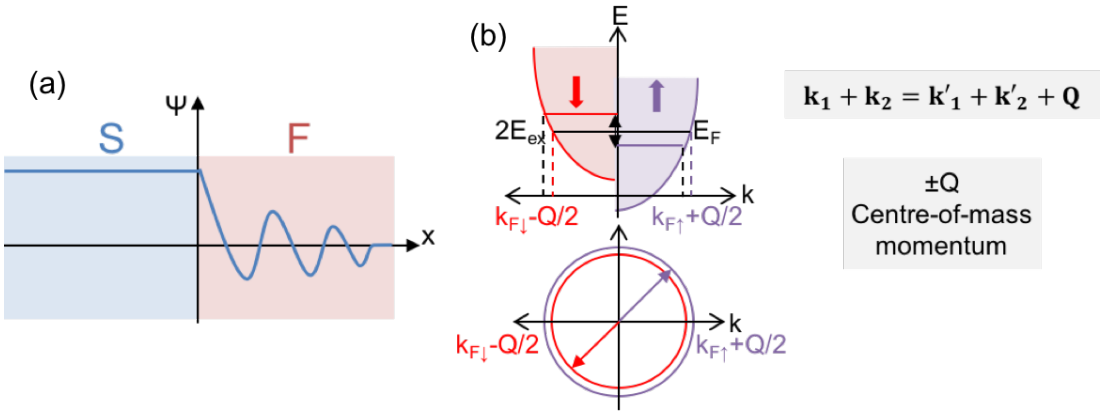

Figure 2-17: *(a) The spatial dependence of the superconducting order parameter within the ferromagnet near the superconductor interface. (b) The mechanism of $S_z = 0$ spin-triplet generation illustrated by considering the energy as a function of momentum k. Adapted from Reference [25].*

Considering the possibility of a ferromagnetic superconductor, an inhomogeneous superconducting state was proposed by A. I. Larkin and Y. N. Ovchinnikov [42] and by P. Fulde and R. A. Ferrell [43] in 1964, which is also known as the FFLO state. They predicted the appearance of a non-uniform superconducting state with a very short sinusoidal behaviour of the superconducting

order parameter over a lengthscale of the order of the superconducting coherence length ξ, involving Cooper pairs with finite momentum [1]. The modulation of the superconducting order parameter in the FFLO state arises due to the Zeeman splitting of the electron energies in the presence of a magnetic field. The FFLO state has not been found in bulk materials, but has been realised in hybrid superconductor-ferromagnet proximity effect structures.

Andreev reflection at the interface between a superconductor and a ferromagnet relies on spin-dependent effects. At the interface an incident spin-up electron from the ferromagnet is reflected at the interface as a spin-down hole. As a result, a Cooper pair of electrons with opposite spins flows in the superconductor. Therefore, both spin-up and spin-down electron bands of electrons in a ferromagnet are involved in this process [1].

2.4 The long range proximity effect - Odd frequency spin-triplet superconductivity

2.4.1 Theory and Key Experiments

First predicted by Bergeret in 2001 [5], the long range proximity effect has been identified in many experimental studies in the recent years. The mechanism for this involves the conversion of conventional s-wave superconductivity comprising of spin-singlet Cooper pairs into spin-triplet pairs with equal spins at the interface with a ferromagnet exhibiting an inhomogeneous magnetisation. Spin mixing occurs at the interface as a result of the different scattering phase shifts electrons with opposite spin acquire when scattered (reflected or transmitted) from a magnetic interface [7].

$$\begin{aligned} |\psi\rangle &= \frac{1}{\sqrt{2}}(|\uparrow\downarrow\rangle e^{i\theta} - |\downarrow\uparrow\rangle e^{-i\theta}) \\ &= \frac{1}{\sqrt{2}}(|\uparrow\downarrow\rangle - |\downarrow\uparrow\rangle)\cos(\theta) + \frac{i}{\sqrt{2}}(|\uparrow\downarrow\rangle + |\downarrow\uparrow\rangle)\sin(\theta). \end{aligned} \tag{2.46}$$

Let us first consider the symmetry properties of a pair of electrons, which are fermions and obey the Fermi-Dirac statistics and the Pauli exclusion principle. In the singlet state, we have a total spin zero and a spin projection along

the quantisation axis equal to zero, as illustrated in Figure 2-18. In order to obey the Pauli exclusion principle, the pair wavefunction must be antisymmetric under an exchange of electrons. Hence, in the singlet state the electron pair is antisymmetric under spin exchange and symmetric in space and time.

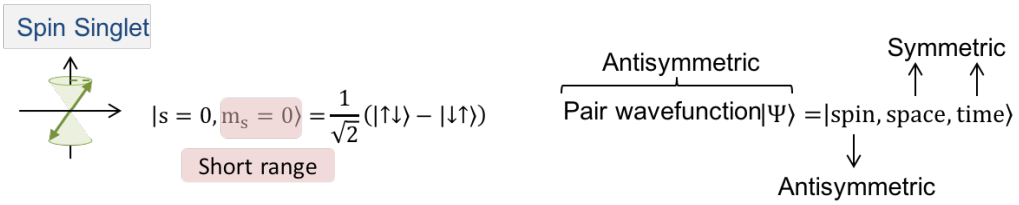

Figure 2-18: *A pair of electrons in a spin-singlet state and their total wavefunction.*

In the triplet state, we have a total spin equal to one and three possible spin projections along the quantisation axis, as illustrated in Figure 2-19. As before, the pair wavefunction must be antisymmetric under an exchange of electrons. The spin-triplet state is symmetric under a spin exchange and the electron pair is also isotropic in space, hence also symmetric. Therefore, the pair wavefunction must be antisymmetric in time, allowing odd-in-time pairing, also called odd frequency triplet superconductivity.

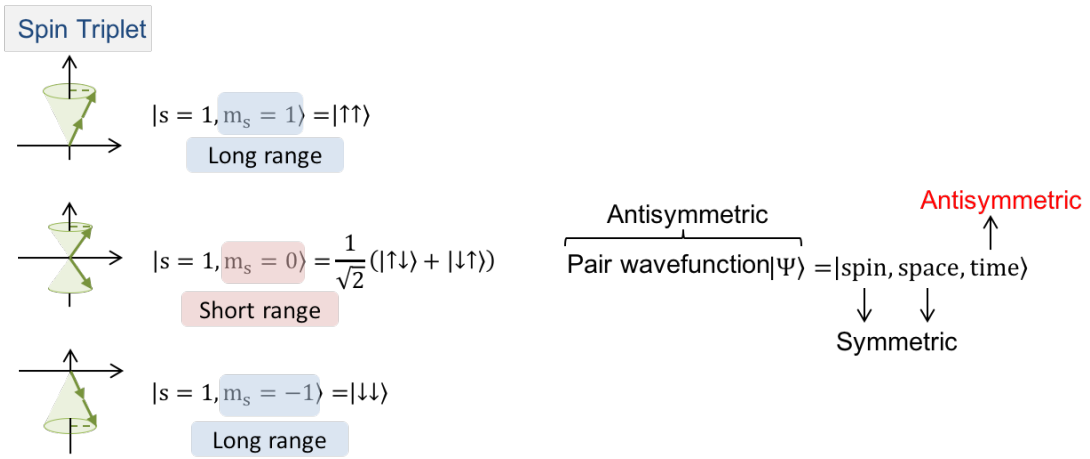

Figure 2-19: *A pair of electrons in the spin-triplet states and their total wavefunction.*

As illustrated in Figure 2-20, the singlet and triplet terms which have zero spin projection, oscillate and decay rapidly over short distances (this is the conventional proximity effect), with no immediate use in spintronics. However, spin-triplet Cooper pairs with $S_z = \pm 1$ projection and are not directly affected by the exchange field of the ferromagnet, as this no longer has a pair-breaking effect on them [6].

Note that the singlet states are the same regardless of the quantisation direction, but the three triplet states transform into each other when the quantisation direction rotates due to non-collinear magnetisation. Therefore, by having a ferromagnet at the interface with a conventional s-wave superconductor, non-collinear pairs with $S_z = 0$ projection can be generated from a spin-singlet source, and the presence of a non-collinear magnetisation, whereby the quantisation axis varies spatially, allows the quantisation axis to rotate such that $S_z = \pm 1$. These same spin pairs can survive over very much longer distances, with promising applications in spintronics [6].

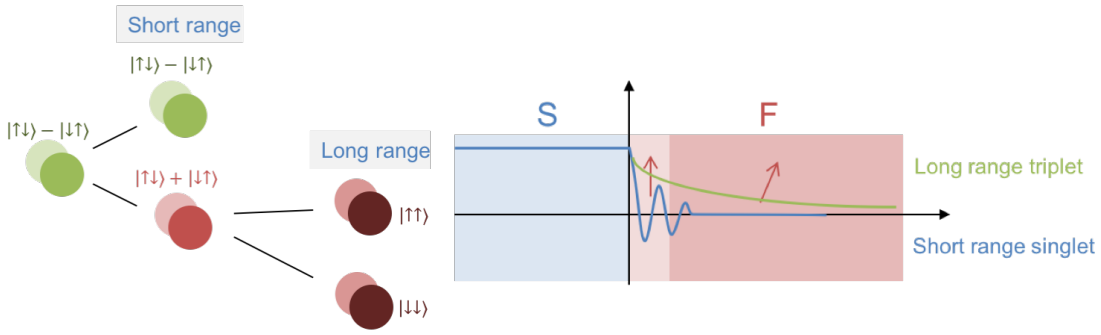

Figure 2-20: *(a) Cooper pair conversion from a spin-singlet state to a spin-triplet state with parallel spins. (b) Sketch of the order parameter within the ferromagnet for long and short range pair correlations. Adapted from Reference [38].*

Recent advances in nanofabrication and deposition techniques have allowed the engineering of new types of devices. The first experimental breakthrough was made by Keizer *et al.* [2] in 2006 when a supercurrent was measured in the half metal CrO_2, where electronic transport is metallic for the spin-up electrons, and insulating for the spin-down electrons, a characteristic of the band structure of the material.

Soon after this, it was realised that the required inhomogeneous magnetisation does not have to be intrinsic. Khaire *et al.* [3] exploited this fact by adding two extra magnetised layers which were misaligned with respect to a central ferromagnetic region and act as a spin mixer. This experiment initiated an entirely new generation of experiments focused on controlling triplet supercurrents by using multilayer structures.

Motivated by a proposal from Houzet and Buzdin [44], a spin-triplet Josephson junction consisting of two conventional superconductors coupled via a non-collinear ferromagnetic trilayer (Ho/Co/Ho) was reported by Robinson *et al.* [45]. At low temperatures Holmium becomes a conical ferromagnet, *i.e.* the atomic magnetic moments precess in a spiral from layer to layer in a cone shape. This intrinsic magnetic inhomogeneity generates equal-spin pairs and these experiments opened the door to a second type of experimental geometry that utilises intrinsically inhomogeneous magnets to controllably create long-range triplet supercurrents.

Recently, a superconductor-ferromagnet Josephson junction has been realised by Jan Aart's group in Leiden [46] that explored inhomogeneous magnetisation in the magnetic vortex of a disk-shaped ferromagnetic structure. They showed that the magnetic texture not only provides the mechanism for generating triplets but also permits control over the spatial distribution of supercurrent. Their device consisted of a disk-shaped planar Josephson junction composed of a Co/Cu/Ni/Nb multilayer. These authors observed a two-channel supercurrent flow which could only be explained by the presence of spin-triplet supercurrents. This work demonstrated that the dynamical control of the spatial distribution of the spin-polarised supercurrent is possible.

Chapter 3

Experimental Techniques and Methods

In this chapter the working principles of the main techniques and equipment used for sample fabrication and characterisation are described, and the materials and methodology used explained in detail. The chapter structure resembles the experimental timetable which in a simplified picture consisted of fabricating the samples and preparing them for the characterisation measurements by coating with a conductive metal for the scanning Hall probe imaging or wire bonding to a proper package for the electrical magnetotransport measurements in the most suitable cryogenic system available.

3.1 Sample Preparation

In this section the main techniques and equipment used for sample preparation are presented, being divided into three major processes, lithography, thin film deposition and physical etching. The last subsection is dedicated to the detailed description of the sample fabrication process for the superconductor-ferromagnet hybrid structures studied and discussed in chapters 4 and 5.

3.1.1 Lithography

The technique of lithography, from the Greek "write with stone", consisted of a process of printing text and artwork using a fine grained limestone where

the immiscibility of oil and water is exploited for content transfer. Two main lithographic techniques are described below, namely, photolithography and electron beam lithography, in which microscopic and sub-microscopic features can be achieved.

Optical Lithography

Optical or photolithography is a technique widely used in the microelectronics industry. It allows precise process and design control to achieve desired microstructures. In general, the technique requires three main elements, a photo mask, a photoresist, and a light source. First, the photo mask, which consists of a single sided chromium coated glass plate, must be prepared. The layout is created by etching the chromium film to allow the light to shine through the design of interest. The substrate is then coated with a light-sensitive polymer called photoresist, here Shipley S1813 is mainly used. The coating must be uniform with a well-defined thickness in order to produce high quality patterns. For this purpose, spin coating has been widely used, where the liquid resist is placed on top of the substrate held by vacuum then rotated about its axis several thousand revolutions per minute (rpm), usually 3000-6000 rpm. The centrifugal forces act to spread the resist which results in a thin uniform layer. The attractive molecular forces responsible for the resist viscosity reduce the thinning rate caused by centrifugal forces. Consequently, photoresists with lower viscosity but similar chemical platforms produce films with thinner thicknesses [47]. The photo mask and the photoresist-coated substrate are then aligned and placed in close contact using a Mask Aligner (Karl Suss MJ3). The aligner comprises of an ultraviolet (UV) light source (Hg lamp) and a set of mirrors and lenses to provide a uniform and stable light intensity exposure. The minimum feature size is limited by the source wavelength due to diffraction effects. UV light is then shone through the photo mask pattern onto the photoresist causing a photoreaction in the exposed areas. A solution called developer (Microposit 351) is used to dissolve the exposed areas, completing the layout transfer.

Another exposure technique which has been largely used in this work is direct laser writing (Heidelberg μPG 101). This technique eliminates the need of photo masks, where a UV laser diode at 375 nm with a beam spot of $\sim$1 μm sequentially exposes the photoresist transferring the pattern pixel by pixel. The layout is

created on the CLEWIN design software and immediately implemented. The only drawback is the long writing time which depends mainly on the layout dimensions. However, for devices produced in small amounts and with small dimensions, this layout versatility becomes an attractive feature.

Electron Beam Lithography

Fundamental in the development of submicron structures, electron beam lithography enables device fabrication using a finely-focused electron beam (∼1.5 nm) to directly write patterns containing features of just a few tens of nanometers with great accuracy. Originally developed in adapted scanning electron microscopes (SEM), this is schematically illustrated in Figure 3-1(a). It consists of a high vacuum column where an electron beam is accelerated by tens of kilovolts from a thermionic or field emission gun. The electron beam is collimated by a sequence of apertures, electromagnetic condenser lenses and scan coils to focus and guide the electron beam towards the sample. A beam blanker and a pattern generator are added to control which areas are exposed. The electrostatic beam blanker (200 V) is used to divert the electron beam from the optical axis of the SEM column, thus preventing electrons from reaching the sample. Nowadays completely dedicated equipment is available with fast processing and high resolution stages. Despite this, the technique still demands long writing times for large and complex patterns.

Similar to optical lithography, the sample is spin coated with an e-beam sensitive polymer called resist. There are two classes of e-beam resist, positive and negative, where the inelastic collisions of the incident electron beam with the resist polymer chains result in ionisation followed by physical-chemical changes. Schematically illustrated in Figure 1(b), after e-beam exposure the long chains present in the positive resist are broken into more soluble small chains. While in the negative resist the inverse process takes place, after exposure it undergoes cross-linking reactions connecting the small chains to form less soluble long chains [48]. A standard positive e-beam resist is the polymethyl methacrylate (PMMA) one of the highest resolution resists available. After e-beam exposure the PMMA polymer fragments can be dissolved in a developer solution of methyl isobutyl ketone (MIBK) and isopropanol (IPA). For thin film deposition an undercut resist profile is desirable to obtain good lift-off. This can be achieved

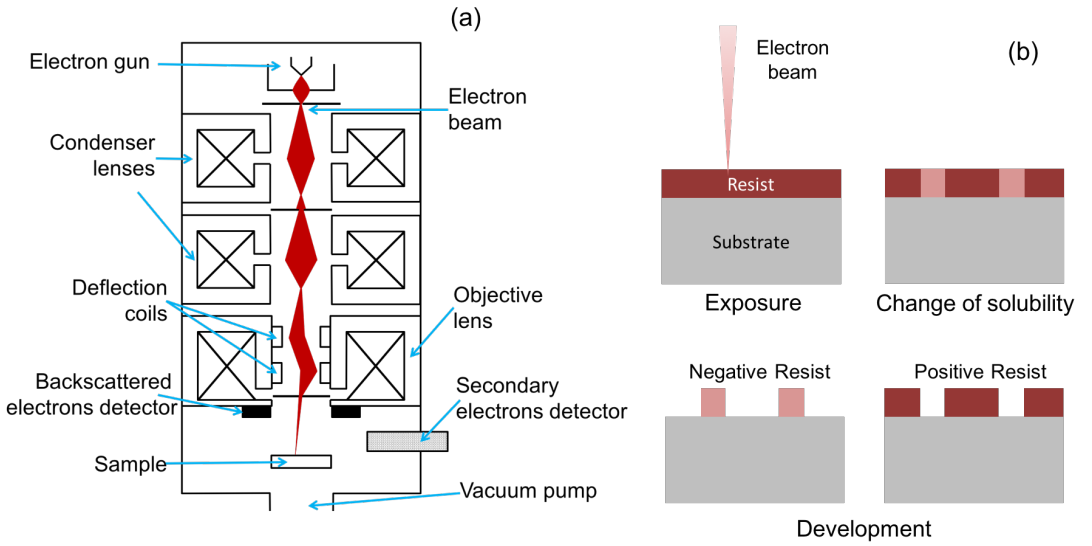

Figure 3-1: *(a) Sketch of a scanning electron microscope and its main elements. (b) Process of electron beam exposure and development of a negative and positive resists.*

by creating a double layer resist made of a low molecular weight PMMA bottom layer (P(MMA(8.5)-MAA) co-polymer) and a high molecular weight PMMA top layer (495 PMMA). P(MMA(8.5)-MAA) EL9 is a mixture of PMMA and 8.5% methacrylic acid. It is formulated mostly of Ethyl lactate (91%) and 9% of Poly(methyl methacrylate)/methacrylic acid. Higher polymer concentration provides a thicker resist layer. PMMA resist can standardly be found in two main molecular weights 495k and 950k. The resist consists of a small percentage of PMMA polymer dissolved either in Anisole (e.g., A3 - 3% in Anisole) or in Chlorobenzene (e.g., C4 - 4% in Chlorobenzene). The more e-beam sensitive bottom layer dissolves faster than the top layer in the developer solution creating an enhanced undercut which enables easier lift-off. In order to achieve cutting-edge results attention must be paid to several parameters such as, the quality of electron optics and focusing, which are crucial for precision writing. Also, beam energy, beam exposure dose, time of development and temperature are critical parameters for obtaining sharp and well defined edges.

3.1.2 Thin Film Deposition

Fundamental in the creation of new technological devices, the constantly improved thin film deposition techniques can be either a physical process, such as evaporation and sputtering, or a chemical process, such as by gas or liquid phase processes. The reactive sputtering deposition combines chemical and physical process. The following is a description of the principles and features of two essential physical vapour deposition techniques, the electron beam evaporator and the magnetron sputtering system.

Electron Beam Evaporation

In the electron beam evaporator an intense electron beam is focused onto a source material, where the kinetic energy of the electrons is transferred and transformed into thermal energy. The material vaporises and condenses on an opposing substrate, forming a thin film with increasing thickness. A schematic illustration of the main elements in an electron beam evaporator is shown in Figure 3-2. In the electron gun inside a high vacuum chamber, a stream of electrons is emitted from the tungsten filament by thermionic emission and accelerated by a 5 kV potential difference between the filament and the grid (anode). A permanent magnet is used to deflect the electron beam by 270^o to reach the source. In addition, deflecting electromagnetic coils can align and raster scan the electron beam across the source surface (XY sweep) for a more uniform energy transfer. The high energy density obtained from the accelerated electron beam makes the technique ideal for high melting point materials like titanium. The source material is heated within a crucible, made of a compatible material, placed on a water-cooled copper hearth. This allows low contamination, as it prevents the crucible material diffusion into the source material.

Magnetron Sputtering Deposition

Magnetron sputtering is a technique known for its controlled and uniform deposition. It is a powerful tool for depositing high quality thin films from a broad variety of materials. It can deposit not only metallic and insulating materials but, also, more complex materials such as, alloys and compounds. The sputtering process occurs by ion bombardment of the target source material. The atoms at the

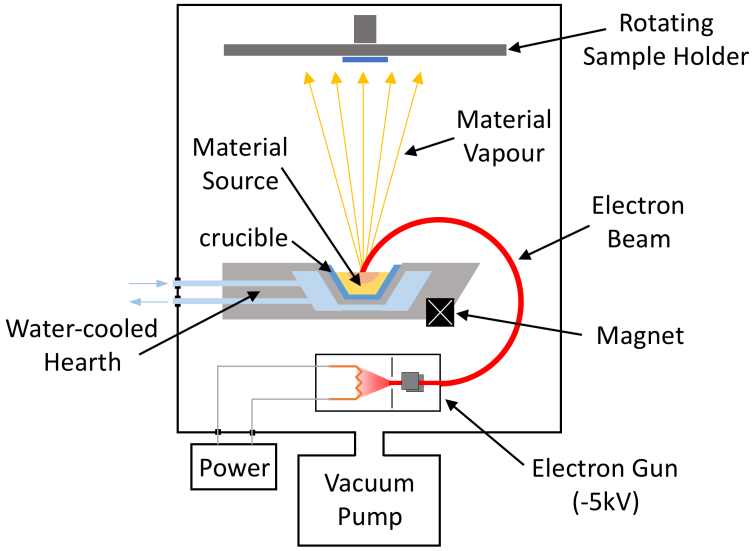

Figure 3-2: *Schematic representation of an electron beam evaporator with the main components indicated.*

target surface are physically ejected when the energy and momentum transferred from incident ions, overcomes the chemical binding energy of the material and directs them away from the surface [49].

Inside a high vacuum chamber, the target material is mounted on a negatively charged magnetron cathode and the substrate is place on a positive anode, as illustrated in Figure 3-3. The magnetron design comprises of permanent magnets, placed closely behind the target, and arranged in a way to confine the magnetic field lines to a circular ring near the target [50]. A chemically inert gas (Argon) is introduced as the sputtering agent, to be ionised and accelerated, creating a sustainable plasma glow discharge. Power can be delivered by a direct current (DC) source for conductive targets or radiofrequency (RF) source for insulating targets. In the first case, the free electrons in the conductive target are discharged and accelerated toward the substrate by the high potential difference with enough kinetic energy to ionise the argon atoms. Conversely, the argon ions will be accelerated toward the negative target with sufficient energy to eject the source material. A magnetron configuration is used to trap the electrons in the magnetic field lines simulating a local increase in the chamber pressure near the target. The electrons accelerated by the electric field ($\mathbf{E}$) perform a helical motion around the

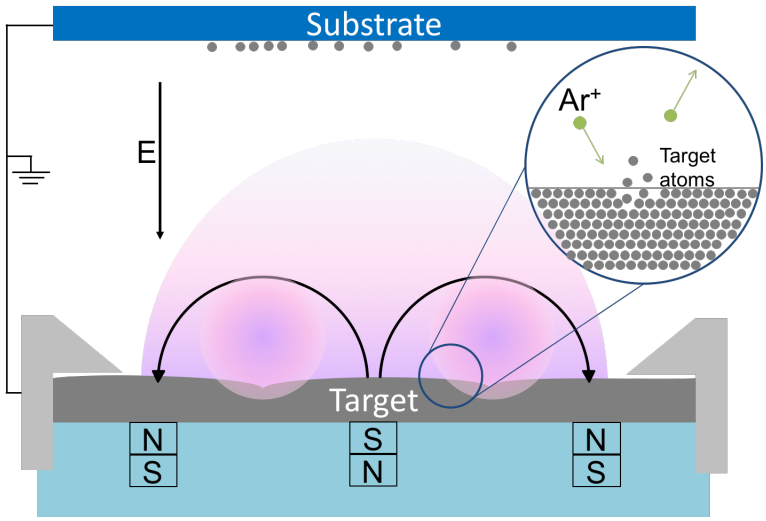

Figure 3-3: *Schematic illustration of a magnetron sputtering head and the sputtering process.*

magnetic field lines (**B**) due to the Lorentz force, $\mathbf{F} = -e(\mathbf{E} + \mathbf{v} \times \mathbf{B})$, where e and v are the electron charge and velocity, respectively. This magnetically enhances the plasma producing a high ion density and high sputter removal rates. However, for insulting materials the plasma discharge cannot be sustained, and an RF power (13.56 MHz) source is used. The target acts as a coupling capacitor to the plasma. The electrons will oscillate in the magnetic confinement region with enough energy to sustain the ionisation and the plasma. The RF source requires an automatic impedance matching network because the plasma will not have a constant impedance but will vary with its operating conditions [51].

Even though sputtering is a purely physical process, chemistry can be added by introducing a mixture of argon and a reactive gas like oxygen or nitrogen. The proportion between the gas species will dictate the reaction with the target and the deposition parameters used. In the work presented here, oxygen gas has been used to create an O_2 plasma to oxidise a nanometre thin aluminium layer, to obtain a thin uniform Al_2O_3 layer.

3.1.3 Physical Etching Techniques

In order to create clean interfaces between materials it is sometimes desirable to create the structures of interest only after thin film deposition of the material. For this purpose, dry and wet etch processes, *i.e.* physical and chemical etching, are generally used. In the former technique, the material is physically removed by sputtering or eroded by reactive ions. The latter is considered the simplest etching technology and uses chemical solutions to selectively etch a material. Two standard physical etching techniques have been used to fabricate the superconductor-ferromagnet Josephson Junctions and these are described below.

Ion Beam Etching

In ion beam etching, the physical principle of sputtering is exploited to perform controlled, highly anisotropic and nonselective material ablation. The collimated ion beam generated by an ion source inside a vacuum chamber is directed onto a tilted mount that slowly rotates the sample etching the exposed surfaces, as illustrated in Figure 3-4. In the ion source, argon gas is ionised into a plasma by the electrons emitted from the tungsten filament cathode and radially accelerated to the cylindrical anode. The argon ions are accelerated and extracted through a pair of optically-aligned carbon grids providing a well-collimated beam. To reduce the electrostatic divergence at the beam and avoid charge accumulation on the sample, a cloud of electrons, thermally emitted by a tungsten filament located in front of the grids, neutralise the ion beam and the sample surface. The number of atoms sputtered divided by the number of incident ions defines the sputtering yield. A thin hard mask with a very low sputtering yield, such as titanium, is commonly used for high resolution pattern transfer. The sample is tilted between 10^o to 30^o from the incident beam plane to avoid sidewall coating due to redeposition. The directional ion beam provides no mask undercut in stark contrast to isotropic etching with wet chemistry. The mechanical nature of ion beam etching is reflected in its ability to etch any material, controlled by calibrated etching rates based on each material's sputtering yield.

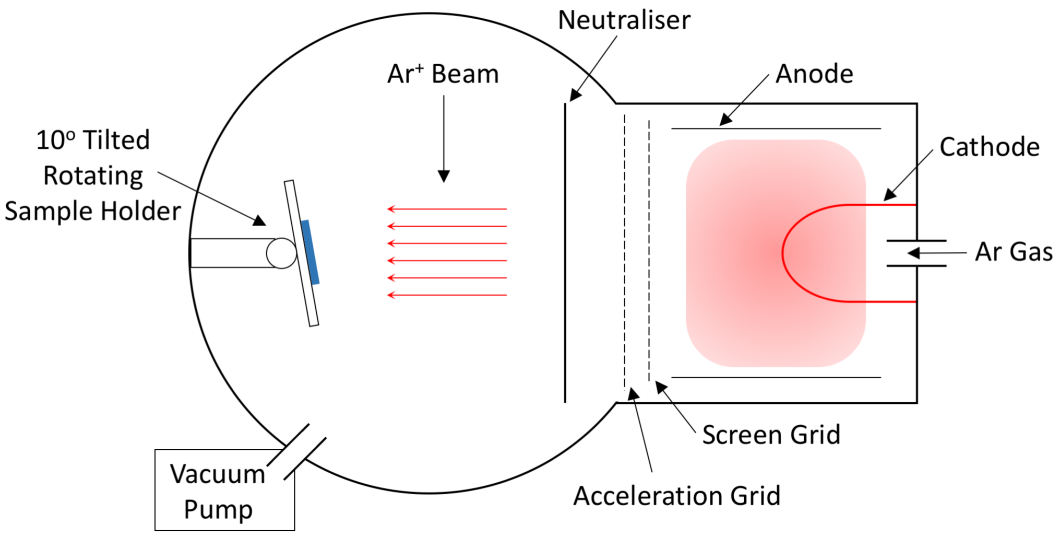

Figure 3-4: *Schematic illustration of the Ar ion beam miller with the main components indicated.*

Focused Ion Beam

Micromachining, high-resolution imaging and ion-beam activated deposition can be achieved in a single platform, the focused ion beam (FIB) microscope. Similar to the scanning electron microscope (SEM), in the FIB microscope a beam of ions instead of a beam of electrons, is generated, collimated and accelerated inside a high-vacuum column (10^{-7} mbar) to reach the sample with a highly focused beam of $\sim$5 nm diameter [52]. A very low ion beam emission current is made possible by using a field ionisation source, the liquid-metal ion source (LIMS), schematically illustrated in Figure 3-5. Gallium (Ga) is the most commonly used metal due to its low melting point (29.8^{o}C), low vapour pressure and low volatility. The source consists of a coil wrapped Ga reservoir connected to a blunt tungsten needle. The reservoir is heated by applying a current to the coil so that the liquid Ga flows to the needle tip. The Ga ions are electric field extracted by the large negative potential ($\sim$30 kV) applied between the needle and the extraction electrode. A Taylor cone made of liquid Ga forms on the needle tip by the balance between electrostatic forces and surface tension, this produces an ion extraction current of $\sim$2 μA with a very fine beam diameter. A set of apertures, lenses and deflection plates define, focus and raster the ion beam onto the sample. Electrostatic lenses

are employed instead of the commonly used electromagnetic lenses in the SEM. The electromagnetic focusing strength depends on the charge/mass ratio of the particle, and would demand unpractically massive lenses for ion beams. The accelerated Ga ions reach the sample with high kinetic energy and momentum, causing a collision cascade through a series of elastic and inelastic interactions, whereby sample surface particles are sputtered, electrons are emitted and Ga atoms are incorporated. Depending on the material properties a 10 nm minimum feature size can be achieved by FIB milling.

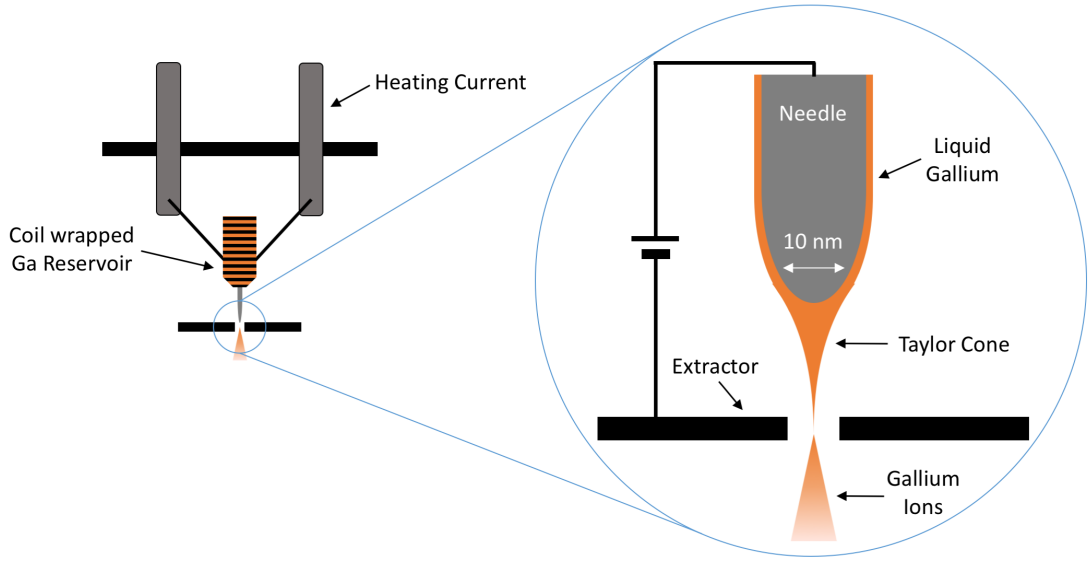

Figure 3-5: *Illustration of a focused ion beam with a Ga tip structure and the ion beam extraction method.*

Imaging is based on the detection of low-energy ion-induced secondary electrons (ISE) and not only provides surface topographic information but also contrast from different crystal orientations. Superficial sample damage takes place during FIB imaging. Hence, in order to achieve minimal sample damage and precise milling conditions, modern dual-beam platform instruments (FIB-SEM) are used, where a FIB column and a SEM column combine into a single microscope. In addition, a gas injection nozzle enables local ion-induced chemical vapour deposition (CVD) of metals such as tungsten (W) and platinum (Pt), and insulators such as silicon dioxide (SiO_2). The organometallic precursor gas is in-

jected by the nozzle which adsorbs on the sample surface. The incident ion beam activates a chemical reaction decomposing the adsorbed gas to form a thin film on the sample surface [53]. In the work here presented, a FEI Helios dual-beam microscope has been used to safely image and precisely mill specific areas in the samples with well-controlled depths.

3.1.4 Fabrication Procedures

Here a detailed description of the fabrication steps is given for the two hybrid systems studied, the superconductor-ferromagnet hybrid arrays and the superconductor-ferromagnet Josephson junctions.

Superconductor-ferromagnetic hybrid arrays

The superconductor-ferromagnet hybrid arrays have been grown on thermally oxidised Si substrates (90 nm SiO_2). The substrates have been degreased and cleaned by a standard cleaning procedure, and spin coated with a copolymer/PMMA double layer resist. Electron beam lithography has been used to write a 1x1 mm^2 pattern composed of a 4 μm period square array of 1 μm diameter disks. These fabrication steps are described in detail in Table 3.1.

Table 3.1: *Fabrication steps for lithographic patterning of the superconductor-ferromagnet hybrid arrays.*

Step	**Description**	**Process/Material**	**Parameters/Action**
1	Substrate cleaning	Trichloroethylene Acetone Isopropyl alcohol (IPA) Nitrogen gas	5 min at 60% power 5 min at 60% power 5 min at 60% power Blown dry
2	Co-polymer coating	P(MMA(8.5)-MAA) EL9	3000 rpm
3	Co-polymer baking	Oven	25 min at 120^{o}C
4	PMMA coating	495 PMMA A3	3000 rpm
5	PMMA baking	Oven	35 min at 155^{o}C
6	Double resist exposure	E-beam lithography	25 kV, 450 μC/cm^2
7	Double resist development	MIBK:IPA	1:3 solution for 5 sec
8	Sample finishing and drying	IPA Nitrogen gas	Rinse for 20 sec Blown dry

A 50 nm ferromagnetic Permalloy ($Ni_{81}Fe_{19}$) film has been deposited on the

patterned substrates at a total base pressure of 10^{-10} mbar by a dedicated magnetron sputtering deposition system called Hammer at the University of Leeds. After lift-off in acetone using mild ultrasonic excitation, the samples were loaded onto the sample holder of a second magnetron sputtering deposition system called IVOR. On one sample, a 100 nm superconducting Niobium thin film has been grown directly on top of the ferromagnetic disk array. On a second sample, in order to suppress the exchange-mediated Cooper pair breaking between the ferromagnetic disks and the superconducting film, a thin aluminium oxide (Al_2O_3) dielectric layer has been grown before the 100 nm Niobium thin film deposition. The dielectric layer has been realised by O_2 plasma oxidation of a 1.6 nm Aluminium film. A schematic representation of the sample structures can be seen in Figure 3-6. Finally, Ge(20 nm)/Au(50 nm) was thermally evaporated over the entire sample. Germanium provides good adhesion for the conductive gold layer that facilitates the approach of the tunnelling tip integrated into the Hall sensor prior to magnetic imaging.

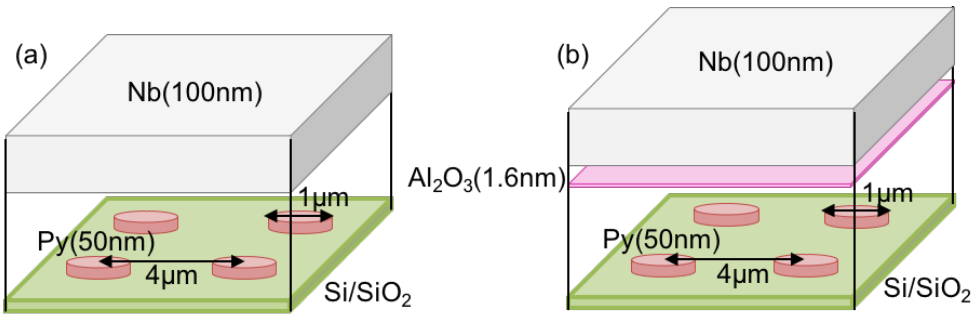

Figure 3-6: *Schematic representation of the two superconductor-ferromagnetic hybrid arrays fabricated, (a) Py(50 nm)/Nb(100 nm) and (b) Py(50 nm)/ Al_2O_3(1.6 nm)/Nb(100 nm).*

Superconductor-ferromagnet Josephson Junctions

A clean interface between superconductor and ferromagnet is paramount for generating spin-polarised supercurrents. Hence, the superconductor-ferromagnetic Josephson junctions were fabricated by etching the junction pattern through thin film layers consisting of a 50 nm Permalloy bottom layer and a 50 nm Niobium top layer. The thin films were grown on thermally oxidised Si substrates (90 nm

SiO_2) by the magnetron sputtering system called IVOR at the University of Leeds. The system reached a 10^{-9} Torr total base pressure and the Nb target had 99.9995% purity. The thinner superconducting layer in this case provides a smaller spin-singlet reservoir to aid in probing the spin-polarised supercurrents generated.

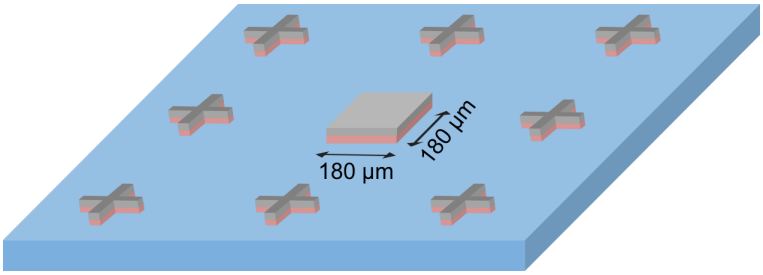

Figure 3-7: *Illustration of the alignment crosses and central square after Ar ion milling of the Py/Nb thin films (Not to scale).*

In order to facilitate alignment during the electron-beam lithography of the junction hard mask, alignment crosses and a 180x180 μm^2 central square have been defined by Ar ion milling the rest of the film away, as illustrated in Figure 3-7. This has been achieved by creating a S1813 resist mask of the crosses and the central square by direct laser writing, with the fabrication steps shown in Table 3.2. After etching the exposed areas, the photoresist mask was removed with acetone with mild ultrasonic agitation.

Table 3.2: *Fabrication steps for photolithographic patterning of the alignment crosses and the central square.*

Step	**Description**	**Process/Material**	**Parameters/Action**
1	UV resist coating	Shipley S1813	4000 rpm (~1.2 μm)
2	UV resist baking	Oven	30 min at 90°C
3	UV resist exposure	Direct laser Writer	25 W, 45%(15% filter)
4	UV resist development	351 developer:DI H_2O	1:3.5 solution for 45 sec
5	Sample finishing and drying	DI H_2O Nitrogen gas	Rinse for 30 sec Blown dry

A thin hard mask for the junctions has been used to achieve good pattern

transfer. The fabrication process is schematically shown in Figure 3-8. First, the junction pattern was defined by electron-beam lithography inside the central square following similar fabrication steps used for writing the array pattern described in detail in Table 3.3. Second, 10 nm Aluminium and 60 nm Titanium films have been deposited by e-beam evaporation to create the hard mask. Titanium has a very low etching rate which is approximately half the Permalloy and Niobium etching rates. Finally, after etching through both Permalloy and Niobium films using the Ar ion miller, the remaining hard mask is removed. The Titanium film is lifted-off by wet etching the Al layer with a MF319 developer, which contains a low concentration of tetramethylammonium hydroxide (TMAH).

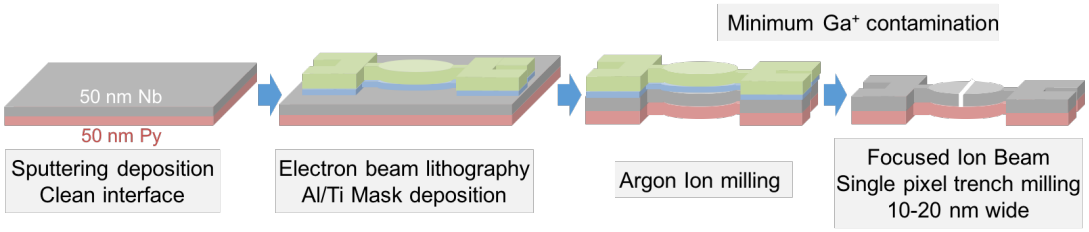

Figure 3-8: *Representation of sequential sample fabrication processes of the superconductor-ferromagnet Josephson junctions.*

In order to connect the central structures to a package, conductive Au leads were fabricated creating a suitable area for wire bonding. Direct laser writing was used to define these lead patterns. The samples were spin coated with Shipley S1813 photoresist following a similar procedure to the one described in Table 3.2. Perfect alignment on the scale of a few micrometer wide leads in the central area could be achieved by dividing the pattern into two parts. One part comprises the area close to the central structures where alignment is critical. The other area corresponds to the rest of the leads which overlaps the first part by a few micrometers, as shown in Figure 3-9. Subsequently, 15 nm Chromium and 200 nm Gold were deposited by e-beam evaporation, followed by lift-off in acetone with mild ultrasonic agitation. Finally, the last step consisted of milling a fine trench (single pixel line) in the centre of the disk across the Nb layer using a focused ion beam to create the actual planar Josephson junction. Different depths ranging from 40 nm to 60 nm were milled and the true depth estimated using simulation

Table 3.3: *Fabrication steps for lithographic patterning of the superconductor-ferromagnet Josephson junctions.*

Step	Description	Process/Material	Parameters/Action
1	Substrate cleaning	Trichloroethylene Acetone Isopropyl alcohol (IPA) Nitrogen gas	5 min at 60% power 5 min at 60% power 5 min at 60% power Blown dry
2	Co-polymer coating	P(MMA(8.5)-MAA) EL9	5000 rpm (∼300 nm)
3	Co-polymer baking	Hot plate	3 min at 180^{o}C
4	PMMA coating	495 PMMA A3	5000 rpm (∼100 nm)
5	PMMA baking	Hot plate	3 min at 180^{o}C
6	Double resist exposure	E-beam lithography	30 kV Dose 450-480 μC/cm^2
7	Double resist development	MIBK:IPA	1:3 solution for 6 sec
8	Sample finishing and drying	IPA Nitrogen gas	Rinse for 20 sec Blown dry

software.

3.1.5 Packaging and Wire Bonding

Once the sample fabrication was completed, samples need to be properly attached to the measuring system for device evaluation. For electrical magnetotransport measurements at low temperatures, Kyocera ceramic dual inline packages (C-DIP) with 20 Au-plated pins have been primarily used. The packages are made of aluminium oxide (Al_2O_3) layers. Commonly referred as alumina, polycrystalline aluminium oxide (Al_2O_3) has good thermal conduction and low electrical conductivity, being a cheap and suitable choice for packages. The package design provides a distance of approximately 0.5 mm between sample and Copper mounting surface, which allows good thermal contact. The sample is attached to the package by a thin GE varnish layer which takes approximately 30 minutes to be fully dry. The sample Cr/Au conducting pads are connected to the package leads by wire bonding.

Wire bonding is a solid phase welding technique used to interconnect pads using a thin conductive wire. The main wire bonding process used was the

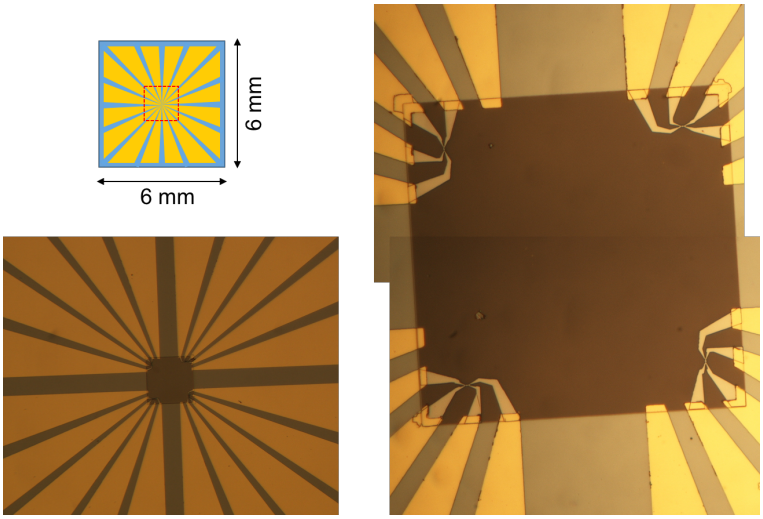

Figure 3-9: *Direct laser writer pattern breakdown at the dotted red line to achieve best alignment and overlay on the four junction leads.*

ultrasonic bonding. It uses ultrasonic vibration and lower bonding pressure at room temperature to produce a metallurgical bond in a short time. A wire bonding technique called wedge bonding was used, that is named after the shape of the bonding tool, a wedge. Throughout this work, the ultrasonic bonding process using a wedge bonding technique was mainly used to interconnect sample and package via a 25 μm diameter Au wire that provides the required current-carrying capacity.

3.1.6 Cryogenic Systems

Three cryostats with variable temperature inserts (VTI) have been used throughout this project, and their main features are illustrated in Figures 3-10 and 3-11. The Cryogenics^{TM} cryostat, schematically shown in Figure 3-10(a), has a single 9.3 litre reservoir and is equipped with two Helmholtz copper coils, one 5.5 mT out-of-plane coil and a 360^o 70 mT in-plane coil. This configuration allows simultaneous in-plane and out-of-plane magnetic fields to be applied. Figure 3-10(b) illustrates the Oxford cryostat which has a single 24 litre reservoir and a 7 T out-of-plane NbTi superconducting coil. Both Cryogenics^{TM} and Oxford cryostats have a single reservoir for cryogenics and follow a similar procedure for sample

cool down. After inserting the sample in the VTI and back-filling a clean 200 mbar He atmosphere, the reservoir is first filled with liquid N_2 and the sample cooled down to a temperature of 77 K. The liquid N_2 is then flushed and pumped out so that liquid He can be transferred to the same reservoir and the sample cooled down to 5 K. The low He gas pressure atmosphere allows a weakly coupled heat exchange between the sample and the liquid He reservoir. This allows accurate temperature control of the sample with the use of a heater attached to the cryostat. These two cryostats were mainly used in the low temperature scanning Hall probe microscopy studies.

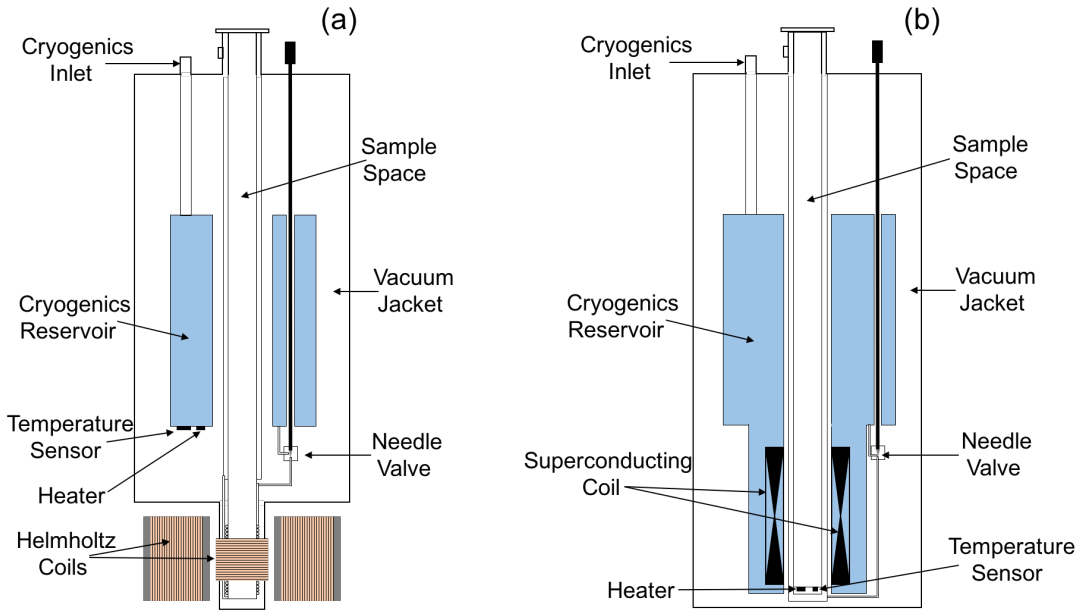

Figure 3-10: *(a) CryogenicsTM cryostat and (b) Oxford Cryostat designs with their main components indicated.*

A glass cryostat has also been used which has a double layer reservoir consisting of an outer liquid N_2 layer and inner liquid He layer, shown in Figure 3-11. Around the variable temperature insert (VTI) a commercial 1 T NbTi superconducting coil is found. The Glass cryostat is capable of reaching lower temperatures down to 2 K by pumping the liquid He reservoir. Similarly, the sample space is also filled with a 200 mbar He gas pressure atmosphere for effective heat exchange. The Glass cryostat was the main cryostat used in the low temperature

magnetotransport characterisation of the superconductor-ferromagnet Josephson junctions.

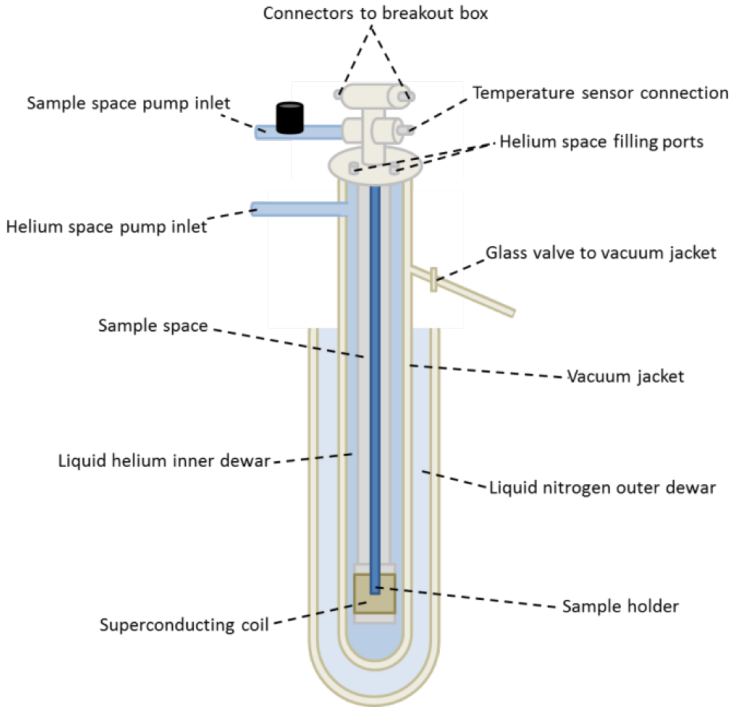

Figure 3-11: *Glass cryostat design with main components indicated.*

3.1.7 Scanning Hall Probe Microscopy

To investigate vortex phenomena in superconductor-ferromagnet hybrid structures scanning Hall probe microscopy (SHPM) was employed. SHPM is a quantitative and non-invasive imaging technique with high field sensitivity and submicron spatial resolution that allows high quality mapping of surface magnetic stray fields at microscopic scales.

First developed by Chang et al. [54, 55] and further improved by Bending's group [56–58], the technique uses Hall effect sensors made of doped semiconductor heterostructures ($GaAs/Al_{0.3}Ga_{0.7}As$) [59] which contain a two dimensional electron gas (2DEG) layer which is ideal for low temperature magnetic flux sensing. A review of the scanning Hall probe technique and other magnetic probe systems can be found in Reference [60].

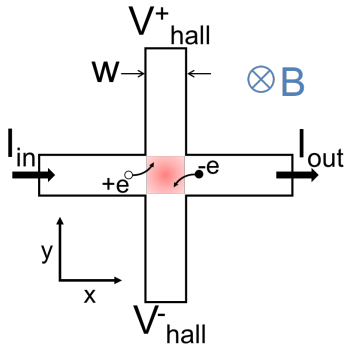

Figure 3-12: *Simplified geometric representation of a 2D Hall sensor with active area indicated in red.*

The basic Hall sensor geometry consists of two intersecting leads forming a cross with a central active area, a sketch is shown in Figure 3-12. The charge carries (q) in the constant current flowing in one of the leads experience a Lorentz force in the presence of a uniform magnetic field ($\mathbf{B}$) perpendicular to the plane of the leads. The Lorentz force drifts the carriers creating a Hall voltage (V_H) across the second pair of leads. Assuming that the voltage leads are much longer than their width (w) and that the charge carriers are in dynamic equilibrium, the Lorentz force can be equated to the electric force acting on the carriers due to the Hall electric field ($\mathbf{E}$) from the accumulation of carriers. This, can be written as

$$q\mathbf{E} = -q(\mathbf{v_q} \times \mathbf{B}) \tag{3.1}$$

where $\mathbf{v_q}$ is the charge carrier velocity. Using the current density expression ($\mathbf{J} = qn_{2D}\mathbf{v_q}$) where n_{2D} is the 2D charge concentration, and considering the 2D representation shown in Figure 3-12, the Hall coefficient (R_H) can be written as

$$R_H = \frac{1}{qn_{2D}} = \frac{E_y}{J_x B_z} \tag{3.2}$$

This shows that, in a constant current J_x, a Hall cross with lower carrier concentration provides a larger Hall coefficient, and consequently an increased field sensitivity. Several materials with low carrier concentration have been studied over the years such as Bi, Si, GaAs and several heterostructures [61]. However,

GaAs/AlGaAs heterostructures have shown to be the best material for low temperature Hall probes due to its very low 2D carrier density and very high carrier mobility. The last property provides a low resistance which produces sensors with good signal-to-noise ratio (SNR) and low Johnson noise in devices with reduced active areas, *i.e.* higher spatial resolution.

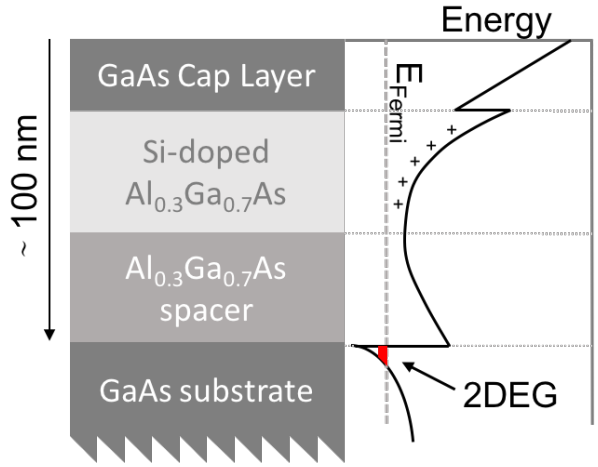

Figure 3-13: *GaAs/AlGaAs heterostructure and its corresponding conduction band energy diagram.*

In the GaAs/AlGaAs heterostructure, the 2DEG charge carriers are physically and permanently separated by an undoped AlGaAs spacer layer from their donor ions, exhibiting typical densities of $n_{2D} = 10^{15}\,\mathrm{m}^{-2}$. The whole structure can be considered as a single crystal with a modulated conduction band edge energy since the lattice constants of GaAs and AlGaAs are practically identical while the conduction band of GaAs and $Al_{0.3}Ga_{0.7}As$ lie at different energies, creating a V-shape potential well at the interface, as shown in Figure 3-13. A diffusive equilibrium is reached as the electrons thermally released from their Si donors migrate to the lower energy potential where they are restricted to a narrow layer in the z direction but free to move in the xy plane, and their high mobility ($\mu > 100\,\mathrm{m}^2/\mathrm{V.s}$ at 4.2 K) arises from the spatial separation from ionised donors, greatly reducing the ionised impurity scattering [62].

The Hall probes used throughout this project were fabricated in Bath using out-sourced GaAs/$Al_{0.3}Ga_{0.7}As$ wafers patterned by optical and e-beam lithography and wet chemical etching. The Ohmic contact to the 2DEG was made by

annealed Au/Ge/Ti/Au pads which can be seen in Figure 3-14(a). An extra lead connects a tunnelling tip (Ti/Au) for sample surface detection ensuring a safe approach. The Hall sensor active area is defined at the intersection of two 0.7 μm wide wires forming a cross. Accounting for edge depletion after wet etching, the expected spatial resolution is about 0.5 μm for the sensors used. The cross is located $\sim$5 μm from the Au coated corner of a deep mesa etch, that serves as an integrated STM tip.

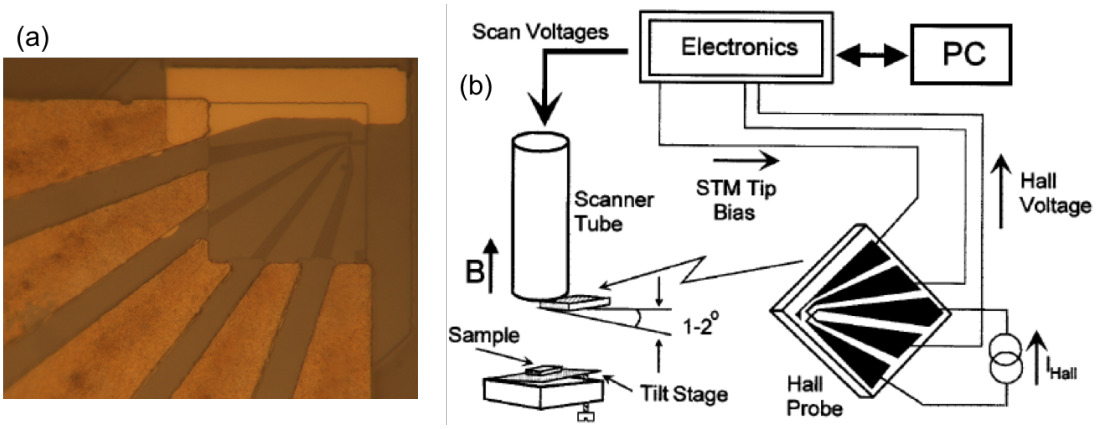

Figure 3-14: *(a) Optical image of a Hall probe of estimated 0.5 μm spatial resolution. (b) Schematic representation of the general SHPM setup. Reproduced from Reference [60].*

For low temperature measurements the Hall probe microscope head is inserted in one of the cryostats described in section 3.2. A schematic illustration of the SHPM system is given in Figure 3-14(b). The sample is mounted with a tilt angle of 1^o-2^o with respect to the Hall probe to ensure that the closest point to the sample is always the tunnelling tip. The Hall probe is mounted directly on the piezoelectric scanner tube. The whole system is controlled using a Nanomagnetic Instruments^{TM} system microcontroller. The sample is approached until a tunnel current is established and then retracted to a safe distance to initiate the 'rapid flying' scanning mode. The piezoelectric material has a reduced coefficient at low temperatures which is reflected in the scan area being limited to approximately 17 μm at 77 K and 7 μm at 5 K. This is the main technique used to characterise the superconductor-ferromagnet arrays and the 2G-HTS tape, further technical specifications are detailed in Chapter 4 and 6, respectively.

3.1.8 Electrical Magnetotransport Measurement

The measuring setup was designed to characterise the magnetotransport properties of the fabricated superconductor-ferromagnet Josephson junctions. Measurements were performed at the University of Bath in the glass cryostat described above. Each sample contained four Josephson junctions. They were mounted and wire bonded to a C-DIP package with the sample out-of-plane direction vertical and parallel to the measuring stick. The measurements were performed in a 4-point configuration using a constant AC current source (32 Hz - voltage source with a large series resistor) supplied by a Stanford Research 830 digital lock-in amplifier. The resulting voltage signal was detected by the same instrument. The instrument lines were connected to the device contacts by a breakout box. A KEPCO bipolar DC power source supplied a DC current for the superconducting solenoid. The circuit diagram of the setup is shown in Figure 3-15. Extreme care was taken to keep the Josephson junctions grounded at all times when not being measured, as electrostatic discharges can potentially damage them. In order to keep the measurement lines continuously grounded we have attached BNC T-pieces on every line and connected terminating resistors on the T-pieces before disconnecting any of the measurement lines. The data acquisition and experimental measuring routine were controlled and automated with a LabVIEW programme. This setup allowed us to probe the Josephson junction resistance as a function of temperature, the resistance as a function of a sweeping out-of-plane magnetic field at different temperatures and also the superconducting critical current as a function of an out-of-plane magnetic field.

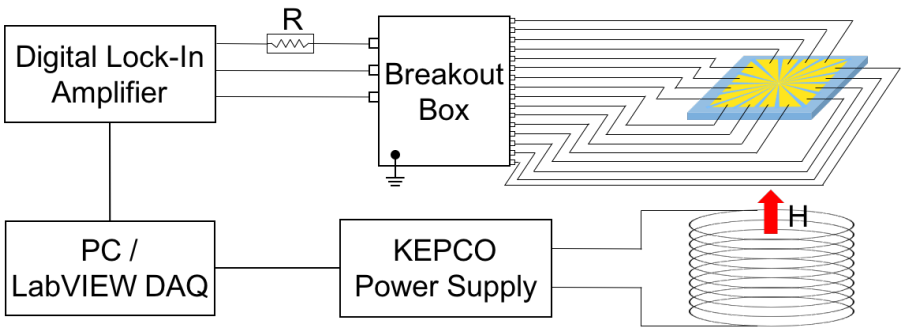

Figure 3-15: *Diagram of the electrical magnetotransport measurement setup. In reality, the sample sits on a measuring stick inside the glass cryostat (not represented here).*

Chapter 4

Vortex Matter in Superconducting-Ferromagnetic Hybrid Arrays

4.1 Introduction

The opposite ordering nature of superconductivity and ferromagnetism allows many fascinating phenomena to arise when the materials are in close contact. The phenomena of domain-wall superconductivity [63] and field-induced superconductivity [64][2] contributed to our understanding of the physics of hybrid superconductor-ferromagnet structures. However, the systematic control of superconducting vortices using nanofabricated pinning landscapes remains a major challenge for both fundamental science and applications in high current conductors. Indirect measurements [65, 66] have mainly been used to explore the influence of size, spacing and material properties of the ferromagnetic pinning structures [23, 67]. By direct vortex imaging, we demonstrate that the pinning landscape in hybrid samples can be sensitively tuned by controlling the magnetic states of permalloy (Py) ferromagnetic disks. Previous theoretical studies [68, 69] have elucidated the interaction between superconducting vortex lines and analogous ferromagnetic structures, however these have not been experimentally demonstrated yet. Our implemented hybrid structure has several sources of vortex pinning including the local suppression of superconductivity due to

exchange-mediated Cooper pair breaking, corrugations in the superconducting Nb film due to the underlying Py disks and local weakening of the superconducting order parameter by the magnetic stray fields of the disks [70]. We have carried out a systematic study that enabled us to differentiate between different contributions from the magnetic and electronic interactions between the superconducting and ferromagnetic sub-systems. In addition to the improved vortex pinning that arises in hybrid structures, the magnetic structure of the ferromagnet can also play a very important role. In the last decade a fascinating phenomenon called the long range proximity effect has been reported [5, 6]. In ferromagnetic structures similar to those studied here, the effect of non-collinear magnetic moments can lead to spin triplet Cooper pair correlations and long range superconducting currents that are not suppressed by the local exchange field [7].

Hybrid arrays have been realised in order to study the interplay between superconducting and magnetic vortices. The structures were produced by electron-beam lithography and magnetron sputter deposition and consisted of a $4\,\mu$m period square array of $1\,\mu$m diameter, 50 nm high ferromagnetic Py ($Ni_{81}Fe_{19}$) disks on a thermally oxidised Si substrate (90 nm SiO_2), as illustrated in Figure 4-1(a). A cloverleaf-like stray magnetic field distribution was observed in the ferromagnetic Py disks arising from a weak magnetic anisotropy, which is somewhat different from the usual flux-closed magnetic vortex structures observed in disks of this size and shape [28, 30, 71, 72]. A 100 nm superconducting Nb thin film has been deposited directly on top of the array by sputter deposition. Superconducting vortices are expected to be induced and pinned in the Nb thin film by the out-of-plane stray magnetic fields of the ferromagnetic Py disks. Lastly, the entire sample was coated with thermally evaporated Ge(20 nm)/Au(50 nm) to facilitate the approach of the integrated tunnelling tip of the Hall sensor during magnetic imaging.

Direct electronic contact between the ferromagnet and superconductor locally suppresses the superconducting order parameter due to exchange-mediated Cooper pair breaking [1]. In order to exclude this effect, a second sample has been fabricated with a thin alumina (Al_2O_3) dielectric layer between the disk array and the Niobium film, as illustrated in Figure 4-1(b). The dielectric layer has been realised by O_2 plasma oxidation of a 1.6 nm thick sputter deposited Al film by sputtering deposition.

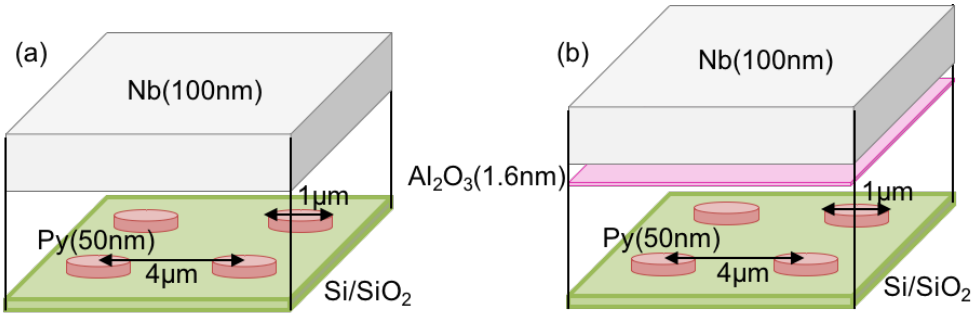

Figure 4-1: *Schematic illustration of hybrid structures including dimensions and thicknesses. (a) Nb/Py sample. (b) Nb/Al_2O_3/Py sample.*

The stray magnetic fields of the ferromagnetic Py disks and the behaviour of the superconducting vortices nucleating at $T < T_c$ (Nb) have been directly imaged with high spatial resolution and sensitivity [60] by scanning Hall probe microscopy (SHPM). After approach the sample was retracted ∼100 nm for rapid 'flying mode' scanning of the Hall sensor, thus, with the active Hall probe ∼200-300 nm above the sample during scans [56]. The non-invasive nature of the SHPM allows quantitative maps of the z-component of magnetic induction to be captured, while other imaging techniques such as low temperature magnetic force microscopy (LT-MFM) can potentially perturb the system under study by nucleating or dragging superconducting vortices [73, 74].

4.2 Results and Discussion

The superconducting critical temperature measured for the Nb film in direct contact with the ferromagnetic Py disks was $T_c = 7.10 \pm 0.05$ K, while the sample with an intermediate dielectric layer had a $T_c = 7.20 \pm 0.05$ K. These values are lower than the superconducting critical temperature for bulk Nb of 9.22 K [75] due to the low film thickness and the non-optimal conditions during the sputtering deposition. The dimensions and height of the array of ferromagnetic Py disks of the hybrid structure were confirmed by atomic force microscopy (AFM), a sample image can be seen as an inset to Figure 4-2. In order to measure the disk magnetisation as a function of the in-plane field, field was swept with the Hall sensor parked close to the centre of a Py disk at 77 K. The shallow tilt

angle of the Hall probe with respect to the sample surface allowed the in-plane component of the magnetic induction to be measured, as shown in Figure 4-2. It exhibits the characteristic form for a flux-closed magnetic vortex, showing a sign of vortex annihilation at $H_a = \pm 362\,\mathrm{Oe}$, and vortex nucleation at $H_n = \pm 190\,\mathrm{Oe}$. An SHPM image of the central region of an array at 77 K ($T \gg T_c$) in zero applied field is shown in Figure 4-3(a). Cloverleaf-like stray fields are seen in the remanent magnetisation state of the ferromagnetic Py disks. An ideal magnetic vortex would present a completely flux-closed state except for a very small core at the centre of the disk where the magnetisation turns out-of-plane. In the same image we can see three disks with reversed vorticity and inverted field contrast, the direction of the magnetisation rotation in as-fabricated samples is random. The rotation is statistically distributed between both orientations and cannot be conditioned by in-plane magnetic fields alone [71, 76]. The cloverleaf-like stray fields seen here are believed to come from a very small out-of-plane tilt of the magnetic moments due to weak uniaxial in-plane anisotropy, similar to what is observed in elliptical Py structures with in-plane shape anisotropy [29].

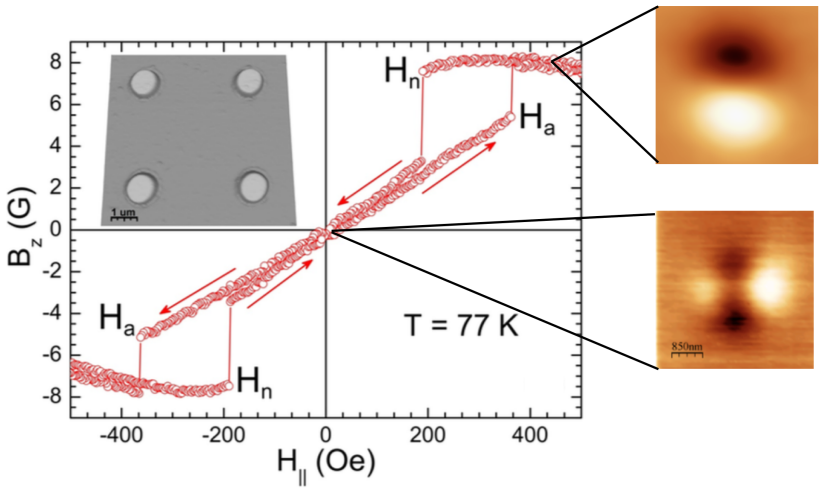

Figure 4-2: *Local magnetic induction dependence on in-plane field measured with the Hall probe in close proximity to the centre of a Py disk. The inset shows an AFM image of the 1 µm disk array. Adapted from Reference [77].*

The source of the magnetisation structure seen in the Py disks has been investigated by micromagnetic simulation using the OOMMF code [33], where

standard parameter values were used: exchange constant $A = 1.3 \times 10^{-11}\,J/m$ and saturation magnetisation $M_s = 8 \times 10^5\,A/m$. In order to approximately reproduce the spatial distribution of the perpendicular magnetic stray field measured by the Hall probe, a perpendicular component 500 nm above the centre of the disk was simulated as shown in Figures 4-3(b-e). Figure 4-3(b) illustrates the result for a simulated ideal magnetic vortex with perfect circular shape without magnetocrystalline anisotropy, when weak stray fields are only seen around the central core. Two potential additional sources have been taken into consideration for the cloverleaf-like stray fields. In Figure 4-3(c), the results for a slightly elliptical-shaped disk with semi-axes of 0.5 μm (along x) and 0.52 μm (along y) are shown. The second potential source considered is the presence of a uniaxial magnetocrystalline anisotropy along the y-axis during Py film deposition in the magnetic field from the especially compact magnetron sputtering head. We have considered two different anisotropy constants: $K_1 = 500\,J/m^3$ which is roughly the highest valued reported for Py grown by magnetron sputtering deposition [78] as shown in Figure 4-3(d), and $K_1 = 1.5 \times 10^3\,J/m^3$ which represents an extremely high value for Py, as shown in Figure 4-3(e). The simulated weakly elliptical disk exhibited a stray field intensity and profile very similar to the measured SHPM image. In contrast the simulation with a typical uniaxial anisotropy level showed much lower stray fields than observed experimentally, and only reproduces the experiment for the unrealistically large values of K_1 used in Figure 4-3(e). This indicates that the cloverleaf-like field distributions most likely arise from systematic distortions of the disks from a perfect circular shape to a slightly elliptical shape introduced inadvertently during lithography or Py sputtering deposition.

Once the samples are cooled down to $T = 5\,K$ ($< T_c$) the magnetic stray field of the ferromagnetic Py disks that threads the superconducting Nb film must satisfy fluxoid quantisation, it will either be screened or formed into quantised superconducting vortices. Similar 100 nm thick Nb thin films deposited by sputtering deposition had a reported penetration depth of $\lambda(0) = 120 \pm 10\,nm$ [79] leading to an effective Pearl penetration depth of $\Lambda = \lambda/2d \sim 140 \pm 20\,nm$ in perpendicular fields for a thin film in the limit $d \ll \lambda$ [14, 80]. Therefore, each lobe of the cloverleaf-like stray fields can be independently quantised as the disk diameter is many times larger than the estimated penetration depth.

We performed SHPM scans in small out-of-plane magnetic fields, H_z, in order

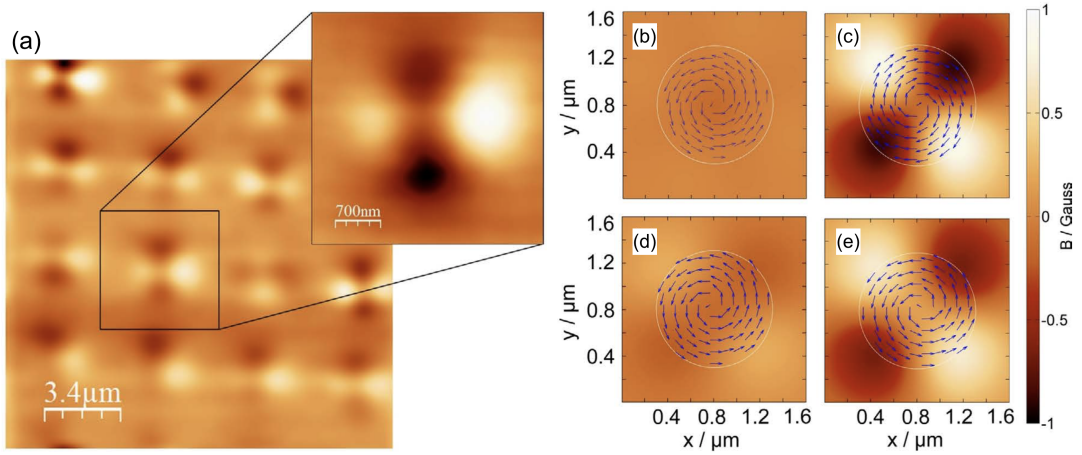

Figure 4-3: *(a) SHPM image of a central area of the array of Py disks at a temperature of 77 K with a colorscale spanning 0.8 G. OOMMF simulations of the perpendicular magnetic stray field component 500 nm above (b) a 1 µm diameter circular disk without anisotropy, (c) an elliptical disk with major axis (y-axis) of 1.04 µm and minor axis (x-axis) of 1 µm without magnetocrystalline anisotropy, (d) a 1 µm diameter circular disk with uniaxial anisotropy constant $K_1 = 500\,J/m^3$ and (e) a $K_1 = 500\,J/m^3$ diameter circular disk with uniaxial anisotropy constant $K_1 = 1.5 \times 10^3\,J/m^3$. The blue arrows illustrate the simulated magnetisation at the disk surface. Adapted from Reference [77].*

to shed further light on this matter. The relationship between the superconducting vortex nucleation position and the cloverleaf-like stray magnetic fields due to the Py disks could be determined by simultaneously imaging them. Figure 4-4 shows SHPM images of central regions of both samples. The cloverleaf-like stray fields can be clearly seen in Figures 4-4(a) and (f) obtained above T_c at 7.5 K in $H_z = 0$. All other images were acquired after field cooling to 5 K in the indicated out-of-plane field ((a-e) for the sample without dielectric layer; (f-j) for the sample with a dielectric layer). In order to indicate the centres of Py disks, white or black dotted lines have been superimposed on the scans and their intersection determines the centre of the disks.

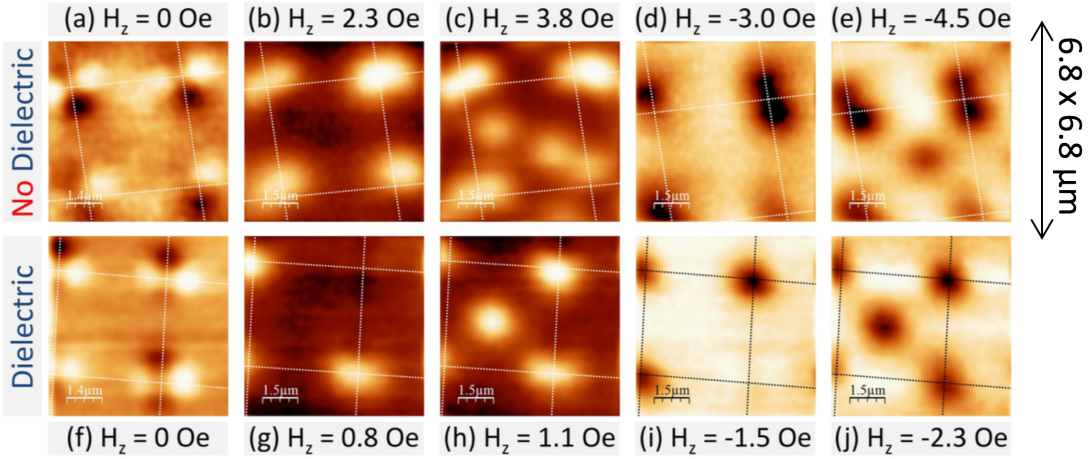

Figure 4-4: *(a-e) SHPM images of the hybrid structure without a dielectric layer (a) at $T = 7.5\,K$, and (b-e) after field cooling to 5 K in the indicated magnetic fields. (f-j) SHPM images of the hybrid structure with a dielectric layer (f) at $T = 7.5\,K$, and (g-j) after field cooling to 5 K in the indicated magnetic fields. Reproduced from Reference [77].*

A careful line profile analysis and sequential image subtraction was performed to identify vortex locations and magnitudes more precisely. In the case of an intervortex distance less than ∼500 nm, the vortices cannot be resolved due to the finite spatial resolution of the Hall probe. In such cases the number of vortices was determined by integrating the magnetic flux associated with the feature. This indicates that two vortices (antivortices) nucleate on top of both bright (dark) lobes of a ferromagnetic Py disk in the sample with the superconducting Nb

film in direct contact with the disks. In Figures 4-4(b) and (c), the large white structures with a round and slightly elongated shape contain two vortices side by side. By reversing the sign of the applied field two black antivortices can be seen on top of the black 'cloverleaf' lobes of a disk. In contrast, in the sample with an intermediate dielectric layer only one vortex (antivortex) nucleates at the centre of the disk as shown in Figures 4-4(g-j).

Upon increasing the cooling field, the pinning sites above the disks ultimately become saturated and interstitial vortices (antivortices) begin to nucleate. This can be seen in Figures 4-4(c,e) for the sample with the superconducting Nb film in direct contact with the ferromagnetic Py disks and in Figures 4-4(h,j) for the sample with a dielectric layer. In the latter case interstitial vortices nucleate at a lower magnetic field due to the in general weaker pinning potential. This can be easily seen in Figures 4-5(a,b) which plot the number of on-site (circles) and off-site (triangles) vortices for the two samples as a function of the cooling field, whereby the grey shading shows the field range where all vortices were pinned on top of the Py disks. The total number of vortices nucleated inside the scan area is represented by the black squares, and follows an approximately linear dependence on the applied magnetic field in both cases. Note that when the number of vortices drops to zero (indicated by a vertical dotted line) the curve intercepts the field axis to the left of the origin due to the additional earth's magnetic field at the sample.

Figures 4-4(e) and (j) show the samples at the highest fields where a single interstitial vortex can be seen in the middle of a unit cell, stabilised by the repulsive interactions with vortices pinned on top of the disks. By further increasing the field, more interstitial vortices nucleate and systematically arrange under their mutually repulsive interactions. Figure 4-6 shows an approximately triangular arrangement of vortices arising due to the competition between interactions with static on-site vortices and other free interstitial vortices, and which rotates as the cooling field is increased (c.f., Figures 4-6(a-d)). The rotation seems to be driven by repulsion from a new vortex that has nucleated near the edge of the unit cell.

In Figure 4-7 we show images of the sample with an intermediate dielectric layer at high positive and negative magnetic fields. Curiously, we see pairs of closely-spaced vortices composed of one interstitial and one on-site vortex. The position of the off-site vortex is modified by the nucleation/movement of nearby

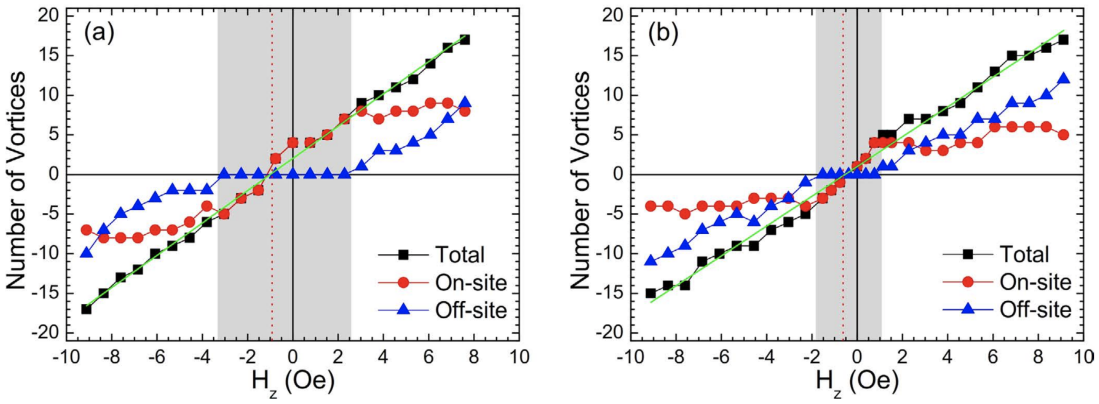

Figure 4-5: *Number of vortices nucleated in the full scan area as a function of perpendicular cooling field, (a) without and (b) with a dielectric layer. Circles and triangles indicate vortices nucleated above disks and between disks, respectively. Black squares represent the total number of vortices. The green fitted line shows an approximately linear nucleation trend. Reproduced from Reference [77].*

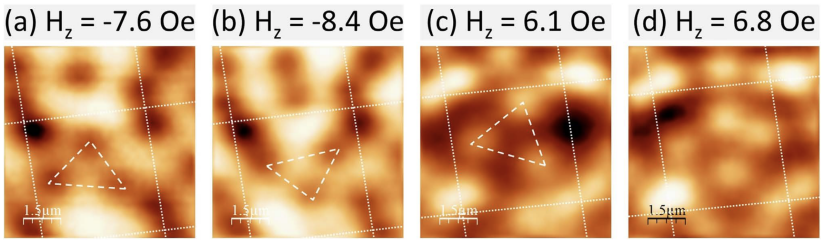

Figure 4-6: *SHPM images near the centre of a hybrid structure without a dielectric layer after field cooling to 5 K in the indicated magnetic fields, showing approximately triangular interstitial vortex (antivortex) arrangements. Reproduced from Reference [77].*

interstitials as the cooling field is increased (c.f., the pair of antivortices in the top right hand corner of Figures 4-7(a,b) and the pair of vortices at the same location of Figures 4-7(e,f)). In Figure 4-7(c) we can see that a third antivortex has joined the original pair on the upper right disk. This suggests an unexpected attractive interaction between on-site and nearby off-site vortices (antivortices). It is possible that the supercurrent trajectories have been perturbed by the topographic corrugation of the superconducting Nb film due to the underlying Py disks, partially reducing the repulsive forces between on-site and interstitial vortices. The interstitial vortices coupled to on-site vortices appears to exhibit no preferential positions around the disk. This indicate that there is no direct interaction with the magnetic stray field lobes of the Py disks.

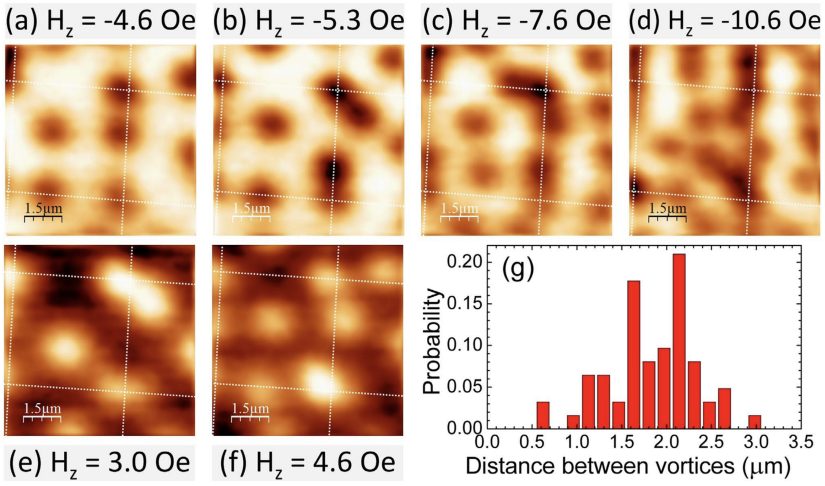

Figure 4-7: *(a-f) SHPM images of the hybrid system with a dielectric layer after field-cooling to 5 K in the indicated fields, and (g) a histogram of the nearest neighbour vortex spacing in (d). Reproduced from Reference [77].*

In strongly type II materials vortices of the same polarity experience mutual repulsion and the presence of competing attractive forces is not expected. Similar vortex pair formation was reported by Kramer *et al.* [81], however in a system of Co/Pt multilayer disks with out-of-plane magnetisation, where spontaneous vortex-antivortex pairs were expected. By Delaunay triangulation of the vortices in Figure 4-7(d) at H_z = -10.6 Oe we could establish a histogram of the nearest neighbour antivortex distances, shown in Figure 4-7(g). A bimodal distribution

seems to exist indicating the clustering of interstitial antivortices about the Py disks with more widely separated antivortices near the middle of the unit cell. Also, we can see in Figure 4-7(d) a trend for the formation of connected chains of antivortices between Py disks.

We have also applied a constant in-plane magnetic field, $H_{||} = 50\,Oe$, to the samples creating what is commonly named an 'onion' magnetic dipole state. In such a state the vortex core has not been annihilated as the Py disks are not fully saturated, and the core is probably pinned near the edge of the disk. The presence of opposite magnetic stray fields on the poles of each disk are likely to nucleate and pin vortices and antivortices. The vortex behaviour observed in both arrays was very similar, and is illustrated in Figure 4-8 for the sample with an intermediate dielectric layer. After field-cooling to 5 K the number of vortices and antivortices has been estimated by analysing line scans across them. Externally applied out-of-plane fields threading the sample must either nucleate new vortices (antivortices) or annihilate existing antivortices (vortices) in order to satisfy fluxoid quantisation, and this can break the vortex/antivortex symmetry of the poles of the Py disks.

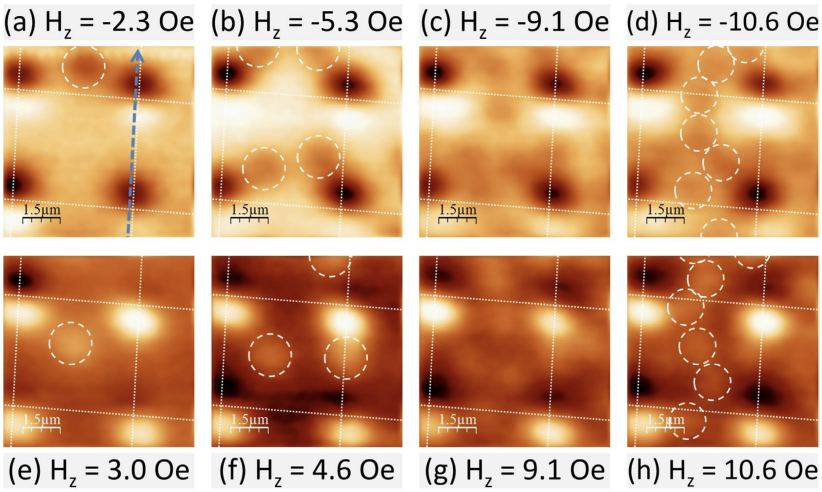

Figure 4-8: *SHPM images of the system with a dielectric layer after field-cooling to 5 K at fixed in-plane field $H_{||} = 50\,Oe$ and in the indicated out-of-plane fields. Reproduced from Reference [77].*

A very complex process of vortex nucleation or annihilation seems to take

place and the net flux linked to each Py disk does not change smoothly with out-of-plane magnetic field. In Figure 4-9 we show line scans across two adjoining disks (designated by a blue dashed line in Figure 4-8(a)) after field-cooling in negative (Figure 4-9(a)) and positive (Figure 4-9(b)) out-of-plane fields. Due to the sum of the contribution of the parasitic out-of-plane component of the electromagnet and the Earth's magnetic field an effective field of H_{eff} = -1 Oe at zero applied field has been estimated. We first see vortex annihilation for negative fields (green line; H_z = -2.3 Oe) followed by antivortex nucleation (blue line; H_z = -3.0 Oe). Then for positive fields we first see antivortex annihilation (red line; H_z = 0.4 Oe) followed by simultaneous antivortex annihilation and vortex nucleation (green line; H_z = 2.3 Oe). Note that when one on-site vortex (antivortex) is annihilated the opposite on-site antivortex(vortex) seems to widen as clearly seen in the line scan.

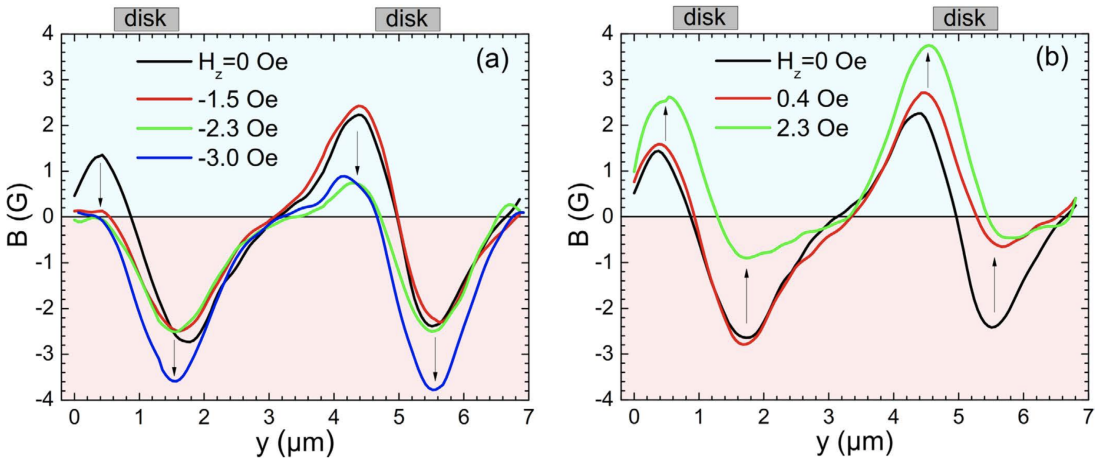

Figure 4-9: *Line scans across two adjacent Py disks in the hybrid structure with a dielectric layer in an 'onion' magnetisation state ($H_{||}$ = 50 Oe) revealing nucleation and annihilation events when an (a) negative and (b) positive out-of-plane field is applied. The dashed blue arrow on Figure 4-8(a) indicates the location and direction of the line scans. Reproduced from Reference [77].*

Interestingly the off-site vortices and antivortices in Figure 4-8 have also nucleated nearest to the poles of the same polarity, while one expects that they should be repelled from these. A zigzag-like structure can be seen between disks with increasing number of interstitial antivortices or vortices, as shown in Figures 4-

8(d) and (h), that seems to be caused by competing repulsive and attractive interactions.

Under an increasing fixed in-plane field of $H_{||} = 100\,\text{Oe}$ the system exhibits a similar vortex nucleation/annihilation behaviour, however a clear relation between interstitial and on-site vortices can now be established. A restored symmetry is observed in comparison to the broken symmetry when half of this value of in-plane magnetic field is applied. The nucleation of an interstitial antivortex linked to the annihilation of an on-site antivortex is shown in Figure 4-10(a), but is only clearly seen in the difference image (Figure 4-10(c)) where the white spot represents a new antivortex and the black spot a missing antivortex. Something similar is seen in Figures 4-10(d,f) where an on-site vortex has been annihilated and an interstitial vortex nucleated. The line scans in Figures 4-10(g,h) obtained from Figures 4-10(a,d) indicated by the dashed lines confirm the annihilation of an on-site antivortex (vortex) when the field is increased. In both Figures 4-10(g,h) we can associate the change of population by one vortex (antivortex) to a change in the peak dipole field of $\sim 1.0 \pm 0.1\,\text{G}$.

The two vortices (antivortices) observed close to each other on top of a disk suggest that there is a reasonably strong pinning potential at play, as the usual triangular Abrikosov lattice in Nb thin films [82] was not observed. Using an expression due to Pearl [27], we estimated the pinning force (F_p) necessary to balance the repulsive force (F_r) between the two vortices seen in the top right hand corner of Figure 4-4(d) which are separated by $1.0 \pm 0.1\,\mu\text{m}$. The expression accounts for the repulsive interaction between two vortices at a separation r in an infinite superconducting thin film of thickness $d \ll \lambda$,

$$F_r = \frac{\Phi_0^2}{\mu_0 \pi r^2}, \tag{4.1}$$

where Φ_0 is the superconducting quantum of flux. The repulsive force is estimated to be $F_r = 1.1 \pm 0.2\,\text{pN}$ (pinning force per unit length, $f_r = 11 \pm 2\,\text{pN}/\mu\text{m}$), approximately half the value reported by Shapoval *et al.* [83] in a similar hybrid structure.

Even though the presence of the Py disk array disturbs the expected triangular vortex ordering, it is interesting to compare the vortex spacing in the interstitial triangular vortex structures of Figure 4-6 with that expected in an Abrikosov

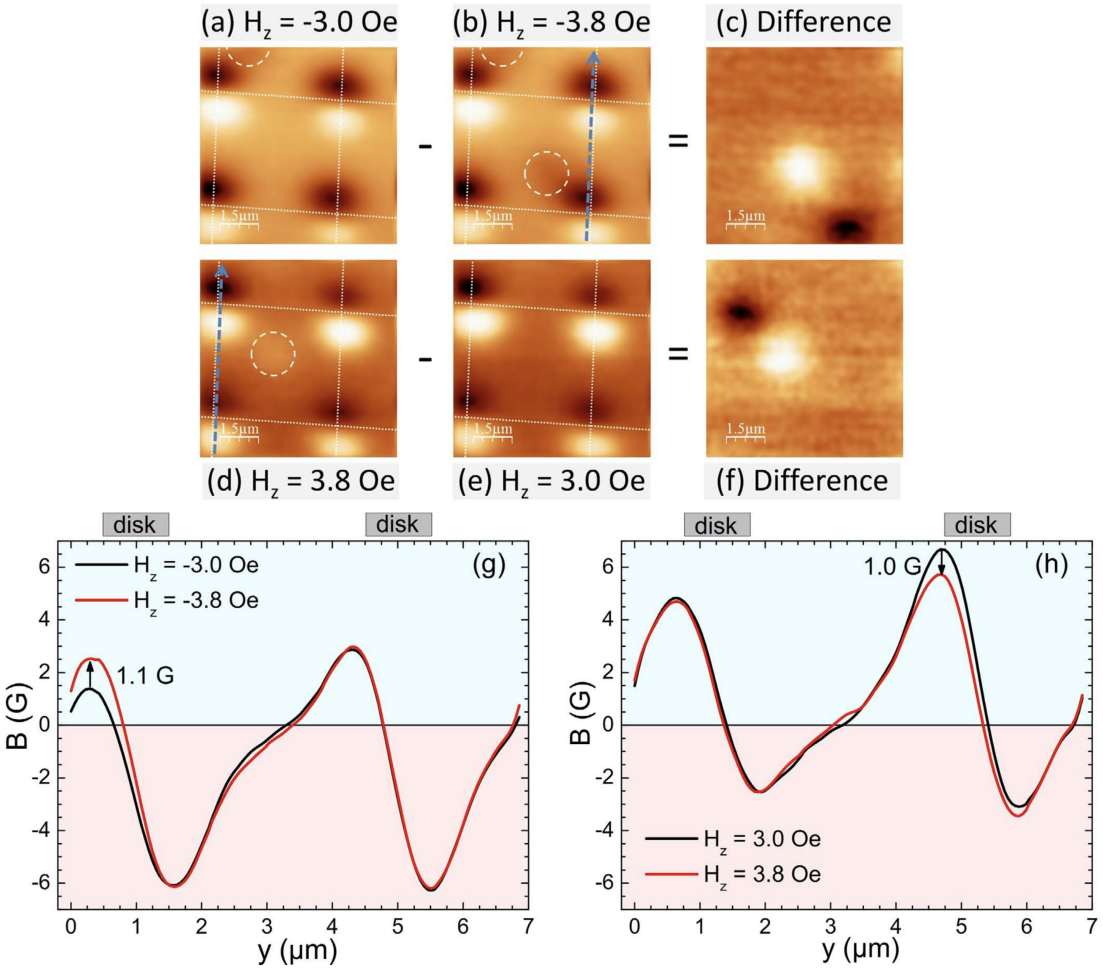

Figure 4-10: *SHPM images at fixed in-plane field $H_{||} = 100\,Oe$ after field-cooling to 5 K in out-of-plane field (a) H_z = -3.0 Oe, (b) H_z = -3.8 Oe, (c) Difference image (a)-(b), (d) H_z = 3.8 Oe, (e) H_z = 3.0 Oe, (f) Difference image (d)-(e). (g,h) Line scans across two adjacent disks indicated by the dashed blue arrows in (b,d) showing on-site antivortex annihilation in (a) and vortex annihilation in (c) respectively. Reproduced from Reference [77].*

vortex lattice:

$$a_0(\mu m) = \frac{4.89}{\sqrt{B(G)}}. \tag{4.2}$$

We have compared the estimated lattice parameter, a_0, and the average (anti)vortex spacing, a_m, for the effective magnetic field applied of -7.5 Oe and 7.0 Oe in Figures 4-6(b) and (c), respectively, where the effective field of -0.9 Oe at zero applied field was estimated from Figure 4-5(a). We obtain the values of $a_0 = 1.78\,\mu$m and $a_m = 2.26\,\mu$m for Figure 4-6(b) and $a_0 = 1.85\,\mu$m and $a_m = 2.34\,\mu$m for Figure 4-6(c). This systematic deviation shows that the interstitial vortex lattice not only depends on the applied magnetic field but also on the attractive potential experienced by on-site vortices as well. In this way the intervortex distance and orientation of the interstitial triangular arrangements are controlled by the location of the vortices on top of the disks which are in turn controlled by the magnetisation structure of the Py disks.

In the two types of samples studied the vortices and antivortices have been preferentially pinned in different positions, suggesting a qualitatively different pinning landscape. In the hybrid structure without a dielectric layer the superconducting Nb film and the ferromagnetic Py disks are electronically coupled and the nucleated vortices experience a uniform pinning potential over the whole area of the disk due to the exchange-mediated Cooper pair breaking. In addition, the cloverleaf-like stray magnetic fields of the Py disks induce further Cooper pair breaking and pinning dependent on the field polarity. Conversely, in the sample with the intermediate dielectric layer the exchange-related pinning is not present and the only pinning is due to the Py stray fields present. Therefore, the pinning potential is much shallower and only a single vortex can be pinned, possibly centred on the core of the disk.

Most theoretical studies [68, 69] consider an insulating layer between the superconducting and ferromagnetic structures, thus we are only able to compare predictions with the hybrid system with an intermediate dielectric layer. Both the cited papers employ the London theory to describe the response of a thin superconducting film with a single ferromagnet nanostructure sitting on top. The models do not consider dipole-dipole interactions with other ferromagnet nanostructures in an array, however the in-plane dipole field of our disks when in the

vortex state and saturated are estimated to be zero and $H_{sat} \sim m/a^3 \sim 6\,Oe$, respectively, where a is the distance to the nearest neighbour disk. This field is much smaller than magnetic vortex annihilation fields and represents a very weak perturbation in our experimental system. Although these papers consider smaller structures than our hybrids they seem to qualitatively describe the vortex behaviour quite well. Reference [68] calculates the vortex pinning potential as a 'rigid' magnetic core moved by an in-plane magnetic field that modifies the disk magnetisation. Despite the fact that the papers do not consider spontaneous vortex-antivortex nucleation and vortex-vortex interactions, the predicted linear increase in pinning potential by moving the magnetic vortex core with in-plane field agrees qualitatively with the increasing strength of superconducting vortex pinning as the magnetisation state moves from the vortex-like state to the onion-like one. Interestingly, a circular-shaped minimum in the pinning potential was predicted near the disk edge in the magnetic vortex state, that is possibly connected to the apparent attraction between vortices we observed at low in-plane fields (c.f., Figure 4-7), however it seems unlikely to account for similar observations at high in-plane fields. The authors of reference [69] considered a bar with fixed in-plane magnetisation and studied the pinning of a free superconducting vortex on one of the poles of the bar, depending on the magnetisation and the presence of nucleated vortex-antivortex pairs. They show that the magnetic field profile of a square-shaped and a disk-shaped ferromagnet produce qualitatively similar magnet-vortex interactions. Hence, for simplicity we have compared our experimental results with the predicted threshold magnetisation required for vortex-antivortex pair nucleation by a square-shaped magnetic nanostructure. By extrapolating the calculated data in Figure 4-9 of reference [69], our predicted M/M_0 ratio at saturation of 0.39 indicates that significantly more than two spontaneous vortex-antivortex pairs should form. We found a maximum of four vortices(antivortices) nucleated on each pole of the disk in the partially magnetised onion-like state at $H_{||} = 100\,Oe$, which qualitatively agrees with this. The field polarity-dependent pinning of vortices at $H_{||} = 50\,Oe$ shows a very complex pattern of vortex nucleation and annihilation depending on out-of-plane field. Once again, Figure 4-9 of reference [69] shows regions where free vortices are alternatively pinned at the positive or negative poles of the ferromagnet with increasing magnetisation, however this does not clarify why the vortex behaviour in

$H_{||} = 100\,Oe$ seems to become to some extent more predictable. There are other features of our experiments which lack a plausible interpretation in the light of current theoretical models, such as the pairwise attraction between on-site and interstitial vortices (antivortices) at high in-plane magnetic fields, in particular in the hybrid system with the superconducting film in direct contact with the ferromagnetic Py disks. This suggests the presence of non-trivial interactions between the superconducting and ferromagnetic components of our hybrid systems. Other studies [84, 85] have suggested the possibility of generation of spin-triplet superconductivity at superconductor-ferromagnet interfaces in vortex-like ferromagnetic structures which has stimulated further experimental studies in such hybrid structures.

4.3 Conclusions

We have investigated two hybrid superconductor-ferromagnet systems. In the first hybrid system the superconducting Nb film and the ferromagnetic Py disks are in electronic contact and vortices (antivortices) nucleate on each dark (bright) lobe of the cloverleaf-like remanent stray fields of the Py disks. In the second hybrid system there is an intermediate dielectric layer between the superconducting Nb film and the ferromagnetic Py disks, and only one vortex (antivortex) nucleates at the centre of each disk and, surprisingly, appears to show a pairwise attraction with nearby interstitial vortices (antivortices) of the same sign. The two hybrid systems exhibited different vortex pattern symmetries. In the first one the cloverleaf-like stray fields strongly perturb the interstitial vortex (antivortex) arrangements, completely disrupting the expected triangular vortex lattice for Nb films. In the second one the presence of the dielectric layer eliminates the local exchange-mediated Cooper pair breaking and pinning is considerably weaker. Magnetic dipole structures formed in the 'onion' state by fixed in-plane field nucleate vortices and antivortices on the positive and negative poles respectively exhibiting a strong field polarity-dependence. Applied out-of-plane fields lead to the nucleation of vortices (antivortices) and annihilation of antivortices (vortices) on the disk poles in a complex fashion. Once the pinning potential on the poles is saturated interstitial vortices (antivortices) start to nucleate, and surprisingly this happens near the poles of same polarity in both systems. Qualitative agree-

ment is found between our results and existing theoretical predictions, although we do find features that suggest the existence of non-trivial interactions in the vortex behaviour that go beyond them. This has stimulated further experimental studies of superconductor-ferromagnet systems aimed at a configuration where novel superconducting correlations can emerge such as odd frequency triplet superconductivity [5–7].

Chapter 5

Superconductor-Ferromagnet Josephson Junctions

5.1 Introduction

The interplay between conventional superconductivity (S) and ferromagnetism (F) in hybrid structures has revealed rich and exciting new physics in the last decade. Theoretically predicted by Bergeret *et al.* [5, 86], the presence of inhomogeneous magnetisation at the S-F interface leads to the conversion of conventional spin-singlet Cooper pairs to equal-spin triplet correlations. Due to their spin-polarised character, spin triplet supercurrents are not suppressed by the local exchange field of the ferromagnet, persisting over long distances [4]. The long-range triplet correlations are the building blocks of superconducting spintronics [6, 7] that is emerging as a promising dissipationless version of spintronics. Several experiments have confirmed the generation of long-range spin triplet correlations in the presence of different ferromagnetic structures such as, the half-metallic ferromagnet CrO_2 [2, 87], artificial multi-layered ferromagnets [3, 88], the conical ferromagnet Ho [45], and the ferromagnetic Heusler alloy Cu_2MnAl [89]. Recently, there has been growing interest in Josephson junctions with inhomogeneous magnetic barriers aimed at the active control of the long-range spin-polarised supercurrents [44, 46, 90, 91]. It has been theoretically proposed [84, 85] that a S-F hybrid structure with a ferromagnetic disk in a magnetic vortex state can generate long-range spin triplet supercurrents. The non-collinear magnetisation which

promotes the generation of spin-polarised supercurrents also plays a role in the supercurrent spatial distribution and allows a level of control over the device.

In the previous chapter scanning Hall probe microscopy has been used to study superconductor-ferromagnet hybrid arrays which exhibited rich vortex phenomena with hints of unconventional behaviour nearby the Py disks. Here, we report the electrical magnetotransport properties of a similar S-F system comprising of a conventional superconductor in direct contact with a single ferromagnetic disk forming a Josephson junction, which can potentially provide deeper insights into the proximity effect in such hybrid structures. We have fabricated Josephson junctions with a central disk-like structure that consists of a bottom layer of permalloy and a top layer of niobium, both of 50 nm thickness deposited by magnetron sputter deposition. The Josephson junction geometry has been patterned by electron beam lithography and Ar^+ beam milling. In order to create a planar S-F-S Josephson junction, focused ion beam (FIB) has been used to etch a very narrow straight trench across the structure, cutting mainly through the top Nb layer, with a single pixel line of width between 10 to 20 nm. We have investigated two FIB cut devices which were estimated to be milled to depths of 45 nm and 60 nm respectively. For the shallow FIB cut we expect that a thin Nb layer is left at the bottom of the junction, while the top Nb layer has been completely divided with the deeper FIB cut. The magnetic moments in the disk-shaped Py layer are aligned in-plane in a magnetisation vortex as a result of competing exchange, shape anisotropy and dipolar energies [28, 29]. This non-collinear magnetisation is a key element for generating spin triplet supercurrents. In addition, the small central out-of-plane component present in the magnetic vortex state, which can be displaced by in-plane magnetic fields, can potentially modify the spin-triplet supercurrent spatial distribution as the long-ranged spin-triplet correlations will be suppressed at this location [46]. The two Josephson junctions have been fabricated on a single Si substrate and measured in an ac current-biased circuit based on a lock-in amplifier.

Our aim is to demonstrate that a ferromagnetic barrier with a magnetisation vortex can potentially generate long-range spin triplet correlations with potential for the dynamic control of the supercurrent distribution in Josephson junctions. This is shown by a comparative analysis of the magnetotransport in the two distinct Josephson junctions: one with an inhomogeneous ferromagnetic barrier

and another dominated by a non-magnetic metallic weak link.

5.2 Results and Discussion

The two planar superconductor-ferromagnet Josephson junctions with single central FIB cuts 45 nm and 60 nm deep can be seen in the SEM images of Figures 5-1(a) and (b), respectively. They display a fairly circular shape with a slightly larger diameter for the shallow FIB cut Josephson junction in Figure 5-1(a). The overall physical structure is shown in Figure 5-1(c) exhibiting four Cr/Au contacts for the four-point measurements. A sketch of the measurement circuit is depicted in Figure 5-1(d).

The Josephson junction with a shallow FIB cut exhibited a higher mid-point resistive superconducting critical temperature of $7.3 \pm 0.1\,\mathrm{K}$ and lower normal resistance of $6.45\,\Omega$ in comparison to the junction with deeper FIB cut which exhibited a $T_c = 7.1 \pm 0.1\,\mathrm{K}$ and $R_n = 8.20\,\Omega$, as shown in Figure 5-2. A residual resistance of approximately $0.6\,\mathrm{m}\Omega$ is observed in both Josephson junctions that forms a shoulder during the transition to the full R = 0 superconducting state. This is believed to indicate that the junction is still in the normal state while the Nb contacts have already undergone a transition to the superconducting state [46]. The Josephson junctions reach zero resistance after a second transition at $5.9 \pm 0.1\,\mathrm{K}$ for the junction with shallow cut and at $4.8 \pm 0.1\,\mathrm{K}$ for the junction with deeper cut.

We have measured the dependence of the resistance on the perpendicular applied magnetic field at different temperatures for the two Josephson junctions, shown in Figures 5-3(a) and (b). The measurements have been performed with the samples as prepared. The peaks indicate lower critical currents while the valleys indicate higher critical currents. As the temperature is increased the overall critical current is reduced and the zero resistance state is restricted to the central valley close to zero field. In Figure 5-3(a), an offset in the origin of approximately 3.5 mT can be seen which is likely to be due to magnetic flux arising from the ferromagnetic structure threading the junction. An aperiodicity in the oscillations is observed for the Josephson junction with a deep FIB cut in Figure 5-3(b). The period of oscillation is shorter for positive applied fields than for negative fields. We believe this aperiodicity is connected to the existence of a

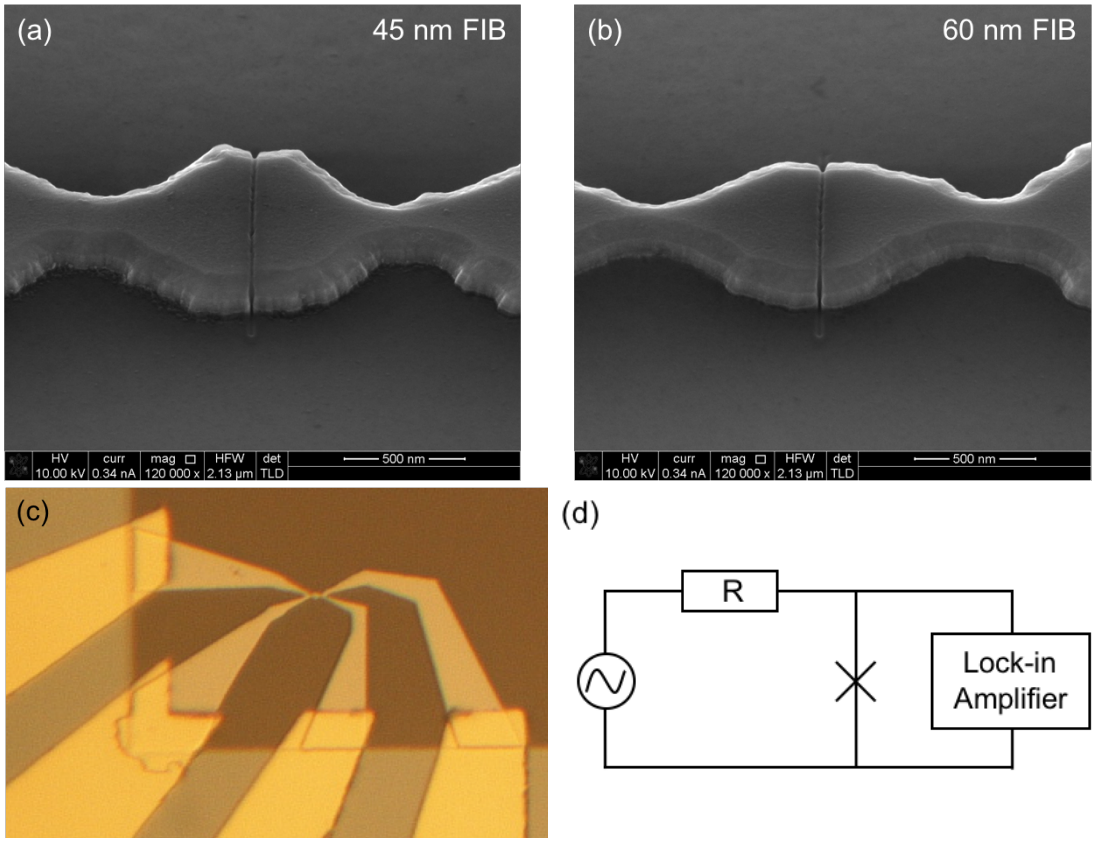

Figure 5-1: *SEM images of two planar superconductor-ferromagnet Josephson junctions with different FIB cut depths. (a) Nb/Py sample with 45 nm FIB cut depth. (b) Nb/Py sample with 60 nm FIB cut depth. (c) Optical image of the physical structure of one S-F Josephson junction showing four contacts for electrical measurements. (d) Diagram of the ac current-biased measurement circuit.*

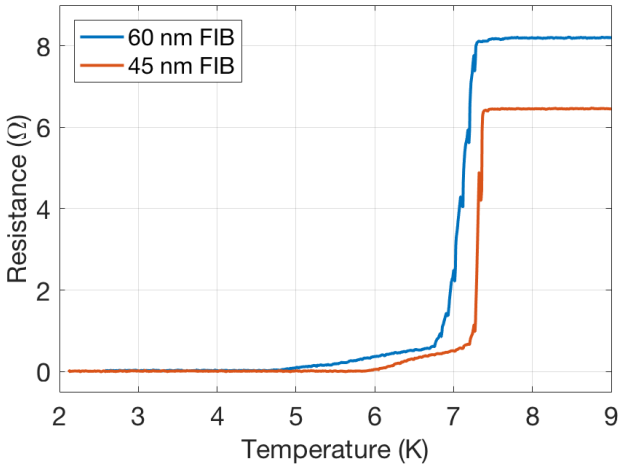

Figure 5-2: *Temperature-dependence of the resistance for two planar superconductor-ferromagnet Josephson junctions made of Nb/Py with 45 nm and 60 nm FIB cut depths. Both curves were measured with a 1 μA ac current excitation.*

non-uniform critical current density distribution across the width of the junction that is suggestive of a signature of unconventional superconducting behaviour.

Note that on average the period for the Josephson junction with deeper FIB cut (∼9.5 mT) is larger than the shallower FIB cut (∼7.8 mT). Even though both Josephson junctions were fabricated on the same piece of wafer, the Josephson junction with a shallow FIB cut displayed a slightly wider central region (larger diameter) in comparison to the Josephson junction with deep FIB cut. This can be inferred by comparing Figures 5-1(a) and (b). Consequently, a larger junction area produces shorter oscillation periods as magnetic flux threading the junction equals a quantum of flux in a smaller applied magnetic field, expressed by $\Phi = BA = BL(2\lambda + d)$, where B is the magnetic induction, A corresponds to the area of the junction, L is the junction diameter, λ is the penetration depth and d is the junction width.

Figures 5-4(a) and (b) show the dependence of the resistance on the perpendicular applied magnetic field for increasing applied ac current excitations for the shallow and deep FIB cut Josephson junctions, respectively. The larger range of currents applied to the Josephson junction in Figure 5-4(a) allows a clear visual-

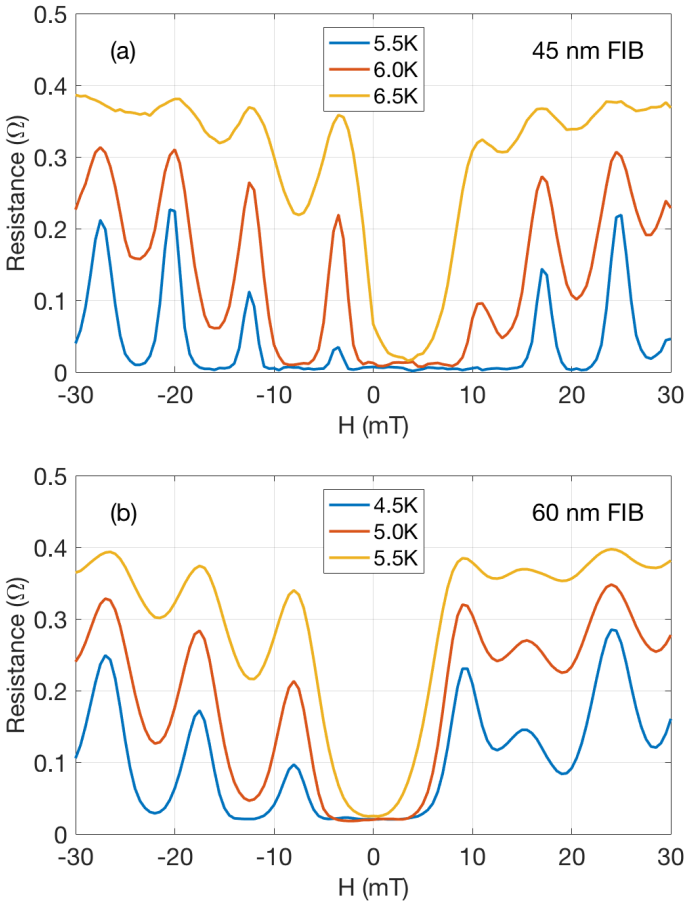

Figure 5-3: *Resistance as a function of perpendicular applied magnetic field at different temperatures for two planar superconductor-ferromagnet Josephson junctions with 45 nm and 60 nm FIB cut depths, measured with (a) 5 μA ac current excitation showing an $\sim$7.8 mT oscillation period, and (b) 2 μA ac current excitation with a $\sim$9.5 mT oscillation period.*

isation of the resistance increase with higher currents as the oscillation period is kept constant. The oscillations in Figure 5-4(b) were measured at the temperature of the resistive shoulder, and a residual resistance can be seen at the valley in zero field. Again, we see aperiodic oscillations in the Josephson junction with a deep FIB cut for different current excitations which hints at unconventional behaviour.

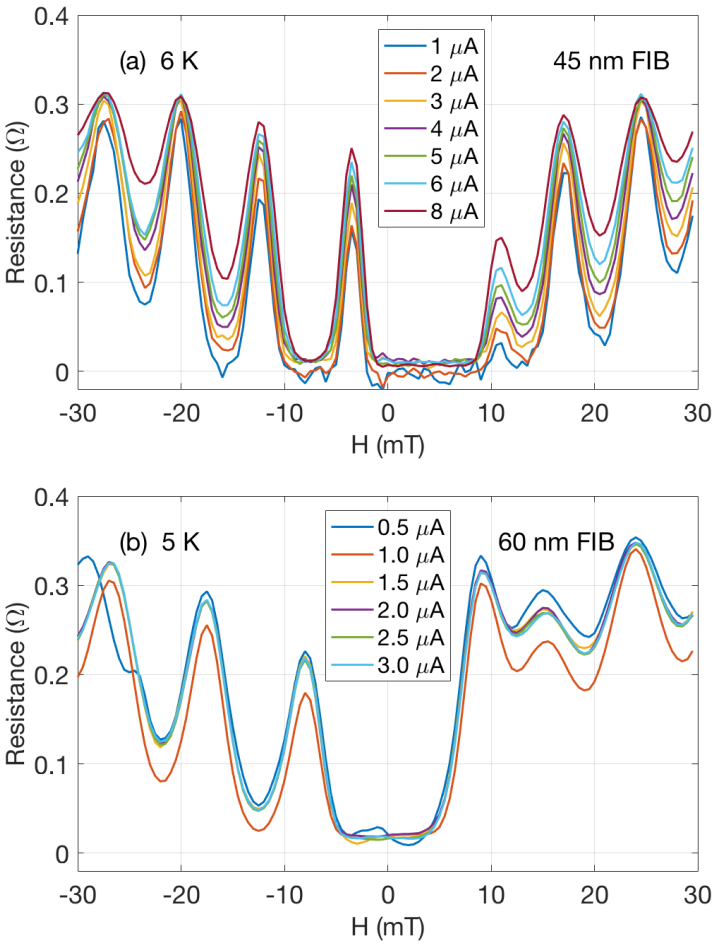

Figure 5-4: *Resistance as a function of perpendicular applied magnetic field measured with different ac current excitations for two planar superconductor-ferromagnet Josephson junctions with 45 nm and 60 nm FIB cut depths, measured at temperatures of (a) 6 K and (b) 5 K.*

Both Josephson junctions show a strong dependence on their magnetic his-

tory. In order to condition the magnetic state of the Py structure, the maximum available perpendicular magnetic field of +830 mT has been applied at 10 K and then removed. The samples were then zero-field cooled down to 5 K for measurements. The dependence of the resistance on the perpendicular applied magnetic field after the magnetic conditioning of the sample is shown in Figure 5-5 for the Josephson junction with a deep FIB cut. The shifted origin suggests that flux from the ferromagnetic layer is coupling into the junction as expected for superconductor-ferromagnet Josephson junctions [92]. Likewise, a reversed maximum magnetic field of -830 mT has been applied at 10 K and removed prior to measurement. A difference of 5.5 mT has been observed between the positive and negative magnetic conditioning and an offset of ∼3 mT from zero field state for both curves. The oscillations have acquired a different profile after magnetic conditioning. Even though a stronger degree of symmetry can be seen, the periodicity has not been fully restored, as the peak periods can differ by ≤1 mT between positive and negative fields. This suggests that the period of the oscillations is connected to the magnetisation of the ferromagnetic layer.

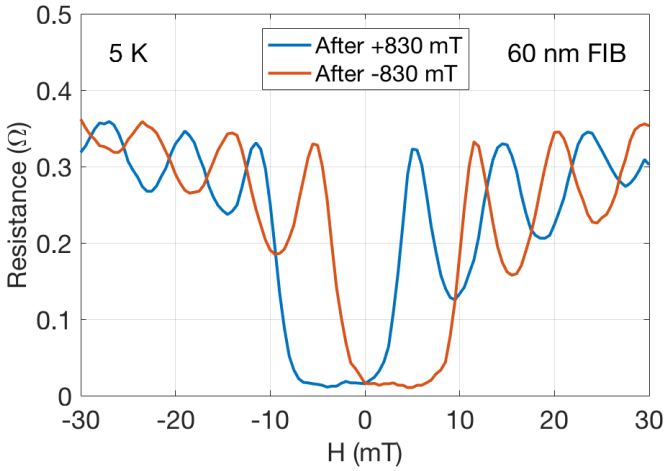

Figure 5-5: *Resistance of the 60 nm FIB cut device as a function of the perpendicular applied magnetic field after the sample has been magnetically conditioned in opposite perpendicular applied magnetic field directions. Both curves were measured with a 3 μA ac current excitation.*

Figures 5-6(a) and (b) shows the Josephson junctions' superconducting critical

current as a function of the perpendicular applied magnetic field obtained by ac I-V measurements for the two S-F Josephson junctions. The circle symbols represent the experimental data points and the solid line serves as a visual guide to the eye. Firstly, the sample magnetic state has been conditioned by applying and removing a +830 mT out-of-plane magnetic field at 10 K. Even though the applied magnetic field is quite not strong enough to saturate the Py disk magnetisation out-of-plane, we believe that it nevertheless significantly orders the remanent magnetic vortex state. A voltage threshold of 50 nV has been used to define the superconducting critical current. In addition, a maximum limit of 10 A for the I-V measurements has been imposed due to experimental limitations, which results in a flat line at the peak of the central oscillation lobes. The maximum critical current values in both Josephson junctions are shifted from zero field, probably due to the presence of internal flux and demagnetising fields from the Py barrier.

The Nb layer in the Josephson junction with a shallow FIB mill has not been fully cut through and a thin normal-Niobium metal barrier can proximitize, allowing spin singlet supercurrents to dominate the junction transport. A typical Fraunhofer-like diffraction pattern can be seen in Figure 5-6(a) with a sinusoidal current-phase relationship, which is characteristic of a uniform and constant supercurrent density distribution where the lower order minima separation is two times ($\sim$14 mT) the higher order minima separation ($\sim$7 mT). This proportion is a common feature in Josephson junctions as it characterises a single-slit interference pattern.

The Josephson junction with a deep FIB cut exhibits a distinct Fraunhofer-like pattern where the lower order minima separation ($\sim$12 mT) is not twice the value of the higher order minima separation ($\sim$8 mT), as seen in Figure 5-6(b). This suggests a possible non-uniform supercurrent distribution in the junction with the possible formation of more localised supercurrent channels [21]. Note that the minima in Figure 5-6(b) corresponds to the maxima in Figure 5-5 for applied positive field and, curiously, only the minimum at H = 0 cannot be seen as the measurements shown in Figure 5-5 used a current excitation of 3 μA.

The standard Fourier transform relation between the magnetic field-dependent critical current and the spatially-dependent critical current density [46, 93] is

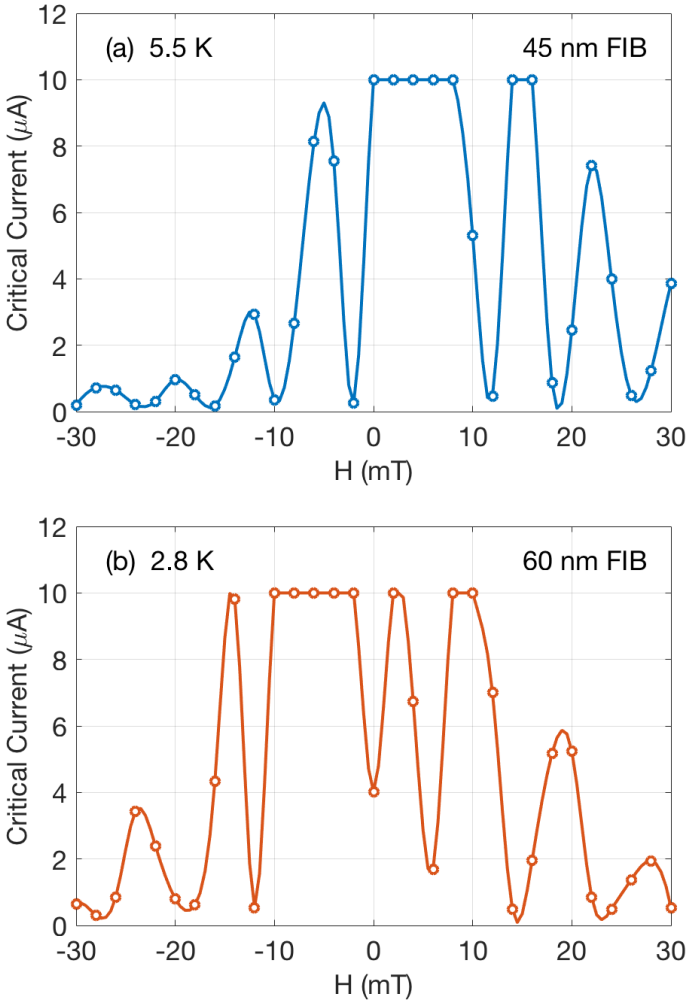

Figure 5-6: *Dependence of the critical current on perpendicular applied magnetic field for two planar S-F Josephson junctions at different temperatures. The circles represent the experimental data points and the solid line is a guide to the eye. (a) Typical Fraunhofer-like diffraction pattern characteristic of a uniform supercurrent density distribution in the Josephson junction with shallow FIB cut (non-magnetic barrier). (b) Anomalous Fraunhofer-like diffraction pattern suggesting a non-uniform supercurrent distribution in the Josephson junction with deep FIB cut (ferromagnetic barrier).*

given by

$$I_c(B_z) = \left| \int_{-L/2}^{L/2} j_c(x) e^{2\pi i(2\lambda+d)/\Phi_0} dx \right|, \tag{5.1}$$

where L is the lateral width (disk diameter), $(2\lambda + d)$ corresponds to the effective length with λ the penetration depth and d the trench width, and Φ_0 is a quantum of flux. This expression shows that the oscillations must always be symmetric for positive and negative magnetic fields, $I_c(B_z) = I_c(-B_z)$. This anomalous Fraunhofer pattern in which local minima in the critical current are nonzero and non-periodic with external field is quite striking and hints at unconventional superconducting behaviour in the Josephson junction with a non-collinear ferromagnetic barrier.

However, the presence of stray fields in the junction can potentially modify the periodicity of the critical current minima leading to an underestimate of the critical current values [93]. Hence, we have performed micromagnetic simulations using OOMMF in order to understand the magnetic state of the Py structure when the 30 mT perpendicular magnetic field excursion is applied. Two geometries have been considered, a circular 1 μm diameter Py disk and a slightly elliptical Py disk with major axis of 1.04 μm, similar to that studied in a previous chapter. The simulations have shown that the magnetisation structure is relaxing in the applied magnetic field for both geometries in a similar fashion. Figures 5-7(a) and (e) show the magnetisation on the surface of the circular disk and the elliptical disk in zero field, respectively. Upon applying a 30 mT perpendicular field, an increase in the out-of-plane magnetisation can be seen in Figures 5-7(b) and (f). The stray fields for this magnetic configuration can be seen in Figures 5-7(d) and (h), 50 nm above the circular and elliptical disks, respectively. Even though the magnetisation changes and additional stray fields might enter the junction with the applied perpendicular field, the extent to which they might modify the spatial distribution of critical current is not clear, as the Josephson junction with a shallow cut also experiences these magnetisation changes but exhibited a conventional behaviour.

Nevertheless, the fact that we have measured supercurrents through a relatively wide ferromagnetic channel (trench width of 10-20 nm) strongly suggests the presence of triplet pairing. The spin singlet supercurrents decay on the scale length of $\xi_F = \sqrt{\hbar D_F / E_{ex}}$, where D_F is the electron diffusion constant and E_{ex} is

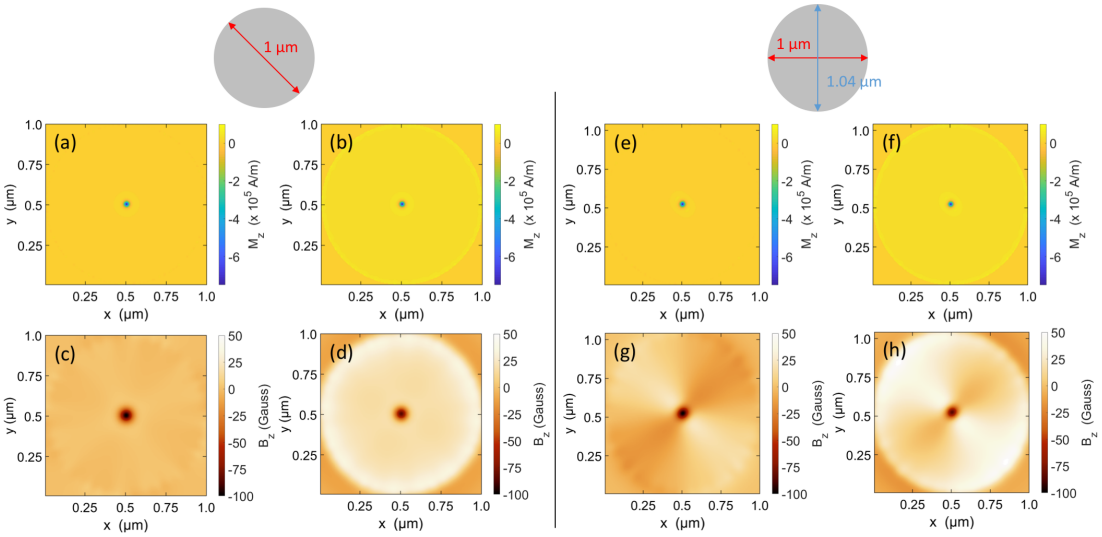

Figure 5-7: *OOMMF simulations of the magnetic state of (a-d) a 1 µm diameter Py disk and (e-h) a slightly elliptical Py disk with major axis of 1.04 µm along the y-axis. Magnetisation of a circular Py disk in (a) zero field and (b) in 30 mT out-of-plane field. Magnetic stray fields at 50 nm above the circular Py disk (c) in zero field and (d) in 30 mT out-of-plane field. Magnetisation of an elliptical Py disk in (e) zero field and (f) in 30 mT out-of-plane field. Magnetic stray fields at 50 nm above the elliptical Py disk (g) in zero field and (h) in 30 mT out-of-plane field.*

the exchange energy in the ferromagnet. For permalloy, the coherence length has been estimated to be of $\xi_F = 1.4\,\mathrm{nm}$ [94], which is considerably shorter than the etched trench. Thus, we believe that the supercurrent in the deep cut Josephson junction must be composed of a mixture of spin singlet and equal-spin triplet correlations.

Although further measurements are needed in order to verify the generation of spin triplet supercurrents in the Josephson junction with a deep FIB cut and also the role of the Py magnetic stray fields in the device, we have shown strong evidence of the anomalous magnetotransport properties of such S-F hybrid structures.

5.3 Conclusions

We have fabricated and studied planar superconductor-ferromagnet Josephson junctions with a disk-like structure. A comparison of two junctions with distinct FIB cut depths has revealed very different magnetotransport properties. In both Josephson junctions shifts in the dependence of the resistance and critical current on the external magnetic field have been observed and are believed to be caused by self-fields from the ferromagnetic layer. The Josephson junction with a shallow FIB cut exhibits the expected conventional superconducting behaviour, suggesting the presence of a thin non-magnetic normal Nb junction that allows spin-singlet correlations to dominate the transport. In contrast the Josephson junction with a deep FIB cut appears to possess a ferromagnetic junction and shows signs of unconventional superconducting behaviour. The disk geometry promotes a magnetisation vortex in the ferromagnetic layer, in which the non-collinear magnetisation is critical for the generation of spin polarised supercurrents. These are believed to distribute non-uniformly in such structures creating distinct interference patterns as a function of perpendicular magnetic field. We have observed aperiodic oscillations in resistance and nonzero minima in the critical current which suggest the presence of unconventional superconductivity. OOMMF simulations have indicated a magnetisation relaxation of the Py structure in the perpendicular applied fields, which can also potentially modify the spatial distribution of the critical current in the junction. The extent to which the deep cut junction's critical current is influenced by the changing magnetisa-

tion and stray fields has still to be determined. Therefore, further experiments are needed to determine the origin of such signatures, in order to conclusively confirm the presence of spin triplet supercurrents.

Chapter 6

The Critical State in a Second Generation High-Temperature Superconducting Tape

6.1 Introduction

High temperature superconductors have been under intensive investigation since their discovery in 1986 due to their great fundamental and technological potential. $YBa_2Cu_3O_{7-\delta}$-based coated conductors have especially strong prospects in various commercial applications, such as electrical power transmission lines [95], fault current limiters [96], and rotating machines such as motors and generators [97]. Despite great developments in this area, preventing the fast decay of the superconducting critical current density in modest magnetic fields continues to be a major challenge. Dissipation takes place when an applied current drives superconducting vortices into motion. The systematic control of the superconducting vortices requires a tailored energy landscape only possible with the presence of effective pinning sites which can lead to a dissipation-free state.

A number of types of pinning sites have been explored in $YBa_2Cu_3O_{7-\delta}$ (YBCO) thin films, which includes chemical modification by ion irradiation [98], rare earth nanoprecipitates [99], and irregular artificial arrays [100], which have all been shown to actively enhance the superconducting critical current. However, the mechanism of vortex pinning has not yet been fully understood and

controlled. A better understanding of the energy landscape imposed by pinning sites and the vortex behaviour within it will allow the production of higher performance coated conductors showing higher superconducting critical current densities, which can potentially lower production costs by reducing the quantity of superconducting material and dimensions required, allowing more widespread implementation [101].

Nowadays second-generation high temperature superconducting (2G-HTS) tapes are usually doped with rare-earth ions in order to create second phase nanoparticles during the metalorganic deposition (MOD) process. In addition, other types of pinning sites also play a role in enhancing the vortex pinning such as grain boundaries, vacancies (pores), stacking faults, twin boundaries and point defects. Transport and magnetisation measurements have been most commonly used to characterise 2G-HTS tapes, which mainly probe the global macroscopic properties of superconducting vortices and pinning sites. Scanning Hall probe microscopy (SHPM) has previously been used to investigate the supercurrent flow through artificial grain boundaries [102] and to probe ac losses [103] in YBCO films over large scan areas. We have used scanning Hall probe microscopy to study the local properties of the flux front penetration at the microscopic scale, enabling us to resolve inhomogeneous supercurrent flow and deviations from classical critical state flux distributions down to a lengthscale of $\sim$1 μm.

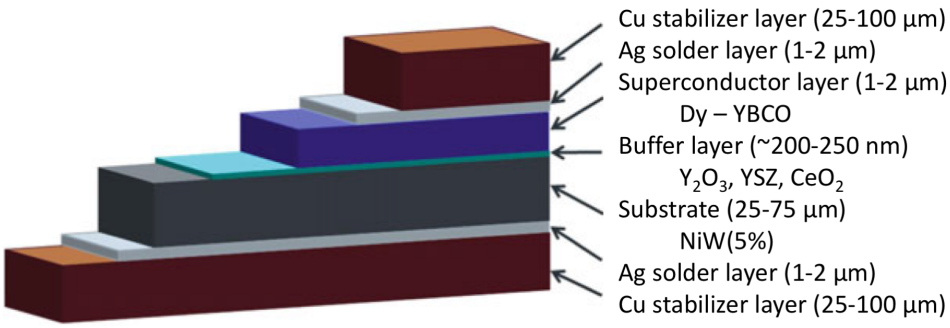

Figure 6-1: *2G-HTS architecture with layers and usual thicknesses described. Adapted from Reference [104].*

We have studied a section of 12 mm wide commercial second-generation high temperature superconducting Amperium tape from the company American Su-

perconductor, AMSC. Currently, 2G-HTS tapes are manufactured and distributed by around 10 commercial companies over the world, with American Superconductors (AMSC) and Superpower the main manufacturers [104]. This tape was manufactured using Rolling Assisted Biaxially Textured Substrate (RABiTS) technology which is based on creating a textured metallic substrate by means of rolling deformation and re-crystallization techniques, coated with a series of epitaxial oxide layers, Y_2O_3/YSZ/CeO_2, that reproduce the substrate texture and impede diffusion between the metallic substrate and superconductor film. The tape architecture and layers are schematically illustrated in Figure 6-1. YBCO materials have a perovskite-type crystal structure, illustrated in Figure 6-2, and superconductivity is believed to reside in the CuO_2 planes while the CuO chains work as charge reservoirs. This highly anisotropic material exhibit larger supercurrents in the a-b plane than along the c-axis. It has been shown by Dimos *et al.* [105] that disruptions in the lattice periodicity, such as high angle grain boundaries, can drastically restrict the supercurrent flow from grain to grain. Hence, the substrate texture is crucial in promoting the YBCO-based high temperature superconductor growth with low grain boundary misorientation enabling high superconducting critical current densities. In addition, the tape is doped with Dy_2O_3 nanoparticles which enhance vortex pinning, allowing the flow of larger supercurrents. The first-generation high temperature superconducting (1G-HTS) tape was based on BiSrCaCuO materials which are uniaxially textured (c-axis grains) through thermo-mechanical processing using powder-in-tube methods [104, 106].

The copper stabiliser layers have first been removed by wet chemical etching in ferric chloride in order to obtain direct access to the $YBa_2Cu_3O_{7-\delta}$ film. The layer of Ag solder left on top of the YBCO thin film has been carefully thinned by polishing with fine alumina paste until the superconducting layer just started to be exposed in a few isolated places. We have used scanning Hall probe microscopy (SHPM) to directly image the magnetic field component perpendicular to the surface of a $10 \times 14\,\mathrm{mm}^2$ piece of 2G-HTS tape at different temperatures. Note that this sample was narrower than the original tape due to the removal of the 1 mm solder fillets at the edges. A Hall probe with $\sim 0.8\,\mu$m spatial resolution and $\sim 5\,\mathrm{mG}/\sqrt{Hz}$ minimum detectable field was used, approached approximately 1 mm from one of the long edges of the sample and then retracted $\sim 1\,\mu$m for fast data collection. We have used two operation modes; a rapid "flying mode" where

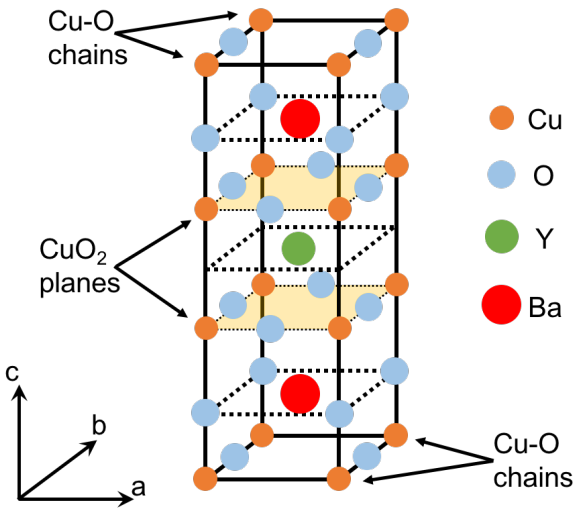

Figure 6-2: *YBaCuO perovskite-type crystalline unit cell with CuO_2 planes and CuO chains indicated.*

the Hall sensor acquires a 2D image of the maximum scan area, and a 'local' magnetometry mode whereby the sensor is parked above a chosen point and the 'local' magnetic induction acquired while sweeping an external magnetic field perpendicular to the plane of the tape. We have systematically acquired SHPM images at regularly spaced points on a magnetic field cycle starting from the zero field-cooled state. This allowed us to create a spatial map of the critical state established around a hysteresis loop.

6.2 Results and Discussion

The mid-point resistive superconducting critical temperature for the 2G-HTS tape before sample preparation was found to be $T_c = 92.0 \pm 0.2\,K$. A slightly lower value of $T_c = 89.5 \pm 0.2\,K$ was measured after being etched and polished to expose the YBCO film, shown in Figure 6-3(a). We have measured local magnetisation curves at different fixed temperatures which can be seen in Figure 6-3(b). The data have been fitted to a classical thin film critical state model developed by Brandt and Indenbom [107] represented by the solid red lines. Each closed loop was scaled by the theoretically estimated value of the critical magnetic field (H_c) which is directly proportional to the critical current density (j_c) at each tem-

perature. In Figure 6-3(c) we have plotted the critical current densities obtained from the model fitting at different temperatures, which are in good agreement with other reported temperature-dependent critical currents for this tape [108].

The data acquired on the critical state in the sample of 2G-HTS tape have been analysed using a critical state model due to Brandt and Indenbom for an infinite superconducting strip [107]. The model describes the magnetic field penetration profile (B_z) in a thin type II superconducting strip of thickness d and width $2a$ in a constant perpendicular magnetic field (H_a) in the limit $d \ll a$. Although the model makes some assumptions such as a homogeneous distribution of pinning sites with a B_z independent critical current, it has the benefit of being analytic and only having one fit parameter, the critical current density j_c.

$$B_z(y) = \begin{cases} 0 & |y| < b \\ B_c \tan^{-1} \dfrac{\sqrt{y^2 - b^2}}{c|y|} & b < |y| < a \\ B_c \tan^{-1} \dfrac{c|y|}{\sqrt{y^2 - b^2}} & |y| > a \end{cases} \tag{6.1}$$

Here, $B_c = \mu_0 j_c d/\pi$, $b = a/\cosh(\mu_0 H_a/B_c)$ describes the boundary of the central flux free region, and $c = \tanh(\mu_0 H_a/B_c)$. In Figure 6-4(a), we show a schematic diagram of the 2G-HTS tape sample where d represents the YBCO film thickness and the blue square illustrates the location of the SHPM scan area (not to scale). Note that the superconducting strip is not infinite as considered in the model but only has an aspect ratio of 1.4, however equation 6.1 is expected to describe the flux penetration profile rather accurately near the middle of the long edges. Figure 6-4(b) shows the magnetic field profile predicted by equation 6.1 across the 10 mm wide tape for different applied magnetic field intensities from the virgin state in zero field.

Since a reversion of the applied field sweep direction occurs during magnetometry measurements when it reaches the maximum field ($\pm H_{max}$), the following relationship for B_z derived in [107] is also used when the field is decreased from H_{max}

$$B_z^{\downarrow}(y, H_a, J_c) = B_z(y, H_{max}, j_c) - B_z(y, H_{max} - H_a, 2j_c). \tag{6.2}$$

The penetrated magnetic field profile across the 10 mm wide tape described by equations 6.1 and 6.2 when the applied field is reduced from a maximum field

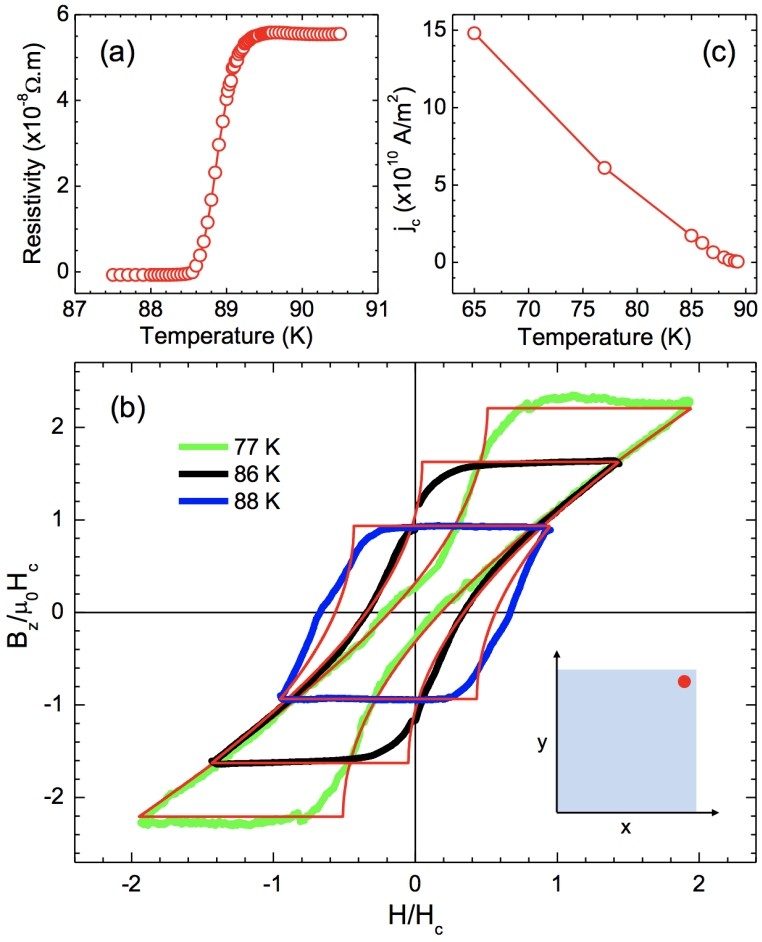

Figure 6-3: *(a) Resistive superconducting transition for the 2G-HTS tape after sample preparation. (b) Scaled magnetic induction hysteresis loops at different temperatures and fits to the critical state model (red lines). (77 K ($H_c = 24.4$ mT), 86 K ($H_c = 5.0$ mT), 88 K ($H_c = 1.2$ mT).) Inset: Illustration of the SHPM scan area with the position chosen for the local magnetometry measurements indicated as a red dot. (c) Temperature-dependence of the superconducting critical current density estimated from fits of the hysteresis loops to the model. Reproduced from Reference [109].*

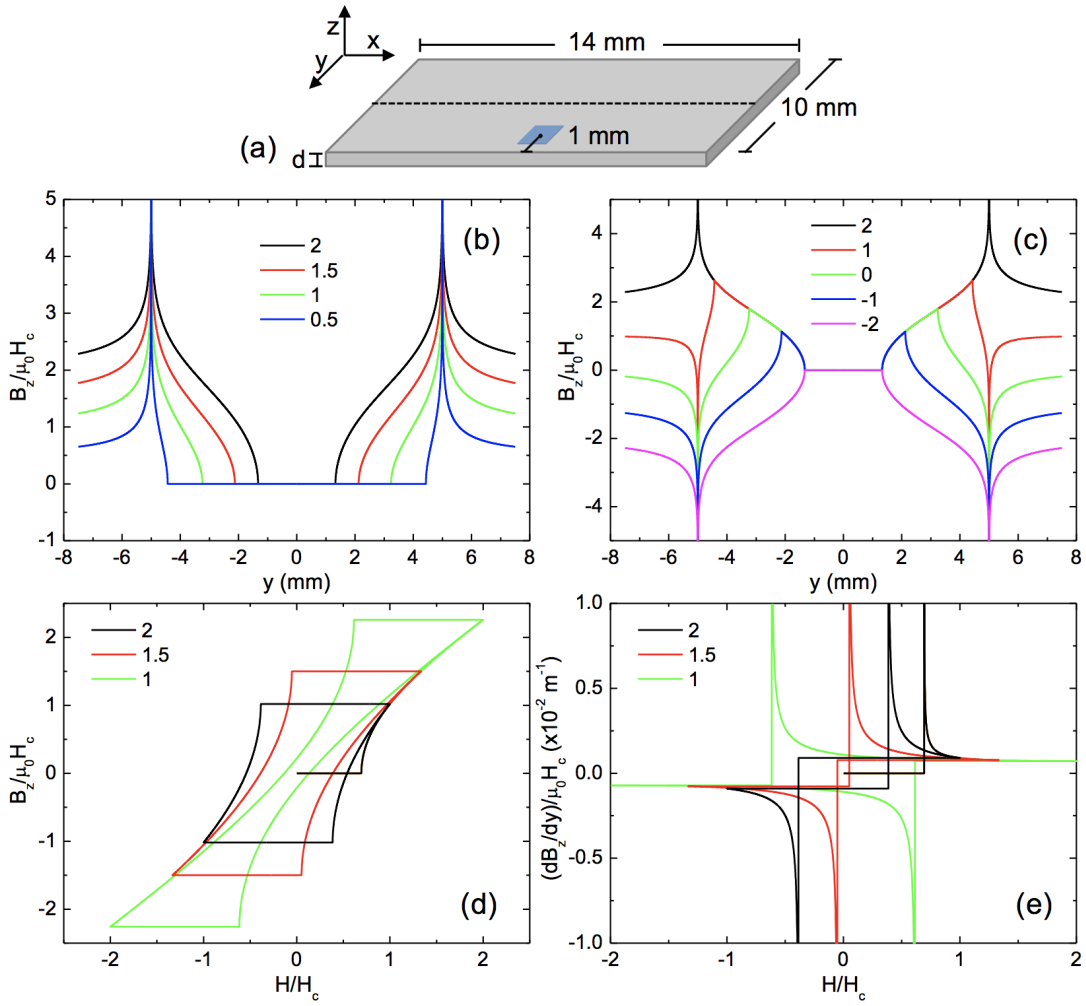

Figure 6-4: *(a) Illustration of the 2G-HTS tape sample with the SHPM field of view indicated by a blue square (not to scale). (b) Theoretical profiles of the magnetic field penetration across a 10 mm wide thin superconducting strip in perpendicular magnetic fields of H/H_c = 0.5, 1, 1.5 and 2 starting from the H/H_c = 0 zero field-cooled virgin state. (c) Theoretical profiles of the magnetic flux penetration across the superconducting strip when the applied perpendicular magnetic field is reduced from H/H_c = 2 down to 1, 0, -1 and -2. (d) Scaled magnetic induction hysteresis loops at a point 1 mm from the edge of the strip for a maximum applied magnetic field excursion of $\pm 2H_{c0}$ for critical current densities of j_c/j_{c0} = 1, 1.5 and 2, where $H_{c0} = H_c(j_{c0})$ with $j_{c0} = 5 \times 10^{10}$ A/m^2. (e) Scaled magnetic induction gradient at a point 1 mm from the edge of the strip for a maximum magnetic field excursion of $\pm 2H_{c0}$ for critical current densities of j_c/j_{c0} = 1, 1.5 and 2. Reproduced from Reference [109].*

of $2H_c$ ($H_c = j_c d/\pi$) is shown in Figure 6-4(c). Conversely, the model can be used to describe the magnetic field penetration profile at a specific point on the tape as a function of the applied magnetic field, as shown in Figure 6-4(d) at a point 1 mm from the long tape edge for different critical current densities and a maximum applied field intensity of $\pm 2H_{c0}$. Starting from zero field, the magnetic flux front penetrates at exactly the same reduced field value for all lines, and the line in black that represents $j_c/j_{c0} = 2$ lies on top of, and fully overlays, all the other lines in this section. In addition, the lateral gradient of the penetrated magnetic field across the width of the tape is given by

$$\frac{dB_z}{dy} = \begin{cases} 0 & |y| < b \\ B_c \dfrac{a^2 c}{(a^2 - y^2)\sqrt{y^2 - b^2}} & b < |y| < a \end{cases} \tag{6.3}$$

The gradient of the penetrated profile is depicted in Figure 6-4(e) and we can clearly identify the position of the flux front by the point where the gradient is singular (at y = b). Note that here again the black line that corresponds to $j_c/j_{c0} = 2$ lies on top of, and fully overlays, the other lines starting from the virgin state up to the first flux front penetration. An apparent wider initial segment can be noticed due to the overlay. This feature shows an essential difference to the Bean critical state [16] in bulk superconductors where the critical current density (j_c) is predicted to be constant and proportional to the gradient of magnetic induction. The unphysical singular behaviour predicted by the model would, in reality, be truncated by the Ginzburg-Landau depairing current density. However, this would not significantly affect Figure 6-4(e), since this is estimated to be almost three orders of magnitude larger than the measured critical current density at our study temperatures [110].

Selected SHPM images are shown in Figure 6-5 illustrating the course of flux front penetration as the applied magnetic field is increased at temperatures 83 K and 77 K. We can see from left to right the first penetration of the flux front starting from the tape's virgin state after being zero field cooled. The flux front is determined by the boundary between the mixed state and the central flux-free region whose structure has been found to be insensitive to edge topology [111]. Even though our SHPM is able to image deep sub-micron features [56], the 1 μm retraction of the Hall sensor necessary here restricted the overall spatial resolution

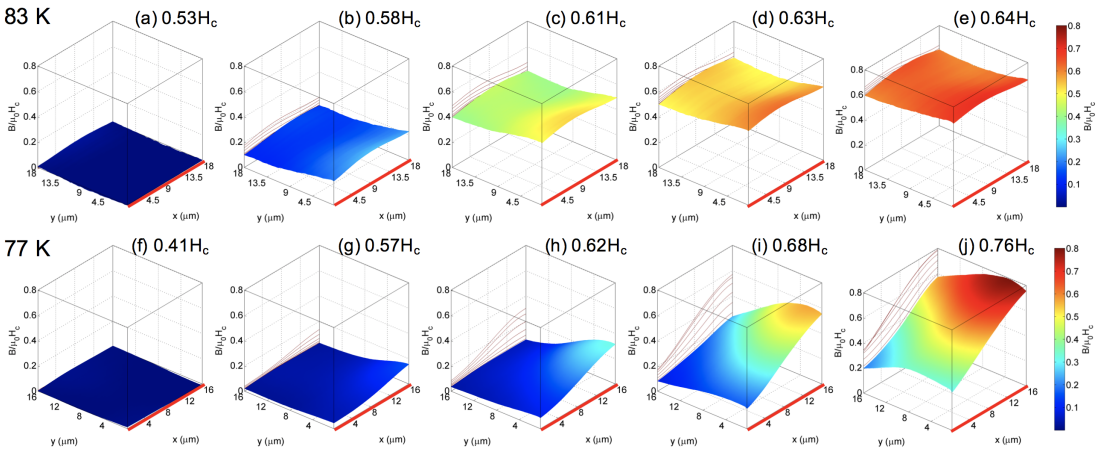

Figure 6-5: *3D SHPM images of the magnetic flux front penetration from the long side of the 2G-HTS tape (indicated by the red line) at (a)-(e) 83 K (H_c = 7.2 mT) and (f)-(j) 77 K (H_c = 24.4 mT). Reproduced from Reference [109].*

to the point where single vortex imaging is no longer possible and only bundles of vortices could be visualised. The penetrating magnetic flux front showed very distinct profiles at different temperatures. In Figures 6-5(a)-(e), we can see that the magnetic flux front penetrated fairly uniformly throughout the whole field of view at 83 K. In stark contrast we can see in Figures 6-5(f)-(j) a much more localised penetration at 77 K when the flux front penetrates mainly on the right hand side of the SHPM scan area. Together with the pinning force, the magnetic field penetration depth (λ) determines the range of interaction between vortices and plays an important role in defining the size of the vortex bundles [112]. The penetration depth depends on temperature and reduces at lower temperatures [113, 114], decreasing the screening current overlap between vortices and, together with the increasing vortex pinning force, makes vortex bundles more localised. This is displayed in the roughening of the magnetic flux front in the tape whose magnetic field dependence has been attributed to the nonlinear diffusion coming from thermally-activated vortex hopping [111].

From a full sequence of SHPM images we have calculated a map of the critical current density (j_c), as shown in Figure 6-6 at 83 K, whereby the magnetic induction at every pixel in the image has been analysed as a function of applied magnetic field using the critical state model of equations 6.1 and 6.2. We

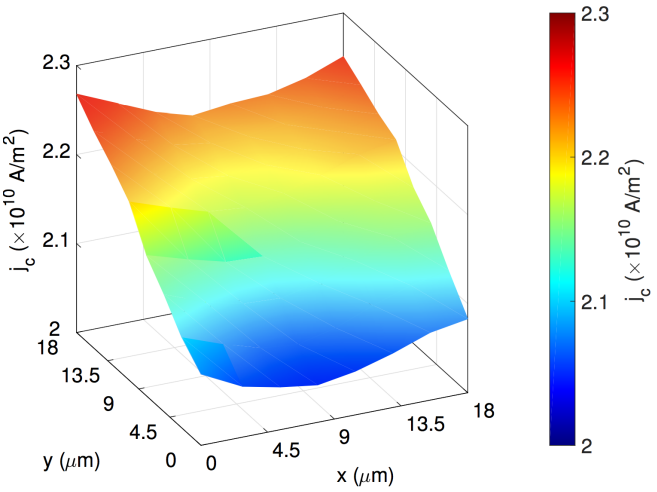

Figure 6-6: *Calculated critical current density (j_c) acquired from fitting the magnetic induction at each pixel of the SHPM image as a function of applied field to a critical state model at 83 K, for a maximum magnetic field range of ±4.8 mT. Reproduced from Reference [109].*

have used the known location of the Hall sensor to define the value of y in the model fit. Due to the rather long time that elapses between sequential SHPM images, substantial magnetic relaxation takes place due to thermally activated vortex motion (flux creep). This produces a significant reduction of the overall magnetisation [115], and estimates of j_c that are slightly smaller than those of Figure 6-3(c) which comes from the analysis of much faster magnetometry measurements. The local values of j_c estimated this way exhibit a significant variation of approximately ±7% across the entire scan area.

Substantial broadening of the penetrating magnetic flux front has been observed at low temperatures. Line scans along the y-axis of the SHPM images (across the width of the tape) are shown in Figures 6-7(a) and (b) for increasing applied fields starting from the virgin state after zero field-cooling at 83 K and 77 K respectively. We can clearly see the initial flux front penetration in both figures when the magnetic induction increases abruptly from $B_z \sim 0$. From the data we can see that the flux seems to penetrate over a narrower reduced field range at 83 K in comparison to the much more broadened increase at 77 K. At the same time, just after initial penetration the normalised gradient dB_z/dy is

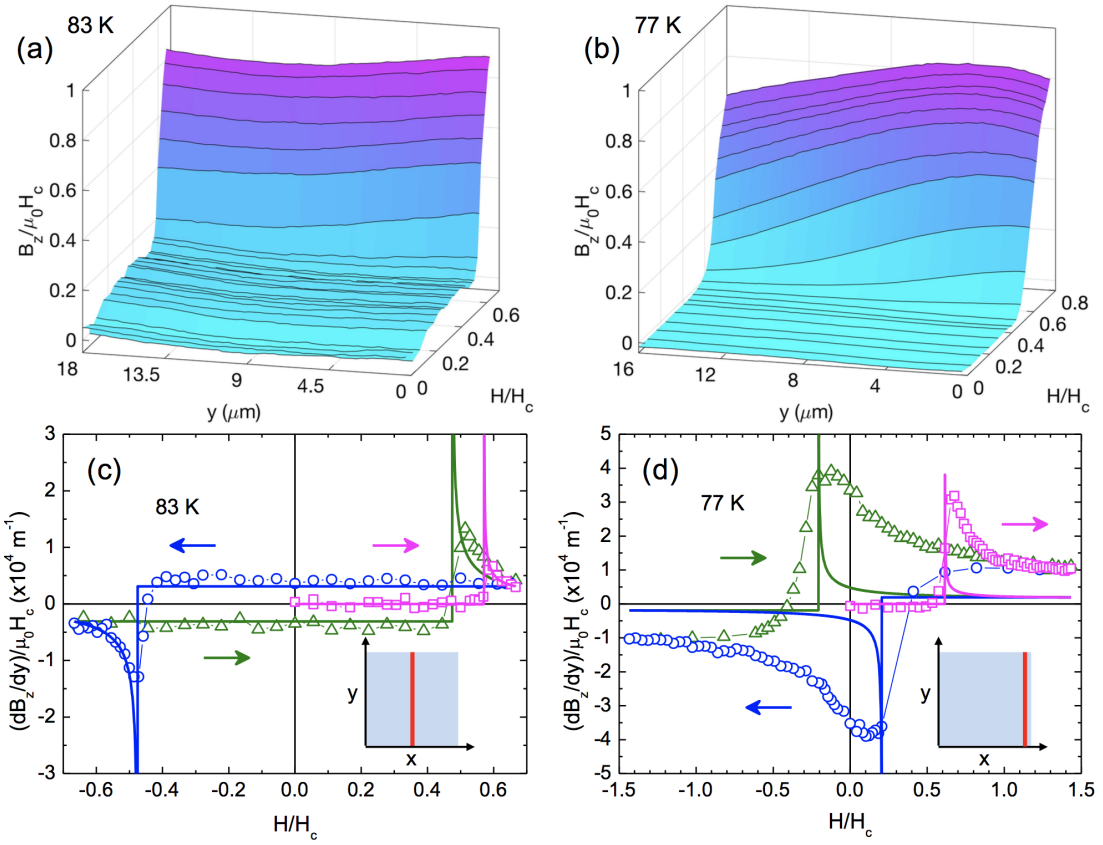

Figure 6-7: *Line scans along the y-axis of SHPM images as a function of applied magnetic field showing initial magnetic flux penetration at (a) 83 K (H_c = 7.2 mT) and (b) 77 K (H_c = 24.4 mT). Normalised gradient of the penetrating magnetic flux front, dB_z/dy, along the y-axis of SHPM images as a function of applied magnetic field at (c) 83 K and (d) 77 K. The symbols indicate the experimental data while the solid lines show the theoretical results obtained from equation 6.3. Insets: illustration of the SHPM field of view indicating the lines where the magnetic induction in (a) and (b) and gradients in (c) and (d) have been measured corresponding to the centres of penetrating vortex-bundles (red lines). Reproduced from Reference [109].*

clearly quite a lot steeper at 77 K. This point is reinforced in Figures 6-7(c) and (d) where we have plotted the gradient along half of the y-axis (9-18 μm and 8-16 μm respectively) as a function of applied magnetic field at each temperature. The square symbols and magenta line indicate the penetration of the first magnetic flux front starting from the zero field cooled virgin state. The circle symbols and a blue line correspond to the reversed flux front penetration. The effect of reversing the applied field once again is shown by the triangle symbols and dark green line. The data at 83 K closely match the expected theoretical behaviour but the singularity at initial penetration has been smeared out considerably. In contrast, at 77 K the behaviour differs considerably from the expected theoretical behaviour. The measured values of dB_z/dy are in general much larger than predicted and the singular penetration peak is broadened out over a wide range of applied fields.

A pronounced onset of local vortex-bundle formation at 77 K is seen in Figure 6-7. Considering that the supercurrents circulating around vortex-bundles lead to higher local magnetic fields than along straight flux fronts, we correlate this with the higher local dB_z/dy and faster penetration of flux front observed. There is some inhomogeneity of the penetrating flux front at 83 K, however not nearly as pronounced as at 77 K. This increase in the flux front inhomogeneity at 77 K could be connected to a fairly abrupt reduction in the size of the vortex-bundles formed due to collective pinning at many pinning centres. The correlated bundle radius for thin films is described by $R_b = C_{66}a/f\sqrt{n}$, where C_{66} is the shear elastic modulus, a the mean vortex spacing, f the pinning force and n the areal density of pinning sites [116]. Considering that $C_{66} \sim \bar{B}/\lambda^2$ [117], where $\bar{B}$ is the average flux density, and supposing that more pinning sites are coming into play at decreasing temperatures as the characteristic superconducting length-scales get smaller, then the product of the pinning force and the square root of the density of pinning sites, $f\sqrt{n}$, can increase faster than $1/\lambda^2$. Hence, a decreasing bundle size can be expected as the temperature is reduced, as observed. Moreover, the dynamics of the reverse flux front penetration and annihilation are different from the first flux front penetration, indicating that the vortex bundle structure is affected by the surrounding environment. We can see this when comparing the magenta line/squares with the blue line/circles in Figures 6-7(c) and (d), revealing the complex vortex dynamics in these tapes.

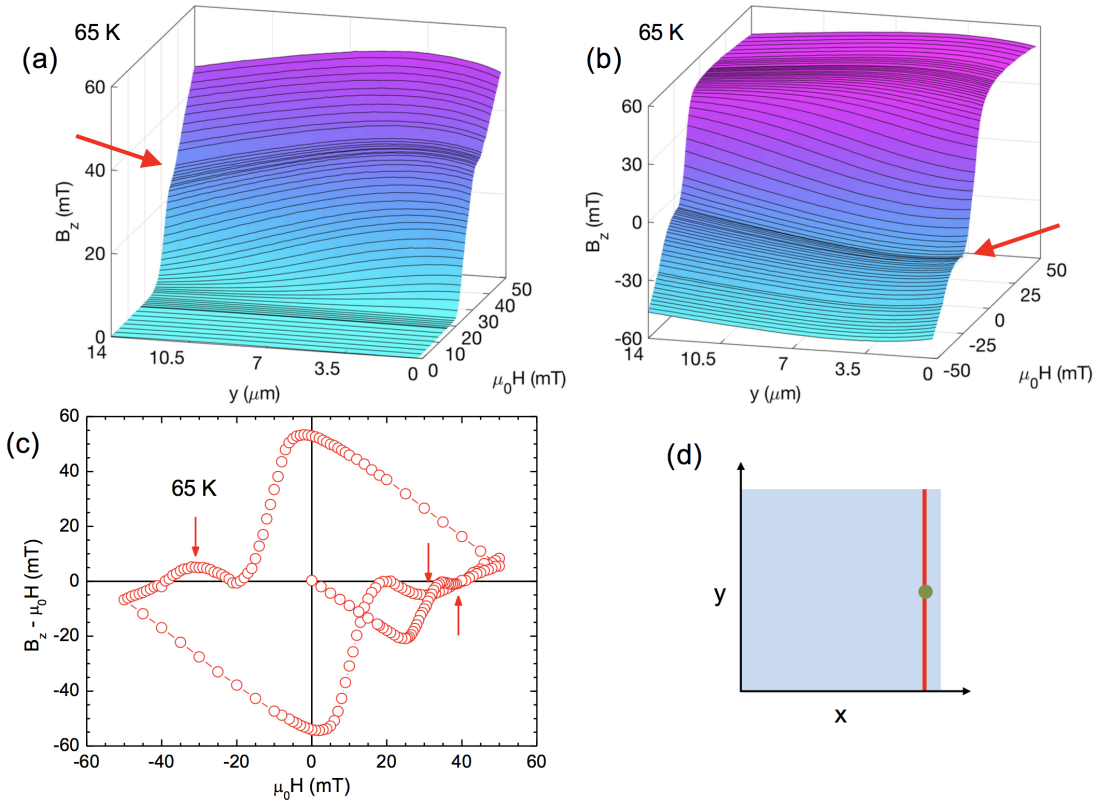

Figure 6-8: *Line scans along the y-axis of SHPM images at 65 K ($H_c = 59.2$ mT) for different applied magnetic fields (a) for the first flux front penetration and (b) for the subsequent reverse flux front penetration. An observed flux locking is indicated by a red arrow in a narrow range of applied magnetic fields. (c) 'Local' magnetisation loop measured at a single pixel of the SHPM images as a function of applied magnetic field at 65 K. Vertical red arrows indicate fishtail-like peaks in the 'local' magnetisation. (d) Schematic representation of the SHM scan area indicating the line where the magnetic induction has been measured in (a) and (b) (red line) and the pixel where the data in (c) (green dot) have been constructed. Reproduced from Reference [109].*

We have also performed 'local' magnetisation and SHPM measurements down to 65 K, the sub-cooled liquid nitrogen temperature at which tape performance is known to be greatly improved including a considerable increase in critical current density [118]. Figure 6-8(a) shows line scans along the y-axis of SHPM images as the applied field is increased from the zero field-cooled virgin state and display a pronounced flat region at μ_0H $\sim$ 40 mT highlighted by the red arrow. In the same way, a similar flattening can be seen at μ_0H $\sim$ -30 mT in Figure 6-8(b) when the magnetic field direction is reversed. Interestingly, we can see in Figure 6-8(c) peaks in the M_l-H loops, indicated by vertical red arrows, which look like the so-called fishtail effect. Here we introduce two possible explanations for the described phenomena. The peaks seen in Figure 6-8(c) seem to occur due to a field-dependent increase in the critical current close to the edge of the tape that screens out further flux penetration over a narrow range of fields. We believe that this arises due to a "matching effect" when the density of vortices near the edge of the tape becomes approximately equal to the density of strong pinning centres in the superconducting YBCO film. As a result, the critical current increases at the edge of the tape, increasing the field gradient, dB_z/dy, thus preventing additional vortices from penetrating to the SHPM field of view. Hence the magnetic flux detected stays locked over a narrow range of applied fields of approximately $\mu_0\Delta$H $\sim$ 10 mT. By considering the measured matching field of B_z $\sim$ 40 mT as a lower bound on the relevant magnetic induction, we can estimate the density of strong pinning sites as $B \sim \phi_0/a^2$ where ϕ_0 is the magnetic quantum of flux and a is the mean spacing between pinning centres. Thus we can estimate an upper bound of $a \sim 230$ nm which can be compared with the mean spacing between Dy_2O_3 second phase particles present in the YBCO film introduced to enhance vortex pinning. Second phase particles with diameter in the range of 10-100 nm and average density of 1538 particles/μm^2 (71 particles/0.06 μm^3, 1.3 μm thick YBCO film) has been reported in an STEM study [119] of a Dy-doped superconducting YBCO thin film from a very similar tape. Vortex 'core' pinning ideally occurs with centres of radius comparable to the superconducting coherence length and it is expected that only the smallest particles will be effective. Based on our estimated matching field only a small portion of the particles act as strong pinning centres equivalent to a density of $\sim$20 particles/μm^2. However, having in mind that the magnetic induction at

the edge of the tape will be strongly enhanced due to the sample geometry and related demagnetisation effects [107], the exact matching pinning site density is likely to be very much higher than our lower bound estimate. These peaks were not seen at 77 K and all temperatures above this, probably because the applied field sweeps in these cases were restricted to $\mu_0 H < 35$ mT, and the condition to observe the matching effect would not have been reached.

These observed peaks can alternatively be related to the possible existence of a field-driven disordering transition. The system could go through a transition, in an increasing magnetic field, from a somewhat well-ordered Bragg glass phase [120, 121], to a disordered glassy phase [122, 123], as dictated by the fine balance between elastic, pinning and thermal energies [124]. Therefore, in this picture the peak is a dynamic response coming from additional pinning due to a more effective interaction with the vortex pinning landscape in the disordered glassy phase. Considering the exceptionally high levels of disorder present in these 2G-HTS films, the existence of a well-ordered Bragg glass phase appears to be rather implausible, and a description in terms of matching effects seems much more probable.

6.3 Conclusions

We have studied and mapped the critical state of a commercial second-generation superconducting high temperature tape. At temperatures close to T_c the classical critical state model due to Brandt and Indenbom describes the vortex system relatively well when thermal energy plays a greater role in comparison to typical pinning energies. However, our experimental results deviate strongly from the critical state model at lower temperatures showing considerable suppression of the singular slope, dB_z/dy, predicted at the flux front. Our measurements show strikingly different flux front roughening and profile broadening behaviours at different temperatures. We observe a much more localised behaviour of the penetrating flux fronts at low temperatures, demonstrating the temperature-dependence of the pinning force and the active pinning site density which establish the typical sizes of vortex-bundles. In local magnetisation measurements at 65 K, we have also observe fishtail-like magnetisation peaks which we relate to a local increase in the critical current density near the edge of the YBCO films, most likely

arising due to a magnetic field matching effect. We believe that these findings contribute importantly to the field of high current superconductors providing a more detailed understanding of vortex phenomena in 2G-HTS tapes.

Chapter 7

Final Conclusions and Prospects for Future Work

7.1 Superconductor-Ferromagnet Hybrid Arrays

Scanning Hall probe imaging of the hybrid superconductor-ferromagnet structures has revealed distinct vortex patterns when superconducting and ferromagnetic systems are in direct contact or separated by a thin dielectric layer. In the hybrid system with the Nb film and Py disks in electronic contact, vortices (antivortices) have nucleated on each dark (bright) lobe of the 'cloverleaf' stray fields of disks, while only one vortex has nucleated at the centre of the disk in the hybrid system with an intermediate dielectric layer. The remarkable difference of the vortex pinning landscape in the presence of electronic coupling highlights how proximity effects that modify the S-F interface also strongly affect the whole hybrid structure.

The stark contrast of vortex configurations between the different hybrids is removed once the permalloy ferromagnetic disks are in the 'onion' state, achieved by applying an in-plane magnetic field. This finding suggests the possibility of systematic control of superconducting vortices by sensitively tuning the pinning landscape via the magnetic state of the disks.

Even though most of our results have shown qualitative agreement with existing theoretical predictions some features, such as the pairwise vortex attraction

with nearby interstitial vortices of same sign and the interstitial vortex nucleation near poles of the same polarity in the 'onion' state, have shown non-trivial vortex interactions which lack theoretical understanding. Therefore, we hope that our results can stimulate further theoretical investigations in such structures.

Furthermore, the non-collinear magnetisation in the ferromagnetic Py disks can potentially lead to the generation of equal spin triplet correlations and long range supercurrents. This can be studied in other hybrid geometries and in different materials systems using vortex imaging by scanning Hall probe microscopy to identify the presence of these fascinating long range proximity effects.

7.2 Superconductor-Ferromagnet Josephson Junctions

Two planar superconductor-ferromagnet Josephson junctions with a disk-like structure have been characterised by electrical magnetotransport measurements. The different FIB cut depths in the junctions have produced distinct responses. The shallow FIB cut junction revealed the expected conventional superconducting junction behaviour while the deep FIB cut junction indicated possible unconventional superconducting junction behaviour.

The non-collinear magnetisation in the ferromagnetic disk geometry can potentially generate spin triplet supercurrents which are expected to be non-uniformly distributed, creating distinct interference patterns as a function of perpendicular magnetic field. However, the magnetic stray fields coming from the ferromagnetic structure also can potentially modify the supercurrent spatial distribution. OOMMF micromagnetic simulation revealed that the magnetic state of the Py structure significantly relaxes in the perpendicular applied magnetic fields used in experiments.

In order to elucidate the role of the magnetic stray fields and magnetisation changes in the junction, new devices with different FIB etch depths must be fabricated and studied. The overall physical structure can benefit from some alterations in the fabrication process to achieve a more symmetrical disk geometry in which more uniform stray fields will be present for the systematic study of their role in the junction. Also, an extended range of applied excitation currents

and temperatures for the resistance and critical current measurements might provide richer details of the device properties. To achieve a consistent initial magnetisation structure, the devices must have the magnetic state of the Py disk conditioned in stronger external out-of-plane magnetic fields. Following these additional steps we will be able to conclusively confirm the presence of spin triplet supercurrents.

7.3 The critical state in a 2G-HTS Tape

Local properties of the magnetic flux front penetration in a commercial second generation high-temperature superconducting tape have been investigated by scanning Hall probe microscopy by systematic and sequential magnetic imaging at different temperatures. These tapes possess strong potential for use in diverse commercial applications where high currents and magnetic fields are required. Hence, it is critical to their further development and wider implementation to obtain an improved understanding of the pinning potential landscape and the vortex behaviour within them in order to prevent the unexpected collapse of the superconducting critical current density.

The classical critical state model due to Brandt and Indenbom describes the vortex system relatively well at temperatures close to the superconducting critical temperature in comparison to the results at lower temperatures. The deviations from classical critical state flux distributions at lower temperatures and the localised flux bundles suggest a strong temperature-dependence of the pinning force and the active pinning site density in the tape, that creates a different vortex landscape with new pinning sites coming into play as the characteristic superconducting lengthscales reduce with temperature. This is reflected in the very different flux front roughening and profile broadening behaviours at different temperatures.

The 'fishtail' magnetisation peaks observed at 65 K were linked to an increase in the critical current density near the edge of the films arising due to a matching effect. Further systematic and sequential imaging at the lower temperatures of 65 K and 77 K under larger magnetic field excursions could shed further light on the origin of these peaks.

Finally, a higher spatial resolution can potentially be achieved by imaging the

superconducting YBCO layer without stabiliser layers directly from the production line in order to achieve a closer approach to the sample.

List of publications

The following is a list of publications related to the work described in this thesis.

E. Marchiori and S. J. Bending,"Mapping the flux penetration profile in a 2G-HTS tape at the microscopic scale: deviations from a classical critical state model," Supercond. Sci. Technol., vol. 32, no. 2, p. 025009, 2019.

E. Marchiori, P. J. Curran, J. Kim, N. Satchell, G. Burnell, and S. J. Bending,"Reconfigurable superconducting vortex pinning potential for magnetic disks in hybrid structures," Sci. Rep., vol. 7, 2017.

Bibliography

[1] A. I. Buzdin, "Proximity effects in superconductor-ferromagnet heterostructures," *Rev. Mod. Phys.*, vol. 77, pp. 935–976, 2005.

[2] R. S. Keizer, S. T. B. Goennenwein, T. M. Klapwijk, G. Miao, G. Xiao, and A. Gupta, "A spin triplet supercurrent through the half-metallic ferromagnet CrO_2," *Nature*, vol. 439, no. 7078, pp. 825–827, 2006.

[3] T. S. Khaire, M. A. Khasawneh, W. P. Pratt, and N. O. Birge, "Observation of spin-triplet superconductivity in Co-based josephson junctions," *Phys. Rev. Lett.*, vol. 104, p. 137002, 2010.

[4] M. Eschrig, "Spin-polarized supercurrents for spintronics," *Phys. Today*, vol. 64, no. 1, pp. 43–49, 2011.

[5] F. S. Bergeret, A. F. Volkov, and K. B. Efetov, "Long-range proximity effects in superconductor-ferromagnet structures," *Phys. Rev. Lett.*, vol. 86, pp. 4096–4099, 2001.

[6] J. Linder and J. W. A. Robinson, "Superconducting spintronics," *Nat. Phys.*, vol. 11, no. 4, pp. 307–315, 2015.

[7] M. Eschrig, "Spin-polarized supercurrents for spintronics: a review of current progress," *Rep. Prog. Phys.*, vol. 78, no. 10, p. 104501, 2015.

[8] J. G. Bednorz and K. A. Müller, "Possible high T_c superconductivity in the Ba-LaCu-O system," *Zeitschrift für Physik B Condensed Matter*, vol. 64, no. 2, pp. 189–193, Jun 1986.

[9] M. K. Wu, J. R. Ashburn, C. J. Torng, P. H. Hor, R. L. Meng, L. Gao, Z. J. Huang, Y. Q. Wang, and C. W. Chu, "Superconductivity at 93 K

in a new mixed-phase Y-Ba-Cu-O compound system at ambient pressure," *Phys. Rev. Lett.*, vol. 58, pp. 908–910, 1987.

[10] H. C. Freyhardt, D. Lee, and T. Izumi, "Coated conductors and their applications," *Supercond. Sci. Technol.*, vol. 23, no. 1, p. 010201, 2009.

[11] H. K. Onnes, "Eletrical researches," *Leiden Communications*, no. 120b, 122b, 124c, 1911.

[12] W. Meissner and R. Ochsenfeld, "Ein neuer Effekt bei Eintritt der Supraleitfähigkeit," *Naturwissenschaften*, vol. 21, p. 787, 1933.

[13] F. London and H. London, "The electromagnetic equations of the supraconductor," *Proceedings of the Royal Society of London. Series A, Mathematical and Physical Sciences*, vol. 149, no. 866, pp. 71–88, 1935.

[14] M. Tinkham, *Introduction to Superconductivity*, 2nd ed. Dover Publications, 1996.

[15] J. F. Annett, *Superconductivity, superfluids and condensates.* Oxford University Press, 2004, vol. 5.

[16] A. C. Rose-Innes and E. H. Rhoderick, *Introduction to superconductivity.* Pergamon, 1978.

[17] V. L. Ginzburg and L. D. Landau, *Zh. Eksp. Teor. Fiz.*, vol. 20, p. 1064, 1950.

[18] P. G. De Gennes, *Superconductivity of Metals and Alloys.* CRC Press, 1966.

[19] V. V. Schmidt, *The Physics of Superconductors: Introduction to Fundamentals and Applications.* Springer, 1997.

[20] A. A. Abrikosov, "Magnetic properties of superconductors of the second group," *Zh. Eksp. Teor. Fiz.*, vol. 32, p. 1442, 1957, [Sov. Phys. JETP 5, 1174 (1957)].

[21] A. Castellanos, R. Wordenweber, G. Ockenfuss, A. v. Hart, and K. Keck, "Preparation of regular arrays of antidots in $YBa_2Cu_3O_7$ thin films and observation of vortex lattice matching effects," *Appl. Phys. Lett.*, vol. 71, no. 7, pp. 962–964, 1997.

[22] K. Harada, O. Kamimura, H. Kasai, T. Matsuda, A. Tonomura, and V. V. Moshchalkov, "Direct observation of vortex dynamics in superconducting films with regular arrays of defects," *Science*, vol. 274, no. 5290, pp. 1167–1170, 1996.

[23] J. I. Martín, M. Vélez, J. Nogués, and I. K. Schuller, "Flux pinning in a superconductor by an array of submicrometer magnetic dots," *Phys. Rev. Lett.*, vol. 79, no. 10, pp. 1929–1932, 1997.

[24] J. Bardeen, L. N. Cooper, and J. R. Schrieffer, "Theory of superconductivity," *Phys. Rev.*, vol. 108, pp. 1175–1204, 1957.

[25] H. Fröhlich, "Isotope effect in superconductivity," *Proceedings of the Physical Society. Section A*, vol. 63, no. 7, p. 778, 1950.

[26] C. A. Reynolds, B. Serin, W. H. Wright, and L. B. Nesbitt, "Superconductivity of isotopes of mercury," *Physical Review*, vol. 78, pp. 487–487, 1950.

[27] J. M. D. Coey, *Magnetism and Magnetic Materials*. Cambridge University Press, 2010.

[28] T. Shinjo, T. Okuno, R. Hassdorf, K. Shigeto, and T. Ono, "Magnetic vortex core observation in circular dots of permalloy," *Science*, vol. 289, no. 5481, pp. 930–932, 2000.

[29] T. Okuno, K. Shigeto, T. Ono, K. Mibu, and T. Shinjo, "MFM study of magnetic vortex cores in circular permalloy dots: behavior in external field," *J. Magn. Magn. Mater.*, vol. 240, no. 1-3, pp. 1–6, 2002.

[30] R. P. Cowburn, D. K. Koltsov, A. O. Adeyeye, M. E. Welland, and D. M. Tricker, "Single-domain circular nanomagnets," *Phys. Rev. Lett.*, vol. 83, pp. 1042–1045, 1999.

[31] N. A. Usov and S. E. Peschany, "Magnetization curling in a fine cylindrical particle," *J. Magn. Magn. Mater.*, vol. 118, no. 3, pp. L290 – L294, 1993.

[32] K. Y. Guslienko and K. L. Metlov, "Evolution and stability of a magnetic vortex in a small cylindrical ferromagnetic particle under applied field," *Phys. Rev. B*, vol. 63, p. 100403, 2001.

[33] M. J. Donahue and D. G. Porter, "Object Oriented MicroMagnetic Framework (OOMMF) Simulation," http://math.nist.gov/oommf/, 1999.

[34] A. F. Andreev, "The thermal conductivity of the intermediate state in superconductors," *J. Exp. Theor. Phys.*, vol. 19, no. 5, p. 1228, 1964.

[35] G. Deutscher, "Andreev–saint-james reflections: A probe of cuprate superconductors," *Rev. Mod. Phys.*, vol. 77, pp. 109–135, 2005.

[36] B. D. Josephson, "Possible new effects in superconductive tunnelling," *Phys. Lett.*, vol. 1, no. 7, pp. 251–253, 1962.

[37] A. Barone and G. Paternò, *Physics and Applications of the Josephson Effect*. Wiley, 2005.

[38] S. S. Saxena, P. Agarwal, K. Ahilan, F. M. Grosche, R. K. W. Haselwimmer, M. J. Steiner, E. Pugh, I. R. Walker, S. R. Julian, P. OPTmonthoux, G. G. Lonzarich, A. Huxley, I. Sheikin, D. Braithwaite, and J. Flouquet, "Superconductivity on the border of itinerant-electron ferromagnetism in UGe_2," *Nature*, vol. 406, p. 587, 2000.

[39] D. Aoki, A. Huxley, E. Ressouche, D. Braithwaite, J. Flouquet, J.-P. Brison, E. Lhotel, and C. Paulsen, "Coexistence of superconductivity and ferromagnetism in URhGe," *Nature*, vol. 413, p. 613, 2001.

[40] N. T. Huy, A. Gasparini, D. E. de Nijs, Y. Huang, J. C. P. Klaasse, T. Gortenmulder, A. de Visser, A. Hamann, T. Görlach, and H. v. Löhneysen, "Superconductivity on the Border of Weak Itinerant Ferromagnetism in UCoGe," *Phys. Rev. Lett.*, vol. 99, p. 067006, 2007.

[41] A. Y. Aladyshkin, A. Silhanek, W. Gillijns, and V. V. Moshchalkov, "Nucleation of superconductivity and vortex matter in superconductor ferromagnet hybrids," *Supercond. Sci. Tech.*, vol. 22, no. 5, p. 053001, 2009.

[42] A. I. Larkin and Y. N. Ovchinnikov, "Inhomogeneous state of superconductors," *Zh. Eksp. Teor. Fiz.*, vol. 47, pp. 1136–1146, 1964.

[43] P. Fulde and R. A. Ferrell, "Superconductivity in a strong spin-exchange field," *Phys. Rev.*, vol. 135, pp. A550–A563, 1964.

[44] M. Houzet and A. I. Buzdin, "Long range triplet josephson effect through a ferromagnetic trilayer," *Phys. Rev. B*, vol. 76, p. 060504, 2007.

[45] J. W. A. Robinson, J. D. S. Witt, and M. G. Blamire, "Controlled injection of spin-triplet supercurrents into a strong ferromagnet," *Science*, vol. 329, no. 5987, pp. 59–61, 2010.

[46] K. Lahabi, M. Amundsen, J. A. Ouassou, E. Beukers, M. Pleijster, J. Linder, P. Alkemade, and J. Aarts, "Controlling supercurrents and their spatial distribution in ferromagnets," *Nat. Commun.*, vol. 8, no. 1, p. 2056, 2017.

[47] H. J. Levinson, *Principles of Lithography*, 3rd ed. Spie Press, 2010.

[48] M. A. Mohammad, M. Muhammad, S. K. Dew, and M. Stepanova, "Fundamentals of electron beam exposure and development," in *Nanofabrication*. Springer, 2012, pp. 11–41.

[49] P. G. Glöersen, "Ion-beam etching," *J. Vac. Sci. Technol.*, vol. 12, no. 1, pp. 28–35, 1975.

[50] D. Depla, S. Mahieu, and J. Greene, "Sputter deposition processes," in *Handbook of deposition technologies for films and coatings : science, applications and technology*, P. M. Martin, Ed. William Andrew, 2010, pp. 253–296.

[51] A. Sarangan, "Nanofabrication," in *Fundamentals and Applications of Nanophotonics*, J. W. Haus, Ed. Woodhead Publishing, 2016, pp. 149–184.

[52] C. A. Volkert and A. M. Minor, "Focused ion beam microscopy and micromachining," *MRS bulletin*, vol. 32, no. 5, pp. 389–399, 2007.

[53] S. Reyntjens and R. Puers, "A review of focused ion beam applications in microsystem technology," *J. Micromechanics Microengineering*, vol. 11, no. 4, pp. 287–300, 2001.

[54] A. M. Chang, H. D. Hallen, L. Harriott, H. F. Hess, H. L. Kao, J. Kwo, R. E. Miller, R. Wolfe, J. Van der Ziel, and T. Y. Chang, "Scanning hall probe microscopy," *Appl. Phys. Lett.*, vol. 61, no. 16, pp. 1974–1976, 1992.

[55] A. M. Chang, H. D. Hallen, H. F. Hess, H. L. Kao, J. Kwo, A. Sudbø, and T. Y. Chang, "Scanning Hall-probe microscopy of a vortex and field fluctuations in $La_{1.85}Sr_{0.15}CuO_4$ films," *EPL*, vol. 20, no. 7, p. 645, 1992.

[56] A. Oral, S. J. Bending, and M. Henini, "Real-time scanning hall probe microscopy," *Appl. Phys. Lett.*, vol. 69, no. 9, pp. 1324–1326, 1996.

[57] ——, "Scanning hall probe microscopy of superconductors and magnetic materials," *J. Vac. Sci. Technol.*, vol. 14, no. 2, pp. 1202–1205, 1996.

[58] S. J. Bending and A. Oral, "Hall effect in a highly inhomogeneous magnetic field distribution," *J. Appl. Phys.*, vol. 81, no. 8, pp. 3721–3725, 1997.

[59] R. Dingle, H. L. Stöemer, A. C. Gossard, and W. Wiegmann, "Electron mobilities in modulation doped semiconductor heterojunction superlattices," *Appl. Phys. Lett.*, vol. 33, no. 7, pp. 665–667, 1978.

[60] S. J. Bending, "Local magnetic probes of superconductors," *Adv. Phys.*, vol. 48, no. 4, pp. 449–535, 1999.

[61] G. Boero, M. Demierre, P. A. Besse, and R. S. Popovic, "Micro-hall devices: performance, technologies and applications," *Sens. Actuator A-Phys.*, vol. 106, no. 1-3, pp. 314–320, 2003.

[62] P. J. Curran, "Vortex phenomena in unconvential superconductors," Ph.D. dissertation, University of Bath, 2012.

[63] Z. Yang, M. Lange, A. Volodin, R. Szymczak, and V. V. Moshchalkov, "Domain-wall superconductivity in superconductor–ferromagnet hybrids," *Nat. Mater.*, vol. 3, no. 11, p. 793, 2004.

[64] M. Lange, M. J. V. Bael, Y. Bruynseraede, and V. V. Moshchalkov, "Nanoengineered magnetic-field-induced superconductivity," *Phys. Rev. Lett.*, vol. 90, p. 197006, 2003.

[65] A. Hoffmann, L. Fumagalli, N. Jahedi, J. C. Sautner, J. E. Pearson, G. Mihajlovic, and V. Metlushko, "Enhanced pinning of superconducting vortices by magnetic vortices," *Phys. Rev. B*, vol. 77, p. 060506, 2008.

[66] J. E. Villegas and I. K. Schuller, "Controllable manipulation of superconductivity using magnetic vortices," *Supercond. Sci. Technol.*, vol. 24, no. 2, p. 024004, 2011.

[67] A. Hoffmann, P. Prieto, and I. K. Schuller, "Periodic vortex pinning with magnetic and nonmagnetic dots: The influence of size," *Phys. Rev. B*, vol. 61, pp. 6958–6965, 2000.

[68] G. Carneiro, "Tunable pinning of a superconducting vortex by a magnetic vortex," *Phys. Rev. B*, vol. 75, p. 094504, 2007.

[69] M. V. Milošević and F. M. Peeters, "Vortex pinning in a superconducting film due to in-plane magnetized ferromagnets of different shapes: The london approximation," *Phys. Rev. B*, vol. 69, p. 104522, 2004.

[70] M. J. Van Bael, J. Bekaert, K. Temst, L. Van Look, V. V. Moshchalkov, Y. Bruynseraede, G. D. Howells, A. N. Grigorenko, S. J. Bending, and G. Borghs, "Local observation of field polarity dependent flux pinning by magnetic dipoles," *Phys. Rev. Lett.*, vol. 86, pp. 155–158, 2001.

[71] M. Schneider, H. Hoffmann, and J. Zweck, "Lorentz microscopy of circular ferromagnetic permalloy nanodisks," *Appl. Phys. Lett.*, vol. 77, no. 18, pp. 2909–2911, 2000.

[72] J. Raabe, R. Pulwey, R. Sattler, T. Schweinböck, J. Zweck, and D. Weiss, "Magnetization pattern of ferromagnetic nanodisks," *J. Appl. Phys.*, vol. 88, no. 7, pp. 4437–4439, 2000.

[73] O. M. Auslaender, L. Luan, E. W. J. Straver, J. E. Hoffman, N. C. Koshnick, E. Zeldov, D. A. Bonn, R. Liang, W. N. Hardy, and K. A. Moler, "Mechanics of individual isolated vortices in a cuprate superconductor," *Nat. Phys.*, vol. 5, p. 35, 2008.

[74] C. Reichhardt, "Vortices wiggled and dragged," *Nat. Phys.*, vol. 5, p. 15, 2009.

[75] G. Webb, F. Marsiglio, and J. Hirsch, "Superconductivity in the elements, alloys and simple compounds," *Physica C*, vol. 514, pp. 17 – 27, 2015.

[76] M. Schneider, H. Hoffmann, and J. Zweck, "Magnetic switching of single vortex permalloy elements," *Appl. Phys. Lett.*, vol. 79, no. 19, pp. 3113–3115, 2001.

[77] E. Marchiori, P. J. Curran, J. Kim, N. Satchell, G. Burnell, and S. J. Bending, "Reconfigurable superconducting vortex pinning potential for magnetic disks in hybrid structures," *Sci. Rep.*, vol. 7, 2017.

[78] W. Oepts, R. Coehoorn, J. C. S. Kools, and W. J. M. de Jonge, "Enhanced anisotropy of permalloy layers sputter deposited on V-grooved substrates and tilted surfaces," *J. Magn. Magn. Mater.*, vol. 218, no. 1, pp. 114–120, 2000.

[79] A. I. Gubin, K. S. Il'in, S. A. Vitusevich, M. Siegel, and N. Klein, "Dependence of magnetic penetration depth on the thickness of superconducting Nb thin films," *Phys. Rev. B*, vol. 72, p. 064503, 2005.

[80] J. Pearl, "Current distribution in superconducting films carrying quantized fluxoids," *Appl. Phys. Lett.*, vol. 5, 1964.

[81] R. B. G. Kramer, A. V. Silhanek, W. Gillijns, and V. V. Moshchalkov, "Imaging the statics and dynamics of superconducting vortices and antivortices induced by magnetic microdisks," *Phys. Rev. X*, vol. 1, p. 021004, 2011.

[82] U. Essmann and H. Träuble, "The direct observation of individual flux lines in type II superconductors," *Phys. Lett. A*, vol. 24, no. 10, pp. 526–527, 1967.

[83] T. Shapoval, V. Metlushko, M. Wolf, B. Holzapfel, V. Neu, and L. Schultz, "Direct observation of superconducting vortex clusters pinned by a periodic array of magnetic dots in ferromagnetic/superconducting hybrid structures," *Phys. Rev. B*, vol. 81, p. 092505, 2010.

[84] M. S. Kalenkov, A. D. Zaikin, and V. T. Petrashov, "Triplet superconductivity in a ferromagnetic vortex," *Phys. Rev. Lett.*, vol. 107, p. 087003, 2011.

[85] M. A. Silaev, "Possibility of a long-range proximity effect in a ferromagnetic nanoparticle," *Phys. Rev. B*, vol. 79, p. 184505, 2009.

[86] F. S. Bergeret, A. F. Volkov, and K. B. Efetov, "Odd triplet superconductivity and related phenomena in superconductor-ferromagnet structures," *Rev. Mod. Phys.*, vol. 77, no. 4, pp. 1321–1373, 2005.

[87] M. S. Anwar, F. Czeschka, M. Hesselberth, M. Porcu, and J. Aarts, "Long-range supercurrents through half-metallic ferromagnetic CrO_2," *Phys. Rev. B*, vol. 82, p. 100501, 2010.

[88] C. Klose, T. S. Khaire, Y. Wang, W. P. Pratt, N. O. Birge, B. J. McMorran, T. P. Ginley, J. A. Borchers, B. J. Kirby, B. B. Maranville, and J. Unguris, "Optimization of Spin-Triplet Supercurrent in Ferromagnetic Josephson Junctions," *Phys. Rev. Lett.*, vol. 108, p. 127002, 2012.

[89] D. Sprungmann, K. Westerholt, H. Zabel, M. Weides, and H. Kohlstedt, "Evidence for triplet superconductivity in josephson junctions with barriers of the ferromagnetic heusler alloy Cu_2MnAl," *Phys. Rev. B*, vol. 82, p. 060505, 2010.

[90] N. Banerjee, J. W. A. Robinson, and M. G. Blamire, "Reversible control of spin-polarized supercurrents in ferromagnetic Josephson junctions," *Nat. Commun.*, vol. 5, p. 4771, 2014.

[91] W. M. Martinez, W. P. Pratt, and N. O. Birge, "Amplitude Control of the Spin-Triplet Supercurrent in S/F/S Josephson Junctions," *Phys. Rev. Lett.*, vol. 116, p. 077001, 2016.

[92] V. V. Bolginov, V. S. Stolyarov, D. S. Sobanin, A. L. Karpovich, and V. V. Ryazanov, "Magnetic switches based on Nb-PdFe-Nb Josephson junctions with a magnetically soft ferromagnetic interlayer," *JETP Letters*, vol. 95, no. 7, pp. 366–371, 2012.

[93] R. C. Dynes and T. A. Fulton, "Supercurrent density distribution in Josephson junctions," *Phys. Rev. B*, vol. 3, pp. 3015–3023, 1971.

[94] J. W. A. Robinson, S. Piano, G. Burnell, C. Bell, and M. G. Blamire, "Critical current oscillations in strong ferromagnetic π junctions," *Phys. Rev. Lett.*, vol. 97, p. 177003, 2006.

[95] J. F. Maguire, F. Schmidt, S. Bratt, T. E. Welsh, and J. Yuan, "Installation and Testing Results of Long Island Transmission Level HTS Cable," *IEEE Trans. Appl. Supercond.*, vol. 19, no. 3, pp. 1692–1697, 2009.

[96] W. Schmidt, B. Gamble, H.-P. Kraemer, D. Madura, A. Otto, and W. Romanosky, "Design and test of current limiting modules using YBCO-coated conductors," *Supercond. Sci. Technol.*, vol. 23, no. 1, p. 014024, 2010.

[97] K. S. Haran, S. Kalsi, T. Arndt, H. Karmaker, R. Badcock, B. Buckley, T. Haugan, M. Izumi, D. Loder, J. W. Bray, P. Masson, and E. W. Stautner, "High power density superconducting rotating machines-development status and technology roadmap," *Supercond. Sci. Technol.*, vol. 30, no. 12, p. 123002, 2017.

[98] M. Leroux, K. J. Kihlstrom, S. Holleis, M. W. Rupich, S. Sathyamurthy, S. Fleshler, H. P. Sheng, D. J. Miller, S. Eley, L. Civale, A. Kayani, P. M. Niraula, U. Welp, and W.-K. Kwok, "Rapid doubling of the critical current of $YBa_2Cu_3O_{7-\delta}$ coated conductors for viable high-speed industrial processing," *Appl. Phys. Lett.*, vol. 107, no. 19, p. 192601, 2015.

[99] H. Yamasaki and H. Yamada, "Flux pinning properties of $YBa_2Cu_3O_{7-\delta}$ thin films containing a high density of nanoprecipitates: A comparative study to reveal size effects," *Physica C*, vol. 542, pp. 46 – 54, 2017.

[100] J. Trastoy, C. Ulysse, R. Bernard, M. Malnou, N. Bergeal, J. Lesueur, J. Briatico, and J. E. Villegas, "Tunable flux-matching effects in high-T_c superconductors with nonuniform pinning arrays," *Phys. Rev. Appl.*, vol. 4, p. 054003, 2015.

[101] W.-K. Kwok, U. Welp, A. Glatz, A. E. Koshelev, K. J. Kihlstrom, and

G. W. Crabtree, "Vortices in high-performance high-temperature superconductors," *Rep. Prog. Phys.*, vol. 79, no. 11, p. 116501, 2016.

[102] R. B. Dinner, K. A. Moler, M. R. Beasley, and D. M. Feldmann, "Enhanced current flow through meandering grain boundaries in $YBa_2Cu_3O_{7-x}$ films," *Appl. Phys. Lett.*, vol. 90, no. 21, p. 212501, 2007.

[103] R. B. Dinner, K. A. Moler, D. M. Feldmann, and M. R. Beasley, "Imaging ac losses in superconducting films via scanning hall probe microscopy," *Phys. Rev. B*, vol. 75, p. 144503, 2007.

[104] S. Sathyamurthy, C. Thieme, and M. W. Rupich, *American Superconductor: Second Generation Superconductor Wire - From Research to Power Grid Applications*. Springer International Publishing, 2016, pp. 131–165.

[105] D. Dimos, P. Chaudhari, and J. Mannhart, "Superconducting transport properties of grain boundaries in $YBa_2Cu_3O_7$ bicrystals," *Phys. Rev. B*, vol. 41, pp. 4038–4049, 1990.

[106] T. Hikata, K. Sato, and H. Hitotsuyanagi, "Ag-sheathed Bi-Pb-Sr-Ca-Cu-O superconducting wires with high critical current density," *Jpn. J. Appl. Phys.*, vol. 28, no. Part 2, No. 1, pp. L82–L84, 1989.

[107] E. H. Brandt and M. Indenbom, "Type-II-superconductor strip with current in a perpendicular magnetic field," *Phys. Rev. B*, vol. 48, pp. 12 893–12 906, 1993.

[108] M. W. Rupich, X. Li, C. Thieme, S. Sathyamurthy, S. Fleshler, D. Tucker, E. Thompson, J. Schreiber, J. Lynch, D. Buczek *et al.*, "Advances in second generation high temperature superconducting wire manufacturing and R&D at American Superconductor Corporation," *Supercond. Sci. Technol.*, vol. 23, no. 1, p. 014015, 2009.

[109] E. Marchiori and S. J. Bending, "Mapping the flux penetration profile in a 2G-HTS tape at the microscopic scale: deviations from a classical critical state model," *Supercond. Sci. Technol.*, vol. 32, no. 2, p. 025009, 2019.

[110] W. Lang, I. Puica, M. Peruzzi, K. Lemmermann, J. D. Pedarnig, and D. Bäuerle, "Depairing current and superconducting transition of YBCO at

intense pulsed currents," *Phys. Stat. Sol. (c)*, vol. 2, no. 5, pp. 1615–1624, 2005.

[111] R. Surdeanu, R. J. Wijngaarden, E. Visser, J. M. Huijbregtse, J. H. Rector, B. Dam, and R. Griessen, "Kinetic roughening of penetrating flux fronts in high- T_c thin film superconductors," *Phys. Rev. Lett.*, vol. 83, pp. 2054–2057, 1999.

[112] G. Blatter, M. V. Feigelman, V. B. Geshkenbein, A. I. Larkin, and V. M. Vinokur, "Vortices in high-temperature superconductors," *Rev. Mod. Phys.*, vol. 66, pp. 1125–1388, 1994.

[113] A. T. Fiory, A. F. Hebard, P. M. Mankiewich, and R. E. Howard, "Renormalization of the mean-field superconducting penetration depth in epitaxial $YBa_2Cu_3O_7$ films," *Phys. Rev. Lett.*, vol. 61, pp. 1419–1422, 1988.

[114] J. Annett, N. Goldenfeld, and S. R. Renn, "Interpretation of the temperature dependence of the electromagnetic penetration depth in $YBa_2Cu_3O_{7-\delta}$," *Phys. Rev. B*, vol. 43, pp. 2778–2782, 1991.

[115] Y. Yeshurun, A. P. Malozemoff, and A. Shaulov, "Magnetic relaxation in high-temperature superconductors," *Rev. Mod. Phys.*, vol. 68, pp. 911–949, 1996.

[116] A. I. Larkin and Y. N. Ovchinnikov, "Pinning in type II superconductors," *J. Low Temp. Phys.*, vol. 34, no. 3, pp. 409–428, 1979.

[117] E. H. Brandt, "The vortex lattice in conventional and high-Tc superconductors," *Braz. J. Phys.*, vol. 32, pp. 675–684, 2002.

[118] J. C. Llambes, D. Hazelton, J. Duval, M. Albertini, S. Repnoy, V. Selvamanickam, G. Majkic, I. Kesign, J. Langston, M. Steurer, F. Bogdan, J. Hauer, D. Crook, S. Ranner, T. Williams, and M. Coleman, "Performance of 2G-HTS tapes in sub-cooled LN2 for superconducting fault current limiting applications," *IEEE Trans. Appl. Supercond.*, vol. 21, no. 3, pp. 1206–1208, 2011.

[119] V. Ortalan, M. Herrera, M. Rupich, and N. Browning, "Three dimensional analyses of flux pinning centers in Dy-doped $YBa_2Cu_3O_{7-\delta}$ coated superconductors by STEM tomography," *Physica C*, vol. 469, no. 23, pp. 2052–2059, 2009.

[120] T. Giamarchi and P. Le Doussal, "Elastic theory of flux lattices in the presence of weak disorder," *Phys. Rev. B*, vol. 52, pp. 1242–1270, 1995.

[121] K. Shibata, T. Nishizaki, T. Sasaki, and N. Kobayashi, "Phase transition in the vortex liquid and the critical endpoint in $YBa_2Cu_3O_y$," *Phys. Rev. B*, vol. 66, p. 214518, 2002.

[122] D. S. Fisher, M. P. A. Fisher, and D. A. Huse, "Thermal fluctuations, quenched disorder, phase transitions, and transport in type-II superconductors," *Phys. Rev. B*, vol. 43, pp. 130–159, 1991.

[123] R. H. Koch, V. Foglietti, W. J. Gallagher, G. Koren, A. Gupta, and M. P. A. Fisher, "Experimental evidence for vortex-glass superconductivity in Y-Ba-Cu-O," *Phys. Rev. Lett.*, vol. 63, pp. 1511–1514, 1989.

[124] T. Nishizaki and N. Kobayashi, "Vortex-matter phase diagram in $YBa_2Cu_3O_y$," *Supercond. Sci. Technol.*, vol. 13, no. 1, pp. 1–11, 2000.